LOCALIZATION AND TOMOGRAPHIC IMAGING FOR SPATIALLY AWARE MOBILE RADIO NETWORKS

A Dissertation
Presented to
The Academic Faculty

By

Brian M. Beck

In Partial Fulfillment
of the Requirements for the Degree
Doctor of Philosophy in the
School of Electrical and Computer Engineering

Georgia Institute of Technology

December 2016

LOCALIZATION AND TOMOGRAPHIC IMAGING FOR SPATIALLY AWARE MOBILE RADIO NETWORKS

Approved by:

Dr. Xiaoli Ma, Advisor
School of Electrical and Computer Engineering
Georgia Institute of Technology

Dr. Robert J. Baxley
School of Electrical and Computer Engineering
Georgia Institute of Technology

Dr. Gee-Kung Chang
School of Electrical and Computer Engineering
Georgia Institute of Technology

Dr. Mary Ann Weitnauer
School of Electrical and Computer Engineering
Georgia Institute of Technology

Dr. Federico Bonetto
School of Mathematics
Georgia Institute of Technology

Date Approved: November 9, 2016

Mathematics is the alphabet with which God has written the universe...

-Galileo

ACKNOWLEDGEMENTS

Studying toward the PhD degree in electrical engineering at Georgia Tech has been a tremendously rewarding experience. Nevertheless, a PhD is a long and challenging path to take, especially given the high caliber and expectations of Georgia Tech. I am sure that no one could cross the finish line without proper help and guidance from the right people. My studies were no exception. This section brings proper acknowledgment of those important people front and center.

I would first like to recognize the efforts of my academic advisor, Dr. Xiaoli Ma. I recall the summer of 2011, when she decided to take a chance on me as a student and welcome me into her research group. There is no shortage of exceptional students at Tech for a professor to choose from. I would like to thank her for all of her productive feedback on all of my published work, and for creating an environment of collaboration within our group. Encouraging students to present their work every semester at group seminars was also an excellent way to help me hone my technical presentation skills.

I must also give special thanks to my co-advisor, Dr. Robert Baxley, with the Georgia Tech Research Institute (GTRI). I had the great fortune of working very closely with Dr. Baxley at GTRI from 2011 to 2014, and can thank him for much of the inspiration in my work. I very much miss our constant discussions, and was saddened when he left GTRI in 2014 to pursue other interests. I know that without his help in laying my research foundation, none of this would have succeeded.

I would also like to give special mention to Joseph Kim, who spent countless hours with me in the lab. Without his help coding, debugging, and testing, I am sure that the CSOT and our localization research would not be what it is today. Similarly I acknowledge Soradhmuny Lanh for his work on the SPACR testbed. His data collection experiments were invaluable to our latest work. Finally, I thank the people of GTRI for their encouragement and willingness to provide me with time and funding to pursue my research interests.

TABLE OF CONTENTS

LIST OF TABLES

LIST OF FIGURES

PUBLICATIONS AND COPYRIGHT

A substantial majority of the research presented in this dissertation has been published with the IEEE, or submitted for publication. Those portions used in this dissertation are © IEEE, and are reproduced with permission according to IEEE guidelines. Relevant sections are indicated in the text with footnotes. The publications resulting from this dissertation research are listed below for reference.

B. Beck, R. Baxley, and X. Ma, "Improving radio tomographic images using multipath signals," in *Proc. IEEE Int. Conf. on Wireless Inform. Technol. and Syst. (ICWITS)*, Nov. 2012, pp. 1–4

B. Beck, J. Kim, R. Baxley, *et al.*, "RadioBOT: A spatial cognitive radio testbed," in *Proc. IEEE Aerospace Conf.*, Mar. 2013, pp. 1–9

B. Beck, R. Baxley, and X. Ma, "Regularization techniques for floor plan estimation in radio tomographic imaging," in *Proc. IEEE Global Conf. on Signal and Inform. Process. (GlobalSIP)*, Dec. 2013, pp. 177–180

B. Beck and R. Baxley, "Anchor free node tracking using ranges, odometry, and multidimensional scaling," in *Proc. IEEE Int. Conf. on Acoustics, Speech and Signal Process. (ICASSP)*, May 2014, pp. 2209–2213

B. Beck, R. Baxley, and J. Kim, "Real-time, anchor-free node tracking using ultrawideband range and odometry data," in *Proc. IEEE Int. Conf. on Ultra-Wideband (ICUWB)*, Aug. 2014, pp. 286–291

B. Beck, X. Ma, and R. Baxley, "Ultra-wideband tomographic imaging in uncalibrated networks," *IEEE Trans. Wireless Commun.*, vol. 15, no. 9, pp. 6474–6486, Sep. 2016

B. Beck, R. Baxley, and X. Ma, "Uncooperative RSS-based emitter localization in uncalibrated mobile networks," in *Proc. 17th IEEE Int. Workshop on Signal Proc. Advances in Wireless Commun. (SPAWC)*, Jul. 2016, pp. 1–6

B. Beck, S. Lanh, R. Baxley, *et al.*, "Uncooperative emitter localization using signal strength in uncalibrated mobile networks," *IEEE Trans. Wireless Commun.*, 2016, (submitted for publication).

SUMMARY

Mobile wireless sensors and networks have many potential applications, and have attracted much industry and academic interest in the past decade. This work pursues research which enhances the spatial awareness of such networks. Specifically, in this work we focus on original contributions to the spatial topics of interference/spectrum mapping, cooperative ultra-wideband (UWB) localization and tracking, uncooperative emitter localization, and active mapping of the radio frequency (RF) shadowing environment. Toward contributions in these areas, we introduce the Cognitive Spectrum Operations Testbed (CSOT), which was designed specifically for spatially oriented wireless network research. The system consists of eight mobile nodes, each with software defined radio (SDR) and UWB capabilities. The CSOT's hardware and software are first demonstrated in an interference mapping experiment, which is used to optimize the positioning of a relay node. We then utilize CSOT to pursue high accuracy, cooperative indoor localization and tracking. This research utilizes fusion of both UWB ranging and odometry data. The experimental results demonstrate average positioning error of < 2 cm, and drops the requirement of pre-surveying the positions of anchor nodes. With precise localization in hand, we then use CSOT to explore the field of radio tomographic imaging (RTI). For our RTI work, UWB signal strength data is employed to produce accurate images of the RF shadowing environment. A major contribution of this work is its deployment in a completely uncalibrated network. All necessary parameters are estimated directly from the data. We show performance improvements through simulation and experiment, and via comparison with other techniques. Finally, we apply the uncalibrated network principle to the uncooperative emitter localization problem. We develop algorithms to model the effects of uncalibrated sensors on the data covariance and mitigate them. Further simulations and experimental results demonstrate significant localization performance improvements over naive methods.

CHAPTER 1
INTRODUCTION

The past decade has seen an explosion in the number of deployed wireless-enabled devices. The proliferation of cellular devices, wireless capable sensors, and single-board computers is not expected to slow down, as component cost continues to fall and device capability continues to increase. Research and development of autonomous mobile systems is also occurring in parallel. Mobile wireless networks are proposed for environmental monitoring, military surveillance, and search and rescue; these are just some examples of systems defining the state of the art [9]. With this technological landscape in mind, the objective of this work is to improve the spatial awareness of mobile wireless networks. We examine the concept of spatial awareness in several ways; the main topics are organized here into chapters. This introduction provides a brief overview of each spatially-oriented research topic. We emphasize the natural progression of the maturing research as each topic is addressed.

First, we recognize the need for realistic testing and experimental validation, going beyond simulation results wherever possible. To that end, we introduce the Cognitive Spectrum Operations Testbed (CSOT) in Chapter 2. CSOT is a system of eight robotic mobile nodes with both ultra-wideband (UWB) and software defined radio (SDR) capabilities, and was designed and built explicitly for this work. The full hardware, software, and potential applications of the testbed are described. CSOT is then deployed in a real-time interference mapping experiment. A spatially interpolated map is created by using CSOT nodes to densely sample the received signal strength (RSS) of an interfering signal as a function of space. We then show how the map can be utilized to optimize the positioning of a relay node in a two hop relay network [2].

The initial approach to localization in Chapter 2 and [2] uses simple dead reckoning of each node independently, using known starting positions and encoder wheel data. This

proved to lose accuracy quickly with distance and required pre-surveying of each node's position. To address this, we propose to jointly estimate all node positions using pairwise UWB distance measurements, while also incorporating the readily available odometry (wheel encoder) data from the nodes. In Chapter 3, we present algorithms to incorporate this information in a multidimensional scaling (MDS) framework. Our experiments demonstrate node tracking accuracy to < 2 cm localization error [4, 5]. Our tracking algorithm does not require surveying the positions of stationary nodes, instead creating a coordinate system relative to their positions. Both simulation and experimental results demonstrate the performance improvements of our novel UWB/odometry data fusion technique when compared to the benchmark extended Kalman filter (EKF).

It is very advantageous for a sensor network to know not only the positions of its nodes, but also the features present in the environment, e.g. walls or other obstacles. The UWB signals used for ranging and localization also carry significant information about shadowing from objects attenuating the signal. With accurate knowledge of node positions in the mobile network, in Chapter 4 we shift focus to cooperatively estimating these features in the environment using UWB-capable sensors. The process of estimating the shadowing environment as a function of space has been called radio tomographic imaging (RTI) [10]. Our research addresses challenges specific to performing RTI in a mobile network consisting of uncalibrated sensors. Namely, these are online estimation of path loss and individual link bias parameters without a prior calibration of the system [6]. A convex, regularized optimization problem is formed from the model to estimate the unknown shadowing image. Our results demonstrate the performance improvements of our approach in simulation when compared to standard approaches, and with respect to the Cramér Rao lower bound (CRLB). We provide experimental results using CSOT to perform RTI in several environments, displaying subjectively high quality image reconstructions.

Finally, in Chapter 5 we seek to apply the lessons learned from working with uncalibrated networks to the problem of localizing an uncooperative emitter. Unlike the cooper-

ative problem, in this case the uncooperative emitter does not actively participate in being localized. Since we are interested in uncalibrated mobile networks, this work is constrained to measuring only the emitter's RSS, and we assume that each mobile node measuring RSS is biased. We propose to model these effects in the nonlinear path loss model as additive random variables, so that their effects may be treated statistically. The main advantage of this approach is that we may model the bias parameters without growing the dimension of the parameter vector, which is very important in nonlinear problems. Instead only the data covariance is estimated in closed form. We derive the covariance estimator via the principle of variance least squares (VLS). VLS estimation of covariance allows our algorithms to scale very well with the size of the network, and hence the number of bias parameters. Two localization algorithms are introduced, one based on nonlinear least squares (NLS), and a more complex version based on the Gaussian particle filter (GPF), with improved performance. Both simulation and experimental testbed results are provided to demonstrate the performance improvements over naive methods.

Since this work covers a broad spectrum of research topics, many readers may be interested in particular points. As such, each chapter is intended to stand on its own. A complete introduction and relevant background information are provided to allow the reader to skip to the chapter(s) of interest, if desired. All acronyms, mathematical notation, etc. are fully defined in each chapter for clarity.

CHAPTER 2

Cognitive Spectrum Operations Testbed

2.1 Background and Contributions

Cognitive radio is an emerging area of research, whose central goal is to employ reprogrammable radio hardware and software to more efficiently utilize the available spectrum [11]. This originally meant simply detecting an available frequency band for transmission, i.e., spectrum sensing [12]. More recently, the field has expanded to address additional challenges. Some of these include signal classification, dynamic channel allocation, and cognitive networks. In signal classification, a cognitive radio would attempt to detect the presence of incoming signals and measure their parameters. This may need to be done with reduced knowledge of those signal parameters [13], such as those originating from hostile emitters. In dynamic channel allocation, portions of the available spectrum are divided dynamically in time, and possibly space, among various nodes. This allows increased utilization of the available spectrum, which may change with time, as well as sharing this information with other nodes in the area.

Conversely, a hostile radio network could be used to increase the interference of friendly nodes or otherwise disrupt communication. Thus, a cognitive radio network must also deal with security concerns. Security threats such as incumbent emulation, spectrum sensing data falsification, and primary user emulation have been addressed [14, 15]. In each of these cases, hostile cognitive radios attempt to disrupt the function of a friendly network. In incumbent and primary user emulation, a hostile cognitive radio attempts to imitate the spectrum usage of an authorized user of the network. This reduces the available spectrum by fooling legitimate nodes. In the spectrum sensing data falsification attack, a hostile network node or terminal transmits false data pertaining to a spectrum sensing operation.

This disrupts the cognitive radio network by providing false data, rather than false signals. Defense against this type of attack requires authentication of each cognitive radio's data, similar to a traditional computer network.

In performing these cognitive tasks, a radio network may also be *spatially aware*, that is, it must have some information about its environment. Clearly this information includes spectrum sensing data already discussed. However, other environmental data might include terrain features, emitter locations, and correlations with previously acquired data [16]. There are now radio frequency (RF)-based techniques for gathering such data, as in the field of radio tomographic imaging (RTI), which can form tomographic images of buildings, objects, and terrain using collected signal strength data [10, 17]. Other spatially oriented tasks include emitter localization, spectrum/interference mapping, and trajectory optimization.

All of the aforementioned techniques, however, depend on collection of large amounts of RF data. Data to be collected generally requires large spatial separation, precise localization, and mobility of radio nodes. It has been suggested that all possible information that a mobile radio network can gather be aggregated into a central database, forming a radio environment map [16]. This would enable centralized or shared decision making with the network. The difficulty, time, and expense associated with data collection for testing and research purposes has been a limiting factor in these areas. Even with today's sophisticated radio hardware, no single platform exists to meet all the needs of research in the above fields. Automated, unmanned collection of radio frequency data with mobility is a key goal in support of such research.

Toward this goal, we have developed a system of mobile, unmanned nodes capable of collecting a variety of RF data and transmitting the received data back to a centralized server for processing. Our system, called the Cognitive Spectrum Operations Testbed (CSOT), consists of eight individual nodes and a central desktop server[1]. CSOT has sev-

[1]Originally introduced as RadioBOT in [2], © IEEE 2013. Reproduced with permission.

eral key capabilities that support research in the above areas. First, each node is capable of transmitting or receiving arbitrary waveforms at high sample rates in both the $2.4 - 2.5$ and $5 - 6$ GHz frequency ranges, using its main software defined radio (SDR). Second, the system is capable of rapid, precise inter-node ranging and channel estimation using its secondary ranging radios. Third, the mobility of each node allows data to be collected over a wide area and at a high sampling density. Fourth, the movements and measurements taken by each CSOT node can either be controlled manually, or automated to suit the application. Finally, each node backhauls acquired data wirelessly to the server, which can then process and display data to the user in real time.

The CSOT testbed is easy to deploy and capable of gathering large amounts of data with minimal user intervention. However, the platform is also designed to be expandable with flexible tasks. Section 2.2 describes the hardware and software capabilities of the CSOT system in detail. Section 2.3 demonstrates a proof of concept experiment, where we use the CSOT system to gather interference power spectrum data over an area. The nodes measure the average received signal power over a test area, yielding spatial samples of an emitter's signal strength. From the data, we interpolate a spectrum map of the area, which is a smooth function of signal power vs. space. Finally, in Section 2.4, knowledge of the area's spatial spectrum is used to optimize the relay channel communication rate between a hypothetical transmitter and receiver inside the test area, by proper positioning of the relay node.

2.2 CSOT Hardware and Software

In this section we provide a description of the overall CSOT system and its capabilities. For CSOT, we have taken a modular approach to the hardware. Most components are commercial, off-the-shelf units that are readily available. This makes the nodes as expandable as possible in their capabilities, while minimizing cost and development time. In this section, we detail the important parts of each node, highlighting the contribution of each component

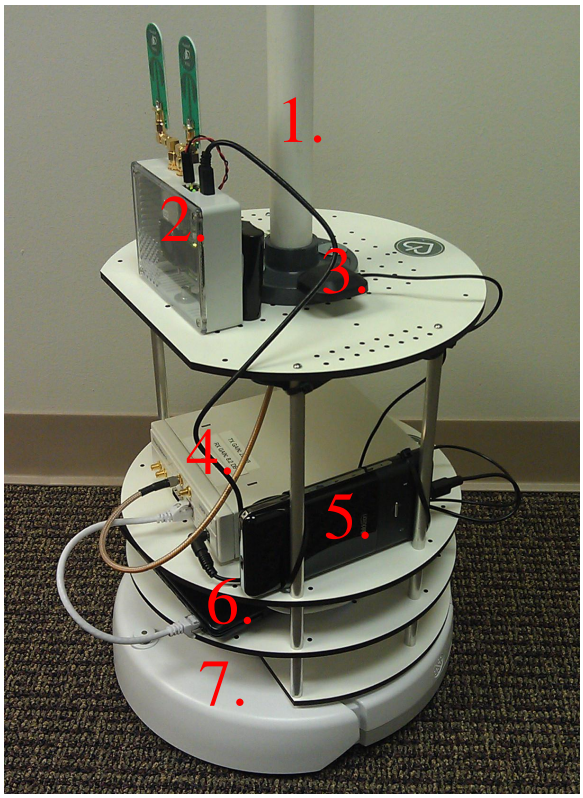

Figure 2.1: Closeup of a CSOT node's hardware. 1. Antenna mast. 2. PulsON P410 radio 3. GPS antenna 4. USRP N200 radio 5. Battery pack 6. Laptop controller 7. iRobot Create

to the overall functionality of the system. The main parts of the system are highlighted in Figure 2.1.

2.2.1 Base: iRobot Create

To provide a physical foundation and mobility for each node, we have selected the iRobot Create[2]. This versatile robot provides a low-profile platform to support all other hardware. Its mobility allows the antennas to move and reposition in the test area. The iRobot's movements are controlled through a simple, open serial interface, which also transmits data from its numerous sensors. The independent 2-wheel drive can propel the iRobot at speeds up to $0.5\ {}^{m}/_{s}$, and allows driving forward, backward, or rotating in place. The on-board sensor suite can provide useful environmental feedback. These include wall sensors, travel

[2]Available at `http://www.irobot.com`

distance and angle dead reckoning, IR packet sensing, and cliff/wheel drop sensing. These sensors allow each CSOT node to avoid walls or other obstructions in the environment without additional hardware. To support the rest of the CSOT hardware, the TurtleBot structure is employed to house all other components. This shelving system has 4 platforms on which other hardware can be mounted. This provides plenty of space for the current radio hardware, with plenty of room left for future expansion.

2.2.2 Computer Controller

A laptop computer is needed for each CSOT node to serve as a controller that all peripherals can connect to. The controller collects and processes the measurement data from radios, issues commands to the iRobot, and runs the CSOT client software. The controller hardware requirement can be filled by any commercially available laptop capable of running Windows 7, with sufficient USB ports and WiFi network access. Collected data is backhauled to the server using a TCP connection over WiFi. The WiFi connection also enables server control of individual nodes. All measurement, data collection, and automation of each node is performed by our own software, purpose built for CSOT. Each CSOT node runs its own instance of the client application. The LabVIEW programming language was chosen for all software development.

2.2.3 Primary Radio: Ettus USRP N200

The Ettus USRP N200 is a general purpose SDR[3]. SDRs allow as much signal processing as possible to be handled digitally, minimizing the size of the analog radio front end [18]. This makes an SDR highly customizable to the application. Arbitrary baseband waveforms can be transmitted and received, with a burst sample rate of up to $50\ {}^{MS}/_{s}$, and a transmit power up to 100 mW. The carrier frequency can be selected in software to any value in the RF front end's range. The CSOT is currently set up for operation in either the

[3]Available at `http://www.ettus.com`

$2.4-2.5$ GHz or $5.0-6.0$ GHz bands. These features make the USRP suitable for a variety of RF measurement tasks. With proper calibration, absolute amplitude accuracy is within ± 1.0 dBm. Since some applications may call for precise synchronization between nodes, we also employ a Global Positioning System (GPS)-based disciplined oscillator (DO) module for each USRP unit. This DO module locks each radio's local oscillator with the GPS signal, to within 0.01 ppm. Doing so allows all radios to achieve precise clock synchronization even when physically separated, making time division routines possible. Finally, the USRP antenna is mounted on a mast 1.3 m above the ground to maximize reception and transmission.

2.2.4 Secondary Radio: PulsON P410

The secondary radio employed on CSOT is a PulsON P410 ultra-wideband (UWB) ranging radio from Time Domain[4]. The primary role of this radio system is to provide each CSOT node with a precise estimate of its range to other nodes. The PulsON ranging radio provides 2.2 GHz of bandwidth, centered at 4.3 GHz. The large bandwidth allows time-of-flight (TOF) measurements to be taken between the radios, even in high multipath environments. Depending on the presence of a clear line-of-sight (LOS) path, ranging accuracy is ± 2 cm to ± 1 m. The ranging radio system can be used for cooperative localization algorithms, and is potentially more accurate than traditional GPS localization. The system is also functional in indoor environments where GPS is not available, and updates the nodes' range estimates multiple times per second. While we employ simple dead reckoning for positioning in this chapter, we fully explore the localization and tracking potential of the P410 radio in Chapter 3. In addition to localization, the PulsON radio may also be employed for general purpose tasks where a large bandwidth is useful. These include channel estimation, coarse ranging, and even radar imaging.

[4]Available at `http://www.timedomain.com`

2.2.5 Server

The CSOT system is monitored and controlled by a central server. Data collected by each node is backhauled via the TCP connection over WiFi to a server machine. Similarly to the computer controller of each node, the requirements for the server are minimal. Any desktop or laptop capable of running Windows 7 is possible, though processing requirements will vary with the application. Data is processed by the server in real time, giving continuous updates to the user. The user can issue new commands to the nodes for movement or measurement, or allow the process to remain automated.

2.3 Spectrum Mapping Experiment

Spectrum mapping, or spectrum cartography, is a spatial, cognitive radio task in which an estimated spatial map of RF energy is formed from a limited number of sample points. Collected data can be used to localize unfriendly emitters, or infer terrain features [19]. The limited spatial data is combined to form a continuous map using various methods, such as splines, basis pursuit, and group-lasso [20, 21, 22]. CSOT can be used to gather real world RF data to produce these interpolated spectrum maps. We have performed an experiment to collect such data and form a spectrum map for a laboratory hallway. The spectrum map will later be used to maximize a relay channel's communication rate in Section 2.4.

2.3.1 Experiment Setup

In our experiment, we measure average received signal power from an emitter in several narrow frequency bands around 5.5 GHz. From the data, the emitter's effect on the area's spectrum is measured. The area to be mapped in this case is a laboratory corridor, shown schematically in Figure 2.2. A photograph of the initial test configuration is shown in Figure 2.3.

The relevant radio frequency parameters are as follows. The emitter is an Agilent E4438C

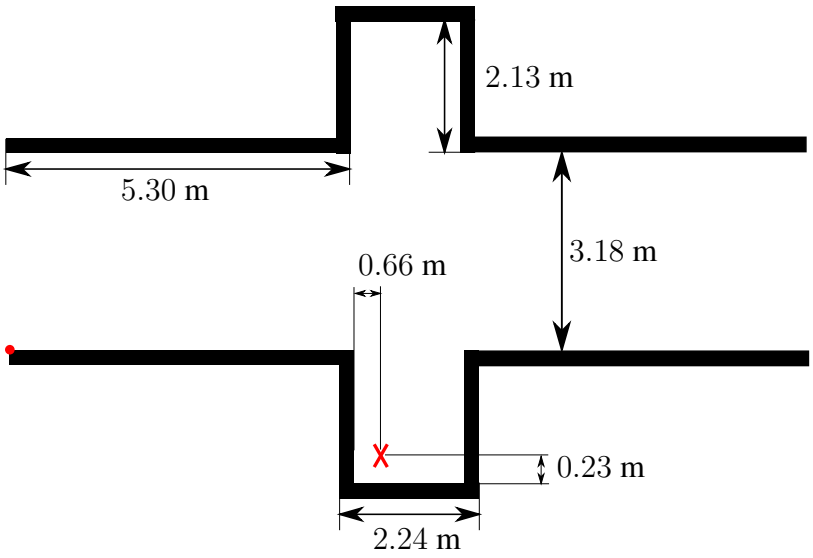

Figure 2.2: Schematic of the symmetric hallway used in the experiment. The red dot indicates the origin of the coordinate system. The red "X" is the actual location of the emitter antenna.

Figure 2.3: Initial radio node configuration before starting the test. The emitter is in the right alcove down the hall.

vector signal generator (VSG) hooked directly into an isotropic, wideband antenna. The VSG transmits a channel estimation waveform at a power level of 10.00 dBm. The waveform samples are defined by

$$s(n) = e^{j2\pi \frac{n(n+1)}{N}}, \tag{2.1}$$

where $N = 2^{14} = 16384$ samples. This waveform is sampled at an in phase/quadrature (IQ) rate of 2.00 MHz, giving the waveform approximately 2.2 MHz of bandwidth. This signal is modulated onto a carrier frequency of 5.500 GHz. We have chosen 5.5 GHz for several reasons. First, there is a lack of interference near this frequency in our area. Second, physical obstructions will tend to cause increased attenuation in this frequency range compared with the 2.4 GHz band, and diffraction effects around corners will be less significant. This increases the line of sight effect on the system; the transmitter is highly shadowed when the line of sight is blocked. Finally, this frequency is within the capabilities of the USRP hardware for reception.

For each CSOT receiver, the primary radio receives at the following carrier frequencies: 5.498, 5.499, 5.500, 5.501, and 5.502 GHz. Each receiver listens for 500 ms on each carrier frequency, for every data point, and samples at an IQ rate of 2 $^{MS}/_{s}$. This ensures that the emitter's signal is captured, while also leaving the edge channels empty to examine the background noise. Data is sampled uniformly over the test area, approximately every 0.5 m in each direction. The CSOT nodes do not move during a receive operation.

From the received complex IQ samples at each carrier frequency, each CSOT node computes average power, defined by

$$P_{avg} = \frac{1}{M} \sum_{i=0}^{M-1} \frac{\left|x(i)^2\right|}{R}, \tag{2.2}$$

measured in watts, since $x(i)$ has units of volts. M is the number of received samples for each data point, which is 10^6 in this case. $R = 100\ \Omega$ is the input impedance of the baseband analog to digital converter. The received power in watts is then converted to dBm

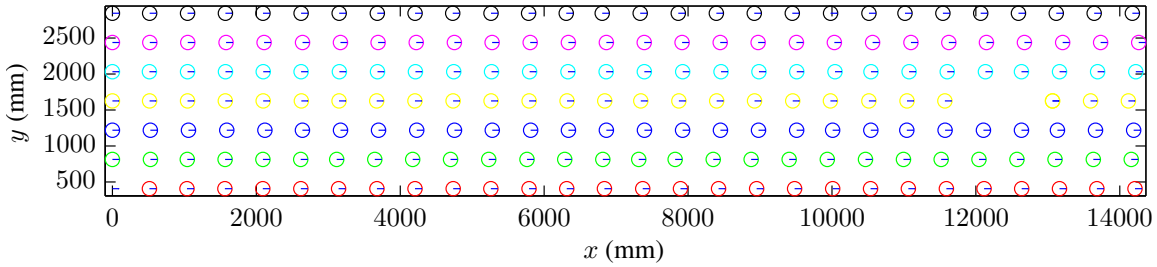

Figure 2.4: A map showing the locations of collected data. Color indicates the number assigned to each CSOT node.

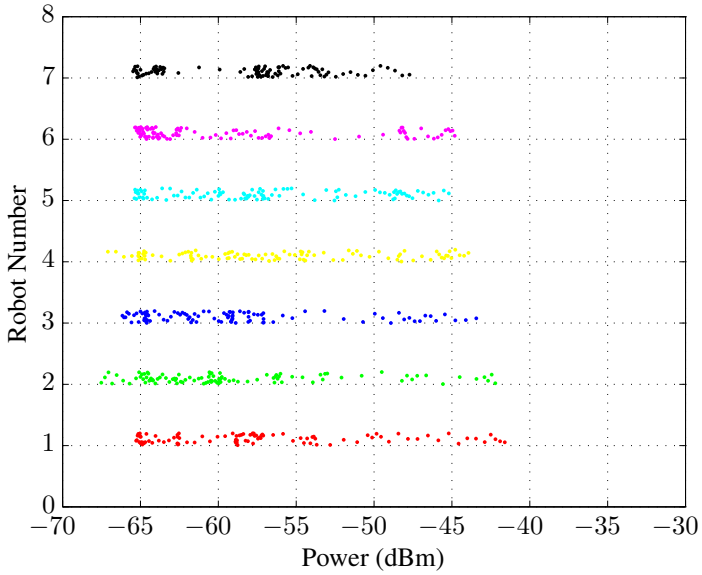

Figure 2.5: Distribution of P_{dBm} for each CSOT node, after normalization of the data.

by taking the log,

$$P_{dBm} = 10 \log_{10} (1000 \; P_{avg}) \; . \tag{2.3}$$

2.3.2 Experimental Results

Data was collected by the procedure outlined in Section 2.3. The spatial locations of each data point gathered are shown in Figure 2.4. The CSOT system allows such a uniform, high sampling density, which would be very time consuming to achieve without mobile nodes.

A received power calibration was performed for each USRP radio prior to the experiment. However, normalization of the data was still performed to correct for small differences in the dynamic range of each radio. The distribution of received power, P_{dBm}, is plotted in Figure 2.5 after normalization.

From the normalized data, a continuous spatial map of the average power is formed by interpolation. We have used a biharmonic spline interpolation method to estimate the power between data points, creating a smooth estimate for the entire hallway area [23]. Other estimation procedures could be used, such as those outlined previously. The interpolated map of the hallway spectrum for each carrier frequency is displayed in Figure 2.6. As expected, the average received power is significantly stronger when the nodes have a line of sight path to the emitter. The received power is also stronger for most data points closer to the emitter, although spatial nulls do exist. A lower spatial sampling density would miss this complex pattern in the map.

2.4 Relay Channel Rate Maximization

We now use the acquired spectrum map data to aid in positioning a relay node for a Gaussian relay channel that must operate inside the test area. In this relay channel, a fixed transmitter, X, is spatially separated from a fixed receiver, Y. In addition to transmitter and receiver, there is a relay node, R, which can aid communication between X and Y. Each link in the system communicates over an additive white Gaussian noise (AWGN) channel with channel capacity C_{ij}, as shown in Figure 2.7. We wish to choose the position of R such that some metric of communication rate between X and Y is maximized. For this problem, we assume that only one signal path will be used to communicate, i.e., X communicates with Y directly, or X communicates with Y through the relay R. Thus we do not assume any diversity gains from receiving two signals at Y. The signal path with the higher channel capacity will be chosen for communication. Since this metric is actually a lower bound on the true relay channel capacity, we use the term "achievable rate" to

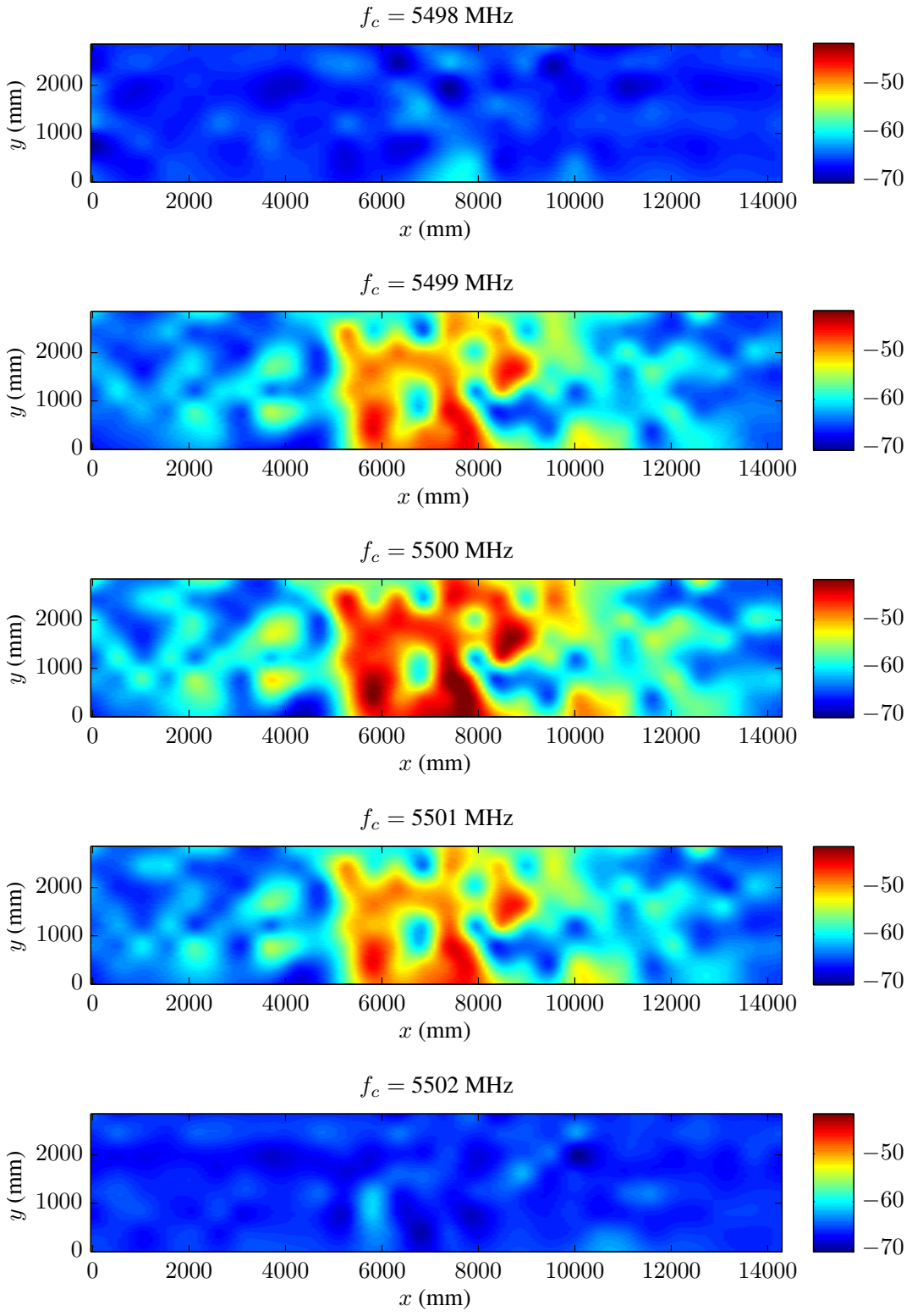

Figure 2.6: Interpolated spatial maps of P_{dBm} after normalization of the data, for each carrier frequency. The two end plots are outside the bandwidth of the emitter, picking up only background noise.

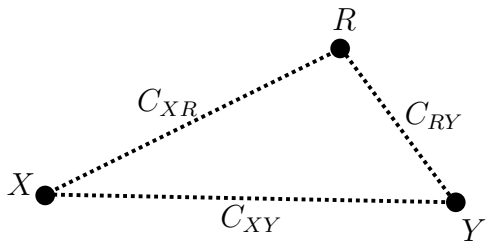

Figure 2.7: The Gaussian relay channel topology. The channel capacity C_{ij} for individual links is labeled. All channels are AWGN.

describe this parameter, to be maximized over all possible positions for R.

Nodes X and R have transmit power P_X and P_R, respectively. For this problem, the locations of transmitter X and receiver Y will be fixed at coordinates $(500, 500)$ mm and $(14000, 2000)$ mm, respectively. Also, we assume that communication occurs at 5.500 GHz, and is real-valued with a bandwidth of less than 1 MHz.

2.4.1 AWGN Channel

The direct path AWGN channel between X and Y has a block diagram shown in Figure 2.8. The Gaussian noise source Z_Y, with power N_Y, is due to the noise power present at the receiver. This noise value is determined from the estimated spectrum map of Figure 2.6. The channel capacity of this AWGN channel, measured in bits per channel use, is the well known result

$$C_{XY} = \frac{1}{2}\log_2\left(1 + \frac{|h_{XY}|^2 P_X}{N_Y}\right). \tag{2.4}$$

The value $|h_{XY}|^2$ is the channel gain experienced by the signal in propagating from X to Y. To model this factor, we use the log distance path loss model, expressed in linear terms. This is an approximate model appropriate for indoor wireless signal propagation. We assume a path loss exponent of 2, equivalent to free space, due to the line of sight and short distances present throughout the test area. With these assumptions and a reference

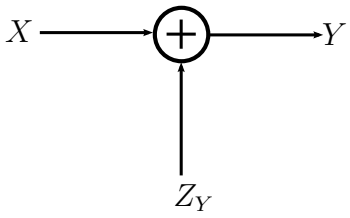

Figure 2.8: Direct path AWGN channel block diagram.

distance of 1 m, the channel gain is approximated from the path loss by

$$PL_{dB} = -\left(20\log_{10}\frac{4\pi}{\lambda} + 20\log_{10} d\right)$$
$$|h_{XY}|^2 = 10^{\frac{PL_{dB}}{10}}\,. \tag{2.5}$$

Here d is the distance between transmitter and receiver in meters, and λ is the wavelength in meters.

2.4.2 Decode and Forward Relay

First we assume that the relay node R uses a decode and forward communication technique. For decode and forward, R receives a signal from X and decodes the message. The decoded message is then re-encoded and sent to the receiver Y. In this way the relay "isolates" transmissions from X to Y along the relay path. The block diagram for the decode and forward relay path is shown in Figure 2.9. The AWGN noise sources Z_R and Z_Y have power N_R and N_Y, respectively. The value of N_R is determined by the choice of relay node position, which is the independent variable in this problem.

If the decode/encode operations are performed optimally, then the capacity of the relay path is simply the minimum capacity of the two AWGN channels that compose the path. Thus, the decode and forward relay path channel capacity, C_{df}, is given by

$$C_{df} = \min\left(C_{XR}, C_{RY}\right)\,, \tag{2.6}$$

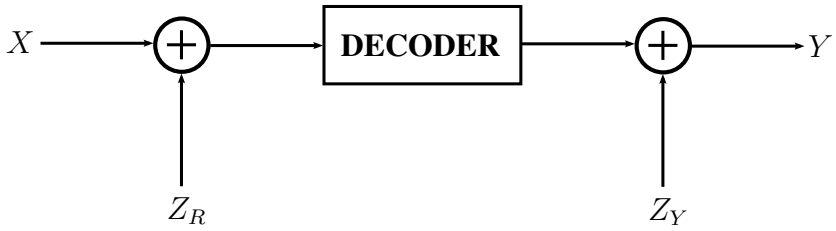

Figure 2.9: Decode and forward signal path block diagram.

where

$$C_{XR} = \frac{1}{2}\log_2\left(1 + \frac{|h_{XR}|^2 P_X}{N_R}\right), \tag{2.7}$$

and

$$C_{RY} = \frac{1}{2}\log_2\left(1 + \frac{|h_{RY}|^2 P_R}{N_Y}\right), \tag{2.8}$$

all measured in bits per channel use. The channel gains are again modeled using the log distance model. Since the system decides which signal path to use based on the one with the higher overall capacity, the achievable rate for the decode and forward scenario is given by

$$R_{df} = \max\left(C_{XY}, C_{df}\right). \tag{2.9}$$

The value of R_{df} is computed for $40,000$ placements of relay node R inside the test area, spaced uniformly. We do this for three sets of values for (P_X, P_R), measured in mW: $(25, 100)$, $(50, 50)$ and $(100, 25)$. The results are plotted in Figure 2.10, where R_{df} is shown as a function of relay node placement. The results show a clear dependence of the system's achievable rate on the placement of the relay node. In the top and middle plots of Figure 2.10, where transmitter power P_X is more limited, it is clear that the relay node improves the system's achievable rate by avoiding areas of high noise power. If the relay is placed in a region of high noise power, then the system will choose to communicate along the direct path, since the relay path actually has a lower capacity. In the bottom case, where the transmitter X has high power, the relay can only assist by being placed in low noise regions very near the receiver.

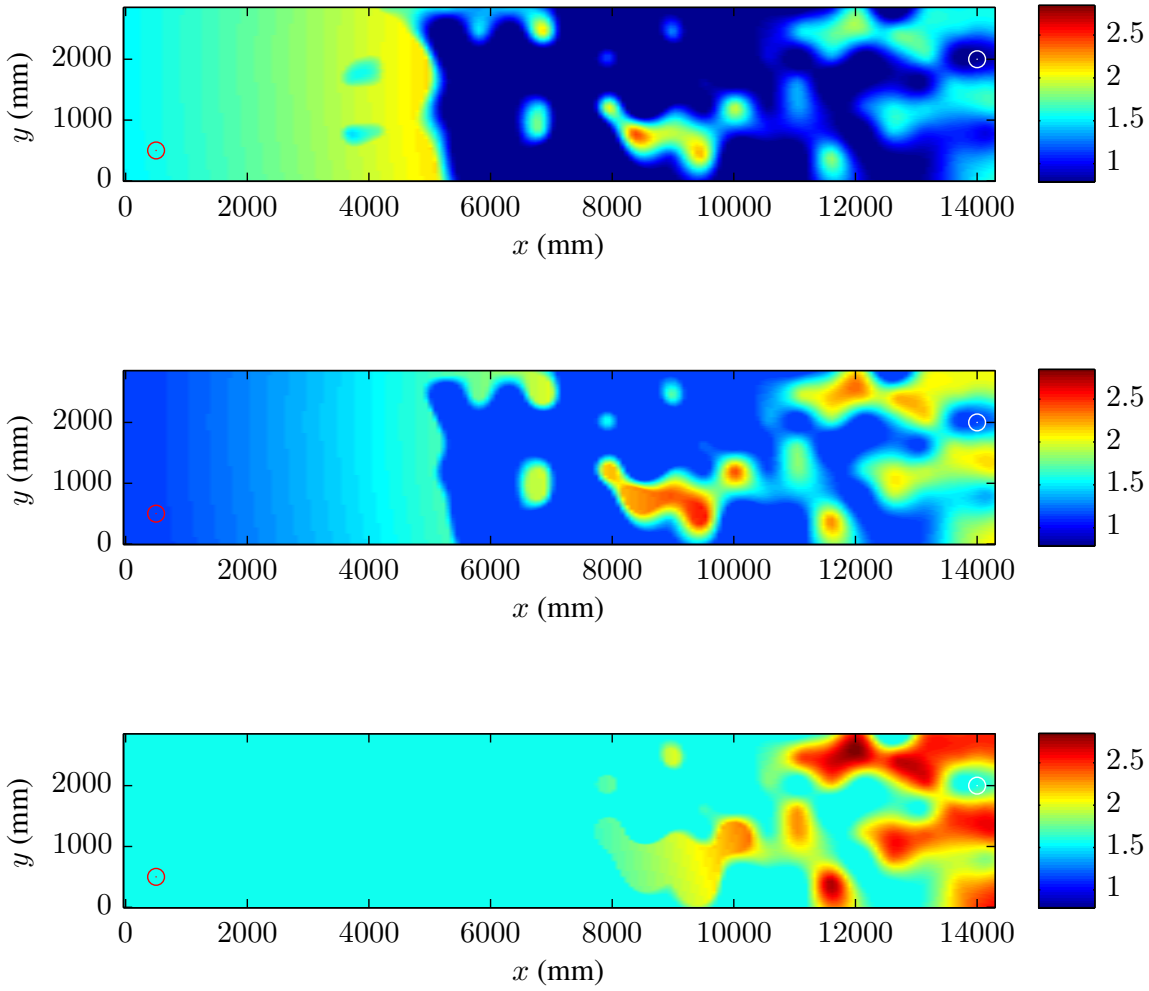

Figure 2.10: Plots of the relay channel achievable rate for the decode and forward scenario, R_{df}, as a function of relay node position, measured in bits. The red circle is the fixed transmitter X; the white circle is the fixed receiver Y. Top: $P_X = 25$, $P_R = 100$ mW. Middle: $P_X = 50$, $P_R = 50$ mW. Bottom: $P_X = 100$, $P_R = 25$ mW.

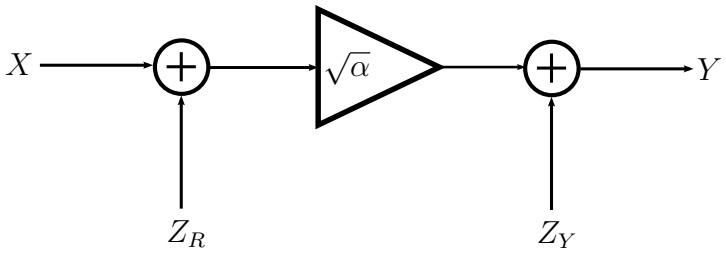

Figure 2.11: Amplify and forward signal path block diagram.

2.4.3 Amplify and Forward Relay

We consider another case in which the relay node employs an amplify and forward strategy instead. Rather than separately decoding and re-encoding the received signal, R instead takes the received signal, scales the power by a factor α, and re-transmits to Y. The block diagram is shown in Figure 2.11. Amplify and forward can boost the signal at Y, but also amplifies the noise originally received at R. Except for this change in the relay node's behavior, all other parameters remain the same as the decode and forward case. The relay path capacity is no longer simply the minimum of the $X - R$ and $R - Y$ paths, but is now given by the total signal to noise ratio (SNR) at Y. The channel capacity can be shown to be

$$C_{af} = \frac{1}{2}\log_2\left(1 + \frac{|h_{XR}|^2|h_{RY}|^2 P_X}{|h_{RY}|^2 N_R + \frac{N_Y}{\alpha}}\right) . \tag{2.10}$$

Since the amplifier in the relay node is constrained to power P_R, the gain factor α must be given by

$$\alpha = \frac{P_R}{|h_{XR}|^2 P_X + N_R} . \tag{2.11}$$

The achievable rate is again chosen to be the signal path with the highest capacity, either the direct path or the relay path. For the amplify and forward case, this is equal to

$$R_{af} = \max\left(C_{XY}, C_{af}\right) . \tag{2.12}$$

The rate R_{af} is again plotted as a function of relay node placement for the same set of power values. The results are shown in Figure 2.12. The map of R_{af} bears the same basic spatial pattern as in the decode and forward case of Figure 2.10. However, $R_{df} \geq R_{af}$ at all points, and for every power level. The difference between the two maps varies in the range $[0,\ 0.491]$ bits. Overall, these plots demonstrate that changing a relay node's position based on a spectrum map can have an impact on achievable rate of several bits per channel use. Given the spatial / spectral information provided by CSOT, we see that there is a strong chance that a relay node could provide little or no benefit to the system if placed in an ad-hoc manner. The spectrum map provides the data needed to select an effective relay node position.

2.5 Conclusion

Spatially aware cognitive radio networks are an emerging field of research with many potential applications. Such research can be enhanced by the ability to gather RF data quickly and in an automated manner over a large spatial area. To this end, we have introduced CSOT, a new testbed for spatially aware wireless network research. We have shown that CSOT is capable of gathering useful RF data by employing the system to map an area's power spectrum in several bands of interest. The spectrum map was then employed to optimize placement of a relay node to be used in aiding communication between a transmitter and receiver. CSOT allows solving such optimization problems using real data, giving an opportunity to test algorithms and models in the real world.

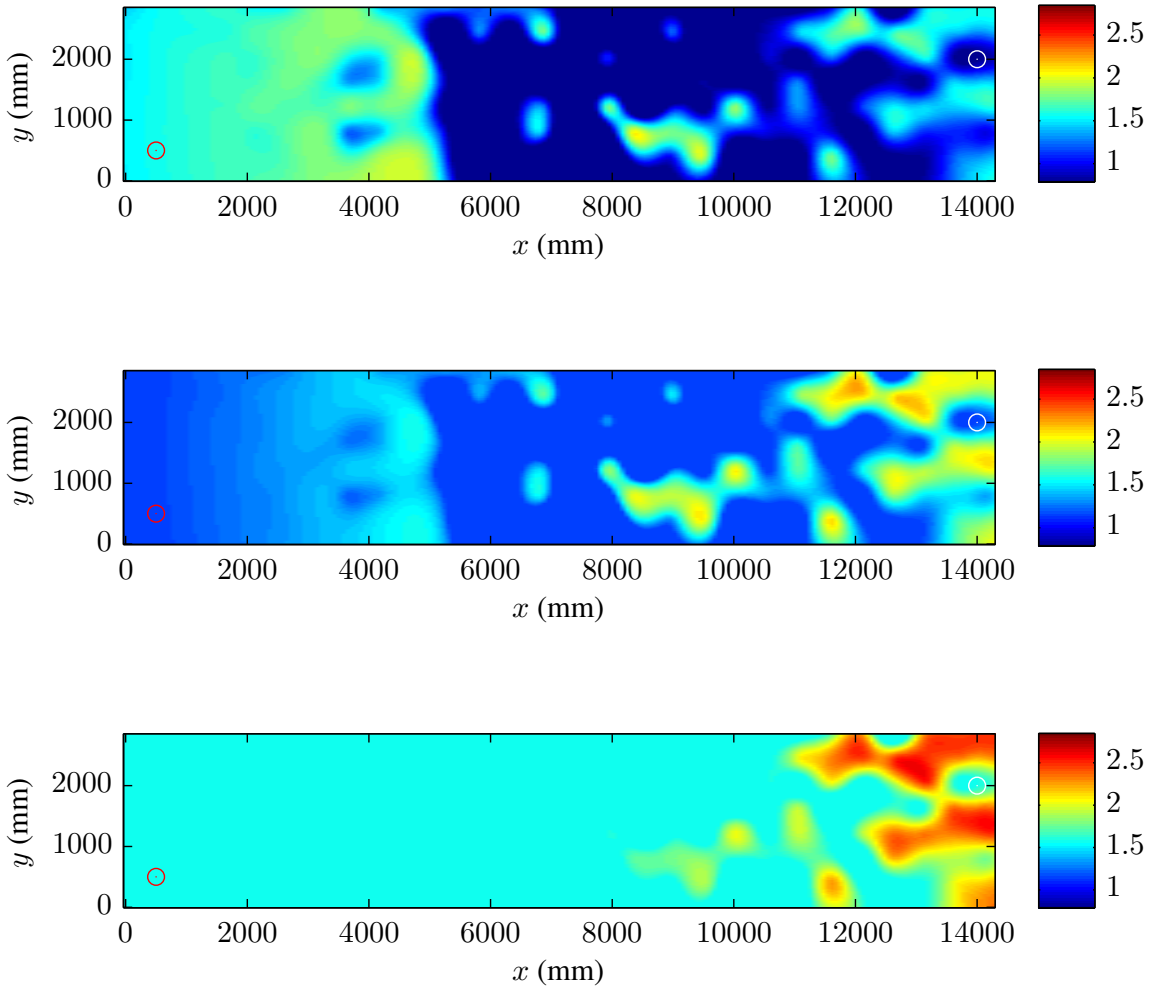

Figure 2.12: Plots of the relay channel achievable rate for the amplify and forward scenario, R_{af}, as a function of relay node position, measured in bits. The red circle is the fixed transmitter X; the white circle is the fixed receiver Y. Top: $P_X = 25$, $P_R = 100$ mW. Middle: $P_X = 50$, $P_R = 50$ mW. Bottom: $P_X = 100$, $P_R = 25$ mW.

CHAPTER 3

COOPERATIVE UWB LOCALIZATION AND TRACKING

3.1 Background and Contributions

Node localization and tracking has broad interest and applications in wireless sensor networks, as well as the field of robotics. Such networks must frequently operate in Global Positioning System (GPS)-denied environments, or where GPS is cost or energy prohibitive, thus motivating the search for other methods [24, 25]. Also, pre-surveyed node positions may not be available, creating an anchor free, or reference-less problem. In such situations, the use of ultra-wideband (UWB) radio techniques has attracted interest [26, 27]. UWB ranging has the advantage of very high temporal resolution and bandwidth, making it resistant to multipath propagation and interference common in many environments. This leads to more accurate ranging, a key input to most localization techniques. For these reasons, we confine our focus in this chapter to two-way time-of-flight (TOF) cooperative ranging between UWB radios as the source of inter-node ranging data.

To estimate node positions, a popular approach to the cooperative relative localization problem is to use a technique known as multidimensional scaling (MDS). In MDS, high dimensional "dissimilarity" data is mapped into a lower (usually 2) dimensional set for easier visualization [28]. In the localization context, the dissimilarity data is a set of pairwise range measurements between nodes, that is, their dissimilarity in location. The MDS solution maps this set of ranges to a set of points in the plane in a way that minimizes a particular *stress function*. Since only pairwise range measurements are used, in the most general case a relative map is formed without the use of anchor nodes, such that the distance between nodes is preserved as much as possible. The relative map represents the true positions up to a flip/rotation and possible translation.

There has been significant work in the literature on using MDS as an approach to localization and tracking, particularly when anchor nodes are available [29, 30, 31]. In [32], a weighted stress function incorporating prior node position information is proposed. Other authors have emphasized distributed approaches by map stitching [33, 34] or dealing with missing data inherent in partially connected networks [35, 36, 37]. In [38], subspace tracking was used to track relative changes in node positions given their respective range measurements. However, without pre-surveyed anchor nodes, these methods either cannot be used, or will present flip/rotation ambiguities between time steps in a mobile system. This is an inherent shortcoming of MDS without anchors; the relative maps produced at different times are not comparable.

We address this shortcoming by proposing a reference-free method to track the relative positions of nodes in a network over time through fusion of range measurements and odometry data[1]. Both the range and odometry data are placed into the MDS framework in a manner that allows solving jointly for the trajectory of all nodes. In MDS, range measurements represent dissimilarity values between nodes in a given time step, while odometry data represents dissimilarity between the *same* node at two different time steps. Thus the odometry data connects inter-node range measurements across time, allowing for a joint solution using all the available data. Other data fusion approaches to localization exist in the literature, e.g. [39, 40, 41, 42]. However, these approaches all rely on anchor nodes to function, and do not utilize the MDS paradigm.

Our approach has several advantages, in addition to removing the need for anchor nodes. First, all available data is used to jointly estimate each node's trajectory, reducing the effects of noise on individual measurements. Second, we take a non-parametric approach to stress function minimization, which needs few assumptions about the environment in which this method is used. No state-space assumptions or statistical measurement models need be determined; these are required for extended or unscented Kalman filters, for

[1]Chapter sections published in [4, 5], © IEEE 2014. Reproduced with permission.

example. Third, odometry data is commonly available on many platforms, often with high accuracy. For example, encoder wheel measurements are commonly used for dead reckoning on mobile robot platforms, and inexpensive inertial navigation systems (INSs) are used on other types of mobile nodes. Fourth, our formulation can easily account for missing data, as well as differences in the relative quality of the various measurements. Finally, the joint estimation of position across multiple time steps eliminates the issue of flip/rotation ambiguities between those time steps. The relative reference frame is preserved for the time values estimated.

In this chapter we first consider our algorithm in "batch" form, i.e., we assume that data is collected over time and post-processed to estimate the sequence of node positions. These results are covered fully in Section 3.2. In Section 3.2.1, we give the mathematical treatment of the proposed method. The results of a comprehensive simulation for varying node count, time steps, and noise is found in Section 3.2.2. The results of our algorithm applied to real data gathered by the Cognitive Spectrum Operations Testbed (CSOT) follow in Section 3.2.3.

After establishing the performance of the proposed methods in batch form, we extend the algorithm to a cooperative tracking scenario. In this case, the sequence of node positions is estimated in real time as the data is collected. The tracking extension is covered in Section 3.3. The algorithmic components are developed in Section 3.3.1, simulation results are introduced in Section 3.3.2, and further CSOT test results are discussed in Section 3.3.3. Finally we offer our conclusions in Section 3.4.

3.2 MDS with Range and Odometry

3.2.1 Mathematical Techniques

We consider the problem of estimating the positions of N nodes in each of K time steps. If the position of node n at time k is given by $\mathbf{s}_n^{(k)} = \begin{bmatrix} s_{n,x}^{(k)} & s_{n,y}^{(k)} \end{bmatrix}^T$, then we can compile the

NK position vectors into the matrix

$$\mathbf{S} = \left[\mathbf{s}_1^{(1)}\mathbf{s}_2^{(1)}\ldots\mathbf{s}_N^{(K)}\right]^T \in \mathbb{R}^{NK\times 2}, \tag{3.1}$$

where a matrix is used instead of a vector by convention in the MDS literature.

We assume that a set of $N(N-1)$ pairwise range measurements are available at each time step, arranged in matrix $\mathbf{R}^{(k)} \in \mathbb{R}^{N\times N}$ such that $\left[\mathbf{R}^{(k)}\right]_{i,j} = r_{ij}^{(k)}$ is the range estimate between nodes i and j at time step k. The main diagonal of $\mathbf{R}^{(k)}$ is equal to zero by definition. The range values are assumed to be already estimated from some method such as TOF, received signal strength (RSS), etc. Similarly, we assume a set of odometry distance measurements are available for each node, which represent the distance traveled by that node between time steps $k-1$ and k. These are arranged into the diagonal matrix $\mathbf{D}^{(k)} \in \mathbb{R}^{N\times N}$, such that $\left[\mathbf{D}^{(k)}\right]_{i,i} = d_i^{(k)}$ is the distance traveled by node i between times $k-1$ and k. The $d_i^{(k)}$ values are estimated from encoder wheel pulses, INS, etc. In this work we assume that the off-diagonal elements of $\mathbf{D}^{(k)}$ are unknown and set to zero.

The total data gathered are assembled into a block tridiagonal matrix $\mathbf{\Delta} \in \mathbb{R}^{NK\times NK}$. For example, if the network consists of 4 nodes, and data is gathered across 3 time steps, then

$$\mathbf{\Delta} = \begin{bmatrix} \mathbf{R}^{(3)} & \mathbf{D}^{(3)} & \mathbf{0} \\ \mathbf{D}^{(3)} & \mathbf{R}^{(2)} & \mathbf{D}^{(2)} \\ \mathbf{0} & \mathbf{D}^{(2)} & \mathbf{R}^{(1)} \end{bmatrix} \tag{3.2}$$

is a 12×12 matrix of 4×4 blocks. Note that stepping between blocks in Δ is equivalent to stepping between time values k.

Taking the weighted stress function approach of [32], we seek the set of positions $\hat{\mathbf{S}}$ that minimize the following stress function:

$$\mathcal{J}(\hat{\mathbf{S}}) = \sum_{i=1}^{NK}\sum_{j=1}^{NK}[\mathbf{W}]_{i,j}\left([\Delta]_{i,j} - \left[d(\hat{\mathbf{S}})\right]_{i,j}\right)^2, \tag{3.3}$$

where we have omitted the term representing prior knowledge of node positions, because none is assumed here. In (3.3), the matrix $\mathbf{W} \in \mathbb{R}^{NK \times NK}$ is a matrix of non-negative scalar weights, and the function $d\colon \mathbb{R}^{NK \times 2} \rightarrow \mathbb{R}^{NK \times NK}$ maps the set of coordinates $\mathbf{S}$ into a matrix of pairwise distances with the same structure as $\mathbf{\Delta}$. That is,

$$\left[d(\hat{\mathbf{S}})\right]_{i,j} = \left(\left([\hat{\mathbf{S}}]_{i,:} - [\hat{\mathbf{S}}]_{j,:}\right)^T \left([\hat{\mathbf{S}}]_{i,:} - [\hat{\mathbf{S}}]_{j,:}\right)\right)^{1/2}. \tag{3.4}$$

The stress function (3.3) is both nonlinear and non-convex in the variable $\hat{\mathbf{S}}$. The most common technique for minimizing this function is known as scaling by majorizing a complicated function (SMACOF) [28], and involves transformation of the stress via majorizing functions. The algorithm is iterative, and usually offers quick convergence. We use the SMACOF algorithm in this work to minimize (3.3), with the addition of trying multiple random initial start configurations to help avoid local minima. It should also be noted that taking the weighted approach to MDS avoids the noise amplification caused by squaring the distance values in the classical non-weighted MDS solution.

The values in the weighting matrix $\mathbf{W}$ represent our relative confidence in the data values. It conveniently allows accounting for any missing data by simply setting the corresponding weight to zero, and thus will have no influence on the stress function (3.3). For the remaining measurements, traditional linear weighted least squares sets $[\mathbf{W}]_{i,j} = \frac{1}{\sigma_{ij}^2}$, where σ_{ij}^2 is the assumed variance of the corresponding measurement. However, the stress function (3.3) is not linear due to the distance mapping $d(\cdot)$, and thus this mapping does not strictly apply. In our simulations we have obtained better results by assigning weights based on the relative standard deviations. In this work, we assign weights by $[\mathbf{W}]_{i,j} = \frac{c}{\sigma_{ij}}$, with c set so that the smallest weight value equals 1 to avoid numerical instability. In the case where no a-priori information is known about measurement quality, then all measurement weights could be set to 1.

3.2.2 *Localization Simulation Results*

For our simulations, we have assumed that nodes begin in a 20×20 meter area, and move randomly such that the straight line distance traveled in the x and y directions at each time step is distributed uniformly between -5 and 5 meters. The variance in both the range and odometry measurements is assumed proportional to the actual distance, which is consistent with both measurement types. The proportionality for range and odometry are assumed known and denoted σ_r^2 and σ_d^2, respectively. That is, σ_r^2, σ_d^2 are the variances in the range measurements *per meter*. In the results, we compute the root mean squared error (RMSE) in position estimates by first aligning the estimated reference-free map with the true trajectory map via a Procrustean transformation [28]. An example estimated trajectory for a set of five nodes is shown in Figure 3.1.

We characterize the general performance of our algorithm through comprehensive simulations of our approach for various values of node count, time steps, and noise levels. For the first simulation, we measure the average RMSE of position estimates for different values of node count N and time steps K. The results are shown in Figure 3.2. From these results, we see that estimation accuracy generally improves with increasing N and *decreasing* K. As N increases, more range data is available at each time index, and more odometry values are available between time steps. However, as K increases while leaving N constant, the sparsity of Δ increases. Thus, more positions must be estimated relative to the amount of data, decreasing accuracy.

For our second simulation, we set $N = 8$ and $K = 4$, with the noise standard deviations σ_r, σ_d allowed to vary. The performance generally decreases as measurement uncertainty increases. We note that across most of the range of σ_d, our algorithm performs fairly consistently at $5 - 6$ dBmm above the range noise level.

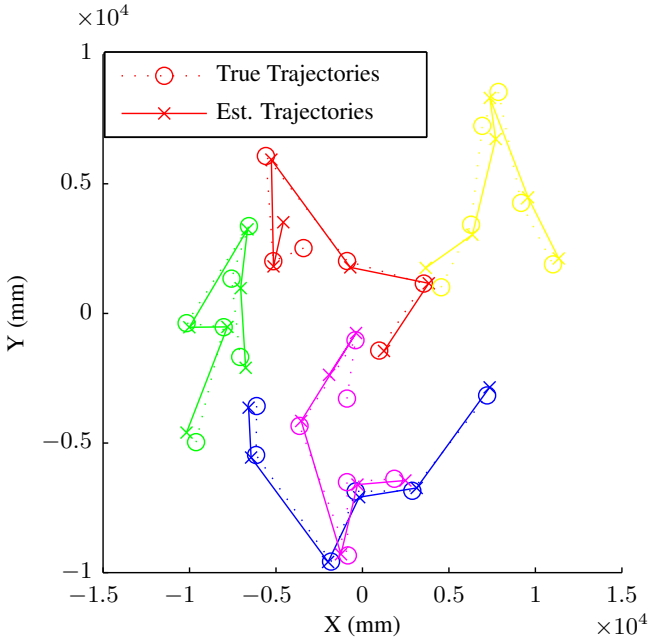

Figure 3.1: Simulated reference-free tracking solution for $N = 5$, $K = 6$, $\sigma_r = 100$ mm, $\sigma_d = 10$ mm. The true trajectories are shown for comparison, aligned via the Procrustean transformation. Position RMSE $= 428$ mm.

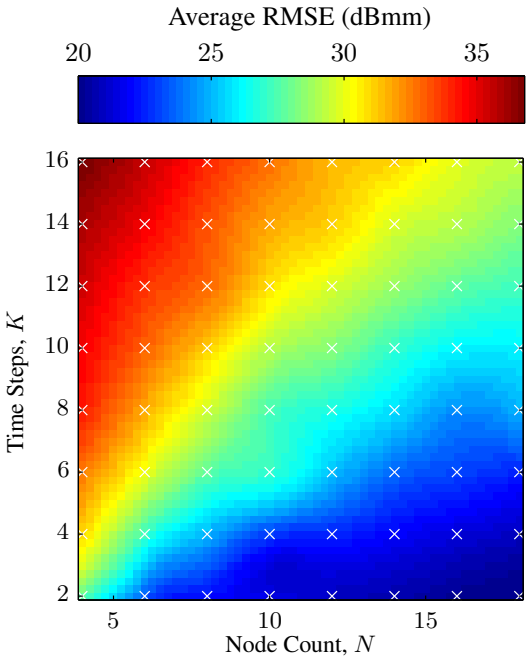

Figure 3.2: First comprehensive simulation results, RMSE vs. K, N. Noise levels: $\sigma_r = 100$ mm, $\sigma_d = 10$ mm.

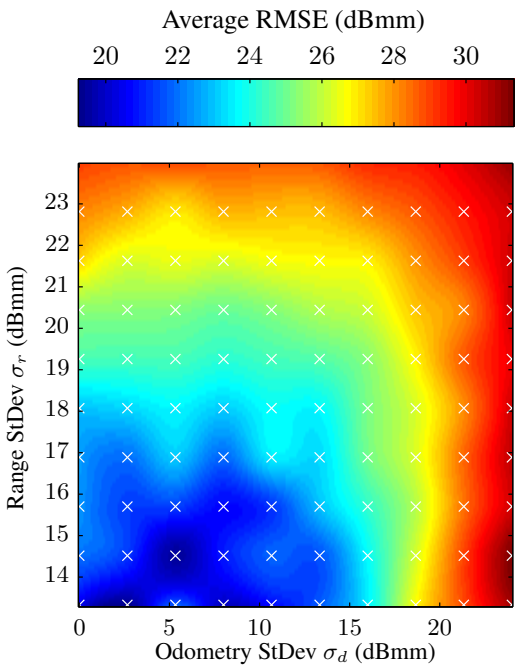

Figure 3.3: Second comprehensive simulation results, RMSE vs. σ_r, σ_d, where $N = 8$, $K = 4$.

3.2.3 Localization Results on Real Data

We have also tested our proposed tracking method on real range and odometry data gathered by the CSOT testbed. Originally introduced as RadioBOT in [2], the testbed features the ability to gather both highly accurate UWB range measurements and mobile robot odometry data. Each mobile node is equipped with two UWB antennas mounted above the robot on the left and right sides, respectively, spaced approximately 315 mm apart. The measured standard deviation of the UWB range measurement error is approximately $\sigma_r = 20$ mm, and is very stable with the distances measured. Odometry measurements are provided by the iRobot mobile base encoder wheels, with estimated standard deviation $\sigma_d = 5$ mm per meter traveled. Here we present the results of two measurement campaigns conducted in a laboratory hallway, as a proof of concept to show our algorithm's ability to estimate node trajectories from actual measured data. The test parameters are summarized in Table 3.1. The hallway test setup is shown in Figure 3.4. For Test I, three of the nodes

Table 3.1: CSOT localization campaign summary.

	Test I	Test II
Stationary Nodes	3	7
Mobile Nodes	5	1
Surveyed Data	Stationary	Stationary + mobile
Total time steps K	19	27
RMSE vs. Survey Data	18 mm	124 mm

remained stationary for the duration of the test, and their locations were surveyed to provide truth data. We stress that the tests are still reference-less, because the stationary node locations are not known to the algorithm. A complete set of pairwise range measurements was taken at each time step, and encoder wheel data gathered for each node's movement between time steps. The collected data were processed per our algorithm of Section 3.2, and the results of the tracking shown in Figure 3.5. The RMSE of the estimated positions is computed with the surveyed nodes after aligning the two maps, and was found to be 16 mm.

In Test II, seven of the nodes remained stationary in a cluster, while a single mobile node took a curved trajectory over a distance of approximately 10 m. Data was collected in the same manner as Test I, with the addition of surveying both the initial and final positions of the mobile node. The RMSE with all surveyed positions in this case was found to be 124 mm. We note the increase in error over Test I, as we are now comparing surveyed truth data for both stationary and mobile nodes. The test also took place over an increased number of time steps and over a larger distance.

3.3 Tracking with Range and Odometry

3.3.1 Tracking Algorithm

We now extend the results of Section 3.2 to consider real time tracking, estimating node positions sequentially as new data is collected. The mathematical development closely follows the notation and conventions established in Section 3.2. We again consider the

Figure 3.4: Initial hallway robot configuration for Test I.

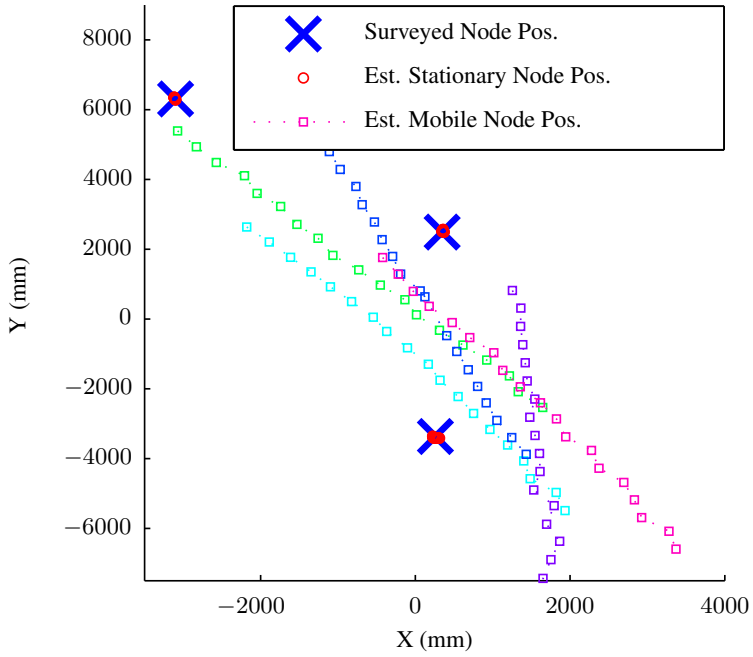

Figure 3.5: Test I tracking results. RMSE = 18 mm.

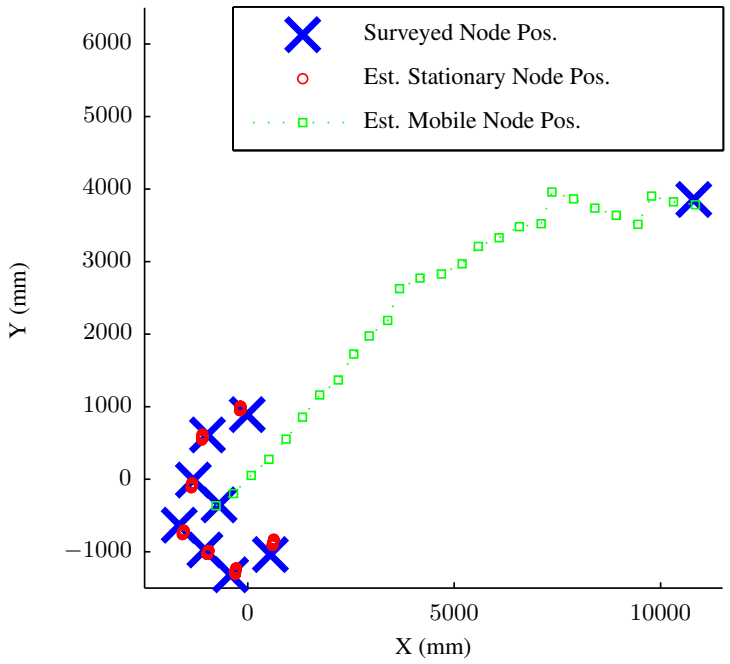

Figure 3.6: Test II tracking results. RMSE = 124 mm.

problem of estimating the positions of N nodes in each of K time steps. The position of node n in the xy plane at time k is given by $\mathbf{s}_n^{(k)} = \begin{bmatrix} s_{n,x}^{(k)} & s_{n,y}^{(k)} \end{bmatrix}^T$. The full tracking solution is once again given by compiling the NK position vectors into the matrix

$$\mathbf{S} = \begin{bmatrix} \mathbf{s}_1^{(0)} \mathbf{s}_2^{(0)} \dots \mathbf{s}_N^{(K-1)} \end{bmatrix}^T \in \mathbb{R}^{NK \times 2} . \tag{3.5}$$

We continue to use a matrix of position coordinates instead of a vector by convention in the MDS literature. The component matrices $\mathbf{R}^{(k)}$ and $\mathbf{D}^{(k)}$ are defined as in Section 3.2. As before, these matrices represent inter-node range values at time k and the intra-node ranges between times $k-1$ and k, respectively. The available data is compiled into a block-symmetric matrix

$$\mathbf{\Delta}^{(k)} = \begin{bmatrix} \mathbf{R}^{(k-1)} & \mathbf{D}^{(k)} \\ \mathbf{D}^{(k)} & \mathbf{R}^{(k)} \end{bmatrix} \in \mathbb{R}^{2N \times 2N} , \tag{3.6}$$

which contains the measured range values related to the unknown node positions

$$\mathbf{S}^{(k)} = \left[\mathbf{s}_1^{(k-1)}\mathbf{s}_2^{(k-1)}\dots\mathbf{s}_N^{(k)}\right]^T \in \mathbb{R}^{2N\times 2} \tag{3.7}$$

for two time steps. Constructing $\mathbf{\Delta}^{(k)}$ in this manner fits the definition of a *dissimilarity matrix* from the MDS literature. That is, elements of $\mathbf{\Delta}^{(k)}$ represent the dissimilarity, or distance between nodes in the plane for both the current and previous time step. Note that matrix $\mathbf{\Delta}^{(k)}$ is of fixed size given the number of nodes N, i.e., $\mathbf{\Delta}^{(k)}$ consists of exactly two time steps. This is in contrast to Section 3.2, where the size of $\mathbf{\Delta}$ varies with the total size of the experiment.

To solve for positions $\mathbf{S}^{(k)}$, we continue to take the weighted stress function approach of [32]. We seek the set of positions $\hat{\mathbf{S}}^{(k)}$ that minimize the stress function

$$\mathcal{J}(\hat{\mathbf{S}}^{(k)}) = \sum_{i=1}^{2N}\sum_{j=1}^{2N}\left[\mathbf{W}^{(k)}\right]_{i,j}\left(\left[\mathbf{\Delta}^{(k)}\right]_{i,j} - \left[d(\hat{\mathbf{S}}^{(k)})\right]_{i,j}\right)^2. \tag{3.8}$$

In (3.8), the matrix $\mathbf{W}^{(k)} \in \mathbb{R}^{2N\times 2N}$ is a matrix of non-negative scalar weights, and the function $d\colon \mathbb{R}^{2N\times 2} \to \mathbb{R}^{2N\times 2N}$ maps the set of coordinates $\hat{\mathbf{S}}^{(k)}$ into a matrix of pairwise distances with the same structure as $\mathbf{\Delta}^{(k)}$. That is,

$$\left[d(\hat{\mathbf{S}}^{(k)})\right]_{i,j} = \sqrt{\left([\hat{\mathbf{S}}^{(k)}]_{i,:} - [\hat{\mathbf{S}}^{(k)}]_{j,:}\right)^T\left([\hat{\mathbf{S}}^{(k)}]_{i,:} - [\hat{\mathbf{S}}^{(k)}]_{j,:}\right)}. \tag{3.9}$$

Note that (3.8) and (3.9) are very similar to those defined in Section 3.2. Here we have merely added the time index k and corrected the limits of summation for the tracking problem.

We now apply the MDS and measurement framework outlined above to the tracking of node positions over time. Unlike many localization and tracking methods, our procedure does not require any anchor nodes, nodes for which exact coordinates are known a-priori and do not move during the session. In this work we will only assume the existence of

at least three *stationary nodes*, nodes which are known not to move during the tracking. The stationary nodes' positions need not be known and are estimated. This is a stronger assumption not made in Section 3.2, though we will point out how it might be avoided.

To begin tracking, an initial reference frame must be established that will be maintained for the entire session, because in general MDS-based algorithms produce relative maps that are only equivalent up to a rotation, reflection, and translation. Assume without loss of generality that the first $m \geq 3$ nodes are the stationary references. The first set of inter-node range measurements are taken and assembled into matrix $\mathbf{R}^{(0)}$. Applying the SMACOF algorithm will produce an initial set of N position estimates $\hat{\mathbf{S}}^{(0)}_{ref} \in \mathbb{R}^{N\times 2}$. The $N - m$ mobile nodes each then proceed to move independently; the measured intra-node travel distances are compiled into matrix $\mathbf{D}^{(1)}$. At the next time step matrix $\mathbf{R}^{(1)}$ is filled with the new set of inter-node ranges. Matrix $\mathbf{\Delta}^{(1)}$ can now be assembled as in (3.6). Again applying SMACOF will produce estimated node coordinates $\hat{\mathbf{S}}^{(1)}$.

Since MDS-based algorithms such as SMACOF produce relative maps, node coordinates are preserved only up to an orthogonal transformation (rotation/reflection/translation). Thus maps produced by successive runs of SMACOF are not generally comparable. However, note that $\hat{\mathbf{S}}^{(1)}$ contains a position estimate for each node at both time steps $k = 0$ and $k = 1$, creating an overlap. We also know that there are at least m node positions in common between $\hat{\mathbf{S}}^{(0)}_{ref}$ and $\hat{\mathbf{S}}^{(1)}$. We use this information to derive an orthogonal transformation which cancels out the ambiguity produced by successive SMACOF operations. That is, we seek a transformation that will optimally "map back" each new set of position estimates onto our original reference frame established by $\hat{\mathbf{S}}^{(0)}_{ref}$:

$$\hat{\mathbf{S}}'^{(k)} = s\hat{\mathbf{S}}^{(k)}\mathbf{T} + \mathbf{1}_{2N}\mathbf{t}^T\,, \tag{3.10}$$

for scale factor s, rotation/reflection matrix operator $\mathbf{T}$, and translation vector $\mathbf{t}$. Finding these values is known as a Procrustean similarity transformation [28]. It can be shown that

if $\mathbf{Y}$ is the $m \times 2$ set of stationary node positions from $\hat{\mathbf{S}}^{(k)}$, and $\mathbf{X}$ is the $m \times 2$ set of stationary nodes from $\hat{\mathbf{S}}^{(0)}_{ref}$, then

$$\mathbf{C} = \mathbf{X}^T \left(\mathbf{I}_m - m^{-1}\mathbf{1}_m\mathbf{1}_m^T\right)\mathbf{Y}$$

$$\mathrm{svd}(\mathbf{C}) = \mathbf{U}\mathbf{\Sigma}\mathbf{V}^T$$

$$\mathbf{T} = \mathbf{V}\mathbf{U}^T \in \mathbb{R}^{2\times 2} \tag{3.11}$$

$$s = \frac{\mathrm{Tr}\left(\mathbf{X}^T\left(\mathbf{I}_m - m^{-1}\mathbf{1}_m\mathbf{1}_m^T\right)\mathbf{Y}\mathbf{T}\right)}{\mathrm{Tr}\left(\mathbf{Y}^T\left(\mathbf{I}_m - m^{-1}\mathbf{1}_m\mathbf{1}_m^T\right)\mathbf{Y}\right)} \in \mathbb{R} \tag{3.12}$$

$$\mathbf{t} = m^{-1}\left(\mathbf{X} - s\mathbf{Y}\mathbf{T}\right)^T\mathbf{1}_m \in \mathbb{R}^{2\times 1} \tag{3.13}$$

will minimize the squared error after applying the transformation. By applying the similarity transformations derived from the stationary nodes, the original reference frame can be maintained during tracking for all nodes. This process of gathering range and odometry data, performing SMACOF, then aligning the new map continues for all time steps k. The procedure is summarized in Algorithm 1.

As stated before, the algorithm assumes the existence of at least $m \geq 3$ stationary nodes which are used to align successive maps. However, it is clear from the definition of $\mathbf{\Delta}^{(k)}$ in (3.6) that two sets of position estimates are being produced at each iteration: one for time $k-1$ and one for time k. Thus all N position estimates from time $k-1$ could be used to produce the similarity transformation vectors (Algorithm 1 lines 11 and 12) for time step k. If this were done, then all nodes could be mobile. However, we would be applying the transformation using successively estimated sets of points. Thus, position errors would accumulate over time, making this analogous to a type of dead reckoning localization.

3.3.2 Simulation Results

Here we present comprehensive simulations to demonstrate the algorithm's performance. We assume that nodes move within an approximately 20×20 meter area. The movements at each time step occur according to a constant velocity model, with velocity perturbation

Algorithm 1: MDS Tracking with Range and Odometry

Data: Range and odometry measurements $\mathbf{R}^{(k)}$, $\mathbf{D}^{(k)}$
Result: Coordinates $\hat{\mathbf{S}}$ estimating true node positions $\mathbf{S}$

begin
  Initialize $k = 0$: observe ranges $\mathbf{R}^{(0)}$;
  $\hat{\mathbf{S}}^{(0)}_{ref} \leftarrow \left[\hat{\mathbf{S}}\right]_{1:N,:} \leftarrow \text{SMACOF}\big(\mathbf{R}^{(0)}, \mathbf{W}^{(0)}\big)$;
  $\mathbf{X} \leftarrow \left[\hat{\mathbf{S}}^{(0)}_{ref}\right]_{1:m,:}$;
  for $k = 1$ **to** $K - 1$ **do**
    observe ranges $\mathbf{R}^{(k)}$;
    observe odometry $\mathbf{D}^{(k)}$;
    assemble matrix $\mathbf{\Delta}^{(k)}$ in (3.6) ;
    $\hat{\mathbf{S}}^{(k)} \leftarrow \text{SMACOF}\big(\mathbf{\Delta}^{(k)}, \mathbf{W}^{(k)}\big)$;
    $\mathbf{Y} \leftarrow \left[\hat{\mathbf{S}}^{(k)}\right]_{1:m,:}$;
    compute s, $\mathbf{T}$, $\mathbf{t}$ by (3.11), (3.12), (3.13) ;
    $\hat{\mathbf{S}}'^{(k)} \leftarrow s\hat{\mathbf{S}}^{(k)}\mathbf{T} + \mathbf{1}_{2N}\mathbf{t}^T$ by (3.10) ;
    store current solution: $\left[\hat{\mathbf{S}}\right]_{Nk+1:Nk+N,:} \leftarrow \hat{\mathbf{S}}'^{(k)}$;
  end
end

$\sim N(0, \sigma_v^2)$. The standard deviation of velocity perturbations is $\sigma_v = 200$ mm/s at each step. The error variance in both the range and odometry measurements is assumed proportional to the actual distance, which is consistent with both measurement types. This proportionality for range and odometry are assumed known and denoted σ_r^2, σ_d^2 respectively. That is, σ_r^2, σ_d^2 are the variances in the range measurements *per meter*. In all cases there were $m = 3$ stationary nodes, and 240 simulations were run for each data point.

From the simulated movements and measurement data, we perform three separate estimation algorithms for comparison. To benchmark the results, we first perform tracking using the well-known extended Kalman filter (EKF). The EKF assumes that the *exact* coordinates of the stationary nodes are known. Thus, they become traditional anchor nodes for EKF tracking. The EKF makes use of range data only, but also assumes the same motion model described above, tracking position and velocity. That is, there is no mismatch between the EKFs state-space model and the model generating the true node trajectories.

The EKF also assumes that the initial positions of the nodes are known to within one meter. We also perform tracking using our proposed tracking algorithm, both with and without odometry data.

For the first simulation, we measure the average RMSE of position estimates for different values of node count N over $K = 20$ time steps, with noise levels $\sigma_r^2 = (75 \text{ mm})^2$, $\sigma_d^2 = (10 \text{ mm})^2$. The results are shown in Figure 3.7. From these results, we see that estimation accuracy generally improves with increasing N. As N increases, more range data is available at each time index, and more odometry values are available between time steps. The EKF shows a much stronger dependence on node count, actually overtaking our approach for $N \geq 14$ if odometry data is not used.

Our second simulation fixes $N = 8$, $K = 20$ time steps, and $\sigma_d = 20$ mm, with the noise standard deviation σ_r allowed to vary. The results are plotted in Figure 3.8. The performance of course generally decreases as measurement uncertainty increases. Our algorithm consistently outperforms the EKF, though the RMSE increases more slowly for the latter. The EKF has an internal motion model, which is favored more as the measurement error becomes large. Of course, if the true motion of the nodes does not match the internal assumptions, then this will not help. Also, the EKF must "lock on" to the trajectories of the nodes, which may take a few samples. We note that our proposed approach does not have these problems, and measurement accuracy is almost solely a function of the measurement error. The performance difference between the two MDS approaches increases as the range measurement error increases. If the algorithm has access to the more reliable odometry data, it will be weighted more strongly, resulting in the observed better performance.

3.3.3 Tracking Results on Real CSOT Data

We have tested the same three tracking methods using real UWB range and encoder wheel odometry data gathered from CSOT. The testbed capabilities were originally introduced

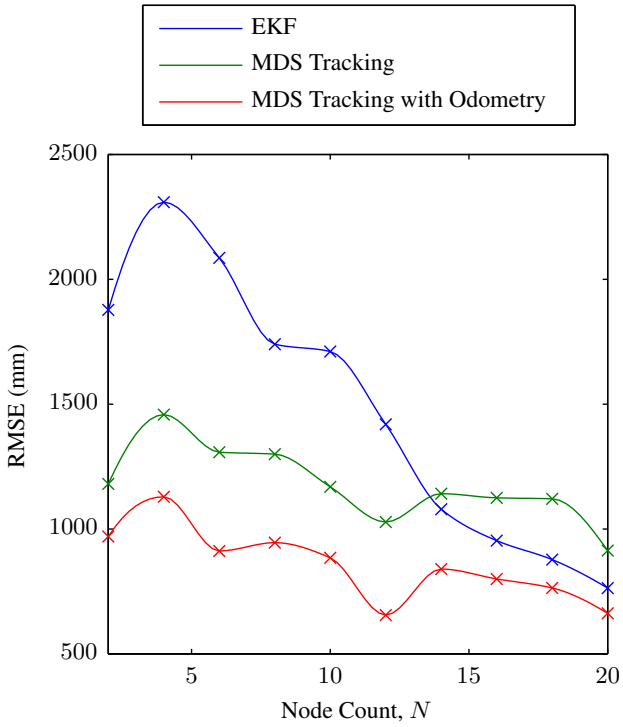

Figure 3.7: First comprehensive tracking simulation results, position RMSE vs. number of nodes N over $K = 20$ time steps. Noise levels: $\sigma_r^2 = (75 \text{ mm})^2$, $\sigma_d^2 = (10 \text{ mm})^2$.

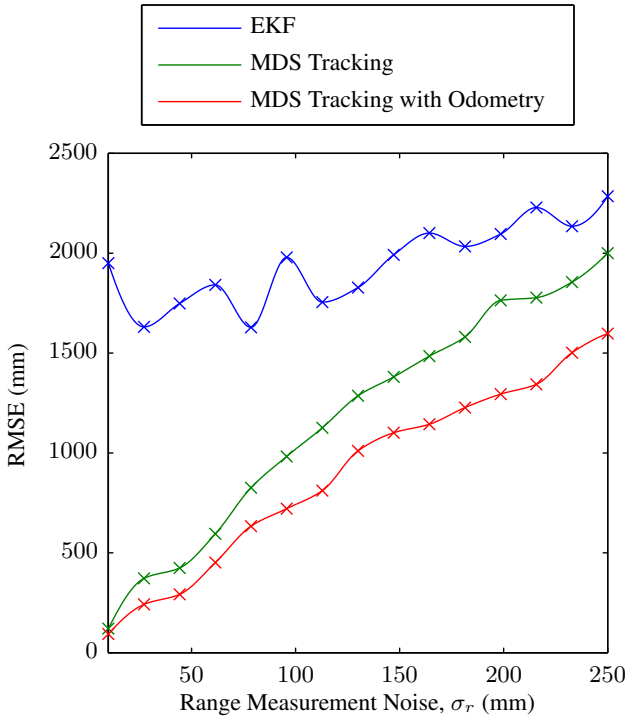

Figure 3.8: Second comprehensive tracking simulation results, position RMSE vs. range measurement noise for $N = 8$ nodes over $K = 20$ time steps, with $\sigma_d = 20$ mm.

Figure 3.9: CSOT initial setup prior to Test I.

in Chapter 2 for producing area-wide spectrum maps. Each CSOT node's UWB ranging radio is capable of ~ 4.7 cm RMSE range accuracy. The ranging radio separately utilizes two UWB antennas mounted at the top of the robot, spaced 315 mm apart. Odometry data is gathered by the wheel encoders built into the mobile base, with comparable accuracy to the UWB radios over short distances. A photo of the system setup is shown in Figure 3.9.

Figure 3.10 displays the results of three measurement campaigns performed in a laboratory hallway to measure real-world tracking performance. The same EKF of Section 3.3.2 is used again for comparison, and assumes that the standard deviation of velocity change is $\sigma_v = 200$ mm/s at each step. The tests represent a range of values for stationary and mobile nodes, movement paths, and time steps. While the first three stationary node positions were known to the EKF, we stress that our MDS algorithm assumes only that they were stationary. The true position of each node was surveyed at every time step, providing a full set of truth data for comparison. A summary of the test parameters is shown in Table 3.2.

Each test was designed to vary the number of moving nodes as well as movement patterns. Test I had the most mobile nodes, and the most consistent movement between

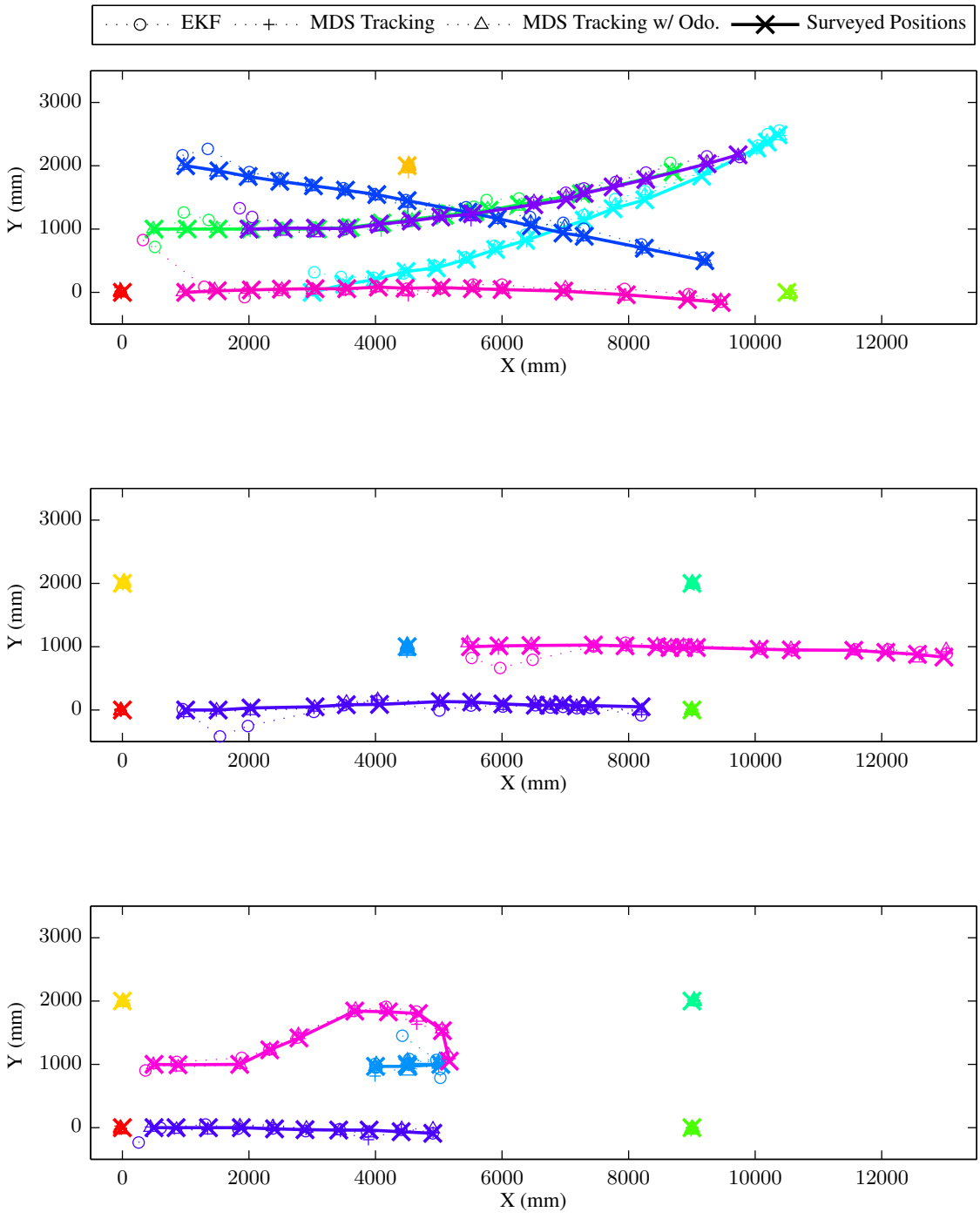

Figure 3.10: CSOT testbed tracking results for Test I (top), Test II (middle) and Test III (bottom).

Table 3.2: CSOT tracking campaign summary.

	Test I	Test II	Test III
Stationary nodes	3	5	4
Mobile nodes	5	2	3
Total time steps K	15	15	10
RMSE: MDS (w/ odo.)	20 mm	15 mm	19 mm
RMSE: MDS (no odo.)	23 mm	16 mm	24 mm
RMSE: EKF	91 mm	68 mm	67 mm
Avg. range error stdev., σ_r	30 mm		
Avg. odo. error stdev., σ_d	27 mm (per meter)		

time steps. Each robot moved approximately $0.5 - 1$ meters at each time step. All three algorithms performed very well here, with RMSE on the order of centimeters as shown in Table 3.2.

For Test II, only two nodes were mobile, leaving the rest stationary. However, the distance traveled by the mobile nodes was more variable vs. Test I. Movement distances in this case varied from $0.2 - 1$ meters. The results show a corresponding decrease in RMSE for all three tracking solutions, indicating that more stationary nodes can improve performance. The relative performance between tracking methods is almost identical to Test I.

Test III utilized three mobile nodes, with distances ranging from $0 - 1$ meters. One node took a curved path, one a very straight path, and the third only moved half of the time. These differences had little effect on the tracking errors. Overall, our MDS-based tracking using range and odometry is able to consistently outperform the EKF on actual measured UWB and encoder data. We do note that utilizing the odometry data in our tests provides only marginal benefit. In our tests the UWB range and odometry data errors are very close in magnitude, making these test results consistent with the far left region of Figure 3.8.

3.4 Conclusion

In this chapter we have proposed a novel reference-free means of estimating the trajectories of mobile nodes by adapting the popular MDS paradigm to use both inter-node range

measurements and intra-node odometry data. The odometry data is used to "link" ranging data, and the resulting MDS localization of node positions, across time steps. Unlike other methods, our approach allows estimation of a node's trajectory jointly with all others, requires few assumptions, and preserves the reference frame across time steps.

We then extended this localization framework to real time tracking of mobile nodes. The extension enables the tracking to be performed as new data is gathered. The tracking algorithm assumes only the existence of stationary nodes with which to relate position estimates gathered over time. We have presented simulation and actual testbed results to demonstrate performance exceeding that of the canonical EKF. Our algorithm also has the substantial advantages of few assumptions, joint estimation, and elimination of pre-surveyed anchor node positions.

Future research could extend the algorithm further to drop the assumption of stationary nodes. As previously discussed, the tracking would become analogous to a dead reckoning approach. The performance of such a scheme could be investigated. A non-centralized approach to estimation would also be helpful for use in distributed or power restricted networks.

CHAPTER 4

UWB TOMOGRAPHIC IMAGING IN UNCALIBRATED NETWORKS

4.1 Background and Contributions

A key goal, particularly for mobile networks, is for the entire system to be spatially aware of its surroundings beyond the traditional localization of node positions. A networked robotic system may need to learn the locations of obstacles to be avoided, as in a simultaneous localization and mapping (SLAM) algorithm [43, 44]. Environmental monitoring applications may additionally require the network to know the presence of people entering or leaving an area, even tracking their movements [45]. Networks employing radio frequency (RF) communication may need to estimate channel quality between points in space, as in [46]. Finally, a mobile network may benefit from environmental map information in areas which are visually occluded behind walls or other obstructions. Such through-wall images could be used by emergency personnel or soldiers in a combat situation [47].

Tomographic imaging is a promising means for achieving the aforementioned goals. Most generally, tomography is the process of reconstructing an image of some environment by viewing it through slices or sections. In practice, this usually means sending some type of energy-carrying signal through an object or area, and observing attenuation in the signal at another position. Over many spatially diverse measurements, an appropriate inverse model may be applied to estimate the environment. Use of RF waves as the measurement phenomenon is attractive due to their potential to propagate over wide areas and penetrate a variety of materials. Early efforts in RF tomographic techniques attempted to locate discontinuities in the ground, such as coal seams or tunnels [48, 49, 50, 51].

In the past decade, the proliferation of low cost wireless sensor networks has stimulated additional research interest in tomographic area mapping and tracking. The term radio

tomographic imaging (RTI) has been used to describe the use of RF signals to estimate the shadowing loss due to static or moving objects [10]. RTI is posed as a case of device-free localization, as the objects to be located do not carry transmitters or receivers [52]. In [10], the authors proposed to image changes in RF attenuation from a measured baseline using only received signal strength (RSS), a measurement available to almost any radio receiver. In [53], measurements of RSS variance were used for tracking only the moving objects in an environment, emphasizing the through-wall capabilities of RTI. Methods for addressing regularization of the inverse problem of image reconstruction were explored in [54].

Other authors have pursued the tomographic imaging of the purely static features of an environment. Knowledge of the static shadowing environment is useful for mapping obstacles, estimating link shadow fading [55], and even informing localization algorithms [56]. In [57], the author utilized a pair of robots moving in coordinated patterns to collect RSS data for a variety of attenuating structures. Compressive sampling techniques were used to reconstruct images using a reduced number of measurements. [58] explored the relationship between random and coordinated spatial sampling patterns using the same robotic testbed. In [59], the authors demonstrated the benefits of sensor fusion for observable and unobservable features, combining laser and RF measurements.

While the aforementioned works have focused on narrow-band RF imaging, ultra-wideband (UWB) pulse radio techniques have also attracted interest. A UWB radio signal is often defined as having a bandwidth greater than 20% of the center frequency, or 500 MHz, whichever is greater. We also distinguish a UWB signal from other wideband signals, such as spread spectrum, by the impulse nature of UWB. That is, UWB signals achieve high bandwidth via very short duration pulses of very low duty cycle. The resulting short spatial extent of the waveforms results in several advantages, namely high range resolution, interference resistance, and multipath signal rejection [60].

These advantages have led to applications in traditional radar tracking, through-wall imaging, and localization. In fact, radar based approaches dominate the UWB literature

for imaging objects occluded by walls, e.g. [61, 62, 63, 64]. For indoor object detection and tracking, a holistic design of the UWB sensor network is considered in [65], and selection of representative measurements is addressed in [66]. UWB signals have even been employed for the remote monitoring of human breathing [67]. In addition to imaging and tracking, UWB has shown promise for the precise localization of nodes in sensor networks where GPS is unavailable. Accurate time-of-arrival (TOA) information, and even two-way time-of-flight (TOF) measurements made by UWB radios can resolve the distances between cooperative nodes, to which a localization algorithm may be applied [27, 24, 4, 5].

In this chapter, we address the RTI problem for imaging the static features and obstacles in the environment using UWB signaling techniques in a realistically deployable mobile network[1]. Our approach has several advantages, and seeks to address some problems with practical implementation of RTI systems. The first problem is mitigation of multipath signal effects which are detrimental to tomographic models which consider only the line-of-sight (LOS) signal path. As the authors of [68] showed, small scale multipath effects can easily exceed the shadowing effects we are interested in, showing up as additional noise in the measurements. We address this issue by using the large signal bandwidth of UWB to clearly separate the LOS signal path from the reflected multipath signal energy, by using a direct-path signal strength (DPSS) metric. Doing so is highly beneficial for applying a linear tomographic projection model along the LOS, and employing a straightforward path loss model even in multipath rich indoor environments. The authors of [57, 58, 59] mitigated these multipath effects using high gain directional antennas, which were kept oriented toward each other at all times. Our approach can be performed with basic, omni-directional broadband antennas, thus achieving the multipath separation capability regardless of the locations or antenna orientations of the nodes. This is important for scaling the network beyond a single pair of nodes, where reorienting antennas across the many

[1]Chapter sections published in [6], © IEEE 2015. Reproduced with permission.

links would become intractable.

Second, we address the calibration issue which is present in static object imaging for RTI. When imaging static objects, the shadowing losses of interest must be separated from the path losses due to link distance, the multipath signal effects, as well as the systematic effect of each link. Differences in transmit power, cable lengths, antenna gain, receiver sensitivity, etc. all introduce an unknown bias for *each* link in the network. Some authors, e.g. [69, 70] have addressed this problem for tracking moving objects, where only changes in RSS are measured. Others [71, 10] collect baseline data for static nodes in an "empty" area, then insert the shadowing objects to be measured. Still others [57, 58, 59] have only a single mobile link to characterize. However, as the network scales beyond even a couple of nodes, individual characterization of each link prior to deployment may be infeasible. During deployment, a given mobile link may not know if or when it is being shadowed by objects, making simple online calibration difficult. We propose to jointly estimate both the unknown spatial shadowing due to objects, as well as the unknown link bias and system path loss parameters. We do this under the framework of a linear mixed effects model. The problem is convex, which leads to efficient numerical solution methods. To overcome the underdetermined nature of the tomography problem, we implement a regularization technique known as the elastic net (EN). This allows the inclusion of the a-priori constraints of image pixel sparsity, as well as assumed pixel spatial correlation.

Chapter 4 is organized into sections as follows. Section 4.2 describes our use of the UWB signal to isolate direct path signal energy for measurements, as well as modeling the signal propagation. In Section 4.3 we describe the tomographic projection model used to map an image on to the space of measured data. Our mixed-effects image reconstruction model is detailed in Section 4.4. We derive performance bounds for the model and test its performance in Sections 4.5 and 4.6, respectively. The results of our tomographic experiments are displayed in Section 4.7. Finally, we conclude and discuss future work in Section 4.8.

4.2 UWB Sampling, Measurement, and Propagation

4.2.1 Time Domain Direct Sampling

Since a UWB signal pulse is very short in both temporal and spatial extent, it will therefore occupy a large bandwidth in the frequency domain. However, the total transmitted signal power may be quite small (< -14.8 dBm in our testing). This is generally to comply with regulations governing UWB transmissions; for example the Federal Communications Commission (FCC) requires the power spectrum to be below -41.3 dBm/MHz. This low limit gives a UWB transmission near noise-level characteristics when viewed from the frequency domain, quite unlike narrowband communication signals. As a result, UWB signals are generally analyzed directly from samples in the time domain. This of course requires relatively high sampling rates in order to satisfy the Nyquist criterion. For example, the P410 UWB radio from Time Domain[2] used in our experiments has an effective sampling period of 61 ps.

Figure 4.1 shows an example idealized pulse transmitted from the UWB radio. The pulse is designed as a bandpass signal with center frequency 4.3 GHz and bandwidth 2.2 GHz, with power level conforming to FCC requirements. The transmitted signal is sampled by another UWB transceiver and the received pulse is shown in the bottom plot of Figure 4.1. Both transmitter and receiver are operating in a high multipath indoor environment. The many surfaces in a multipath environment produce signal reflections that arrive at the receiver at different times. In fact, a majority of the received signal's energy is due to multipath propagation. However, the shortest path along the LOS between transmitter and receiver arrives first, and is clearly separated from the reflected energy by direct sampling in the time domain. This is the motivation for our definition and use of direct-path signal strength, described below.

[2]Time Domain Corporation, Huntsville, AL. Available at: `http://www.timedomain.com`

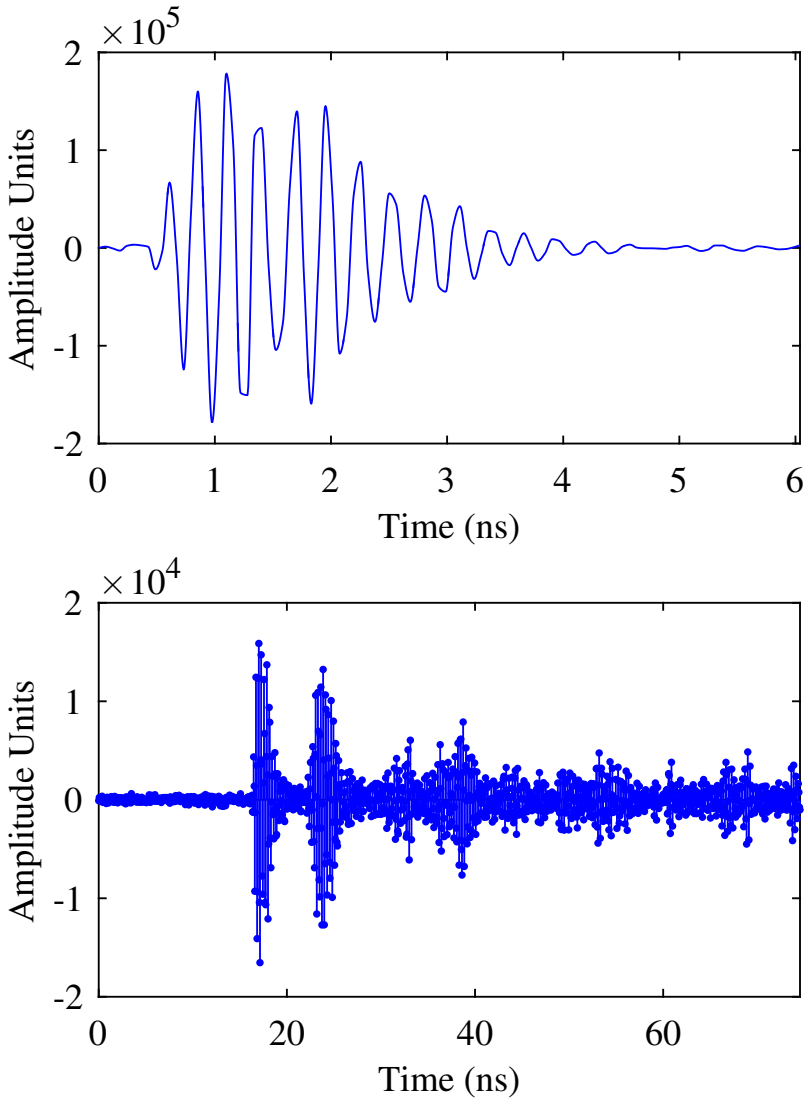

Figure 4.1: Top: Idealized transmitted UWB pulse signal. Bottom: Actual time domain received samples in a high multipath indoor environment at a distance of 10 meters. Amplitude is the raw ADC/DAC value, assumed proportional to voltage.

4.2.2 *Direct-Path Signal Strength*

The ability to separate the LOS and multipath signal energy is crucial, since a linear tomographic projection only models shadowing loss along the LOS. If not rejected, the multipath energy creates a rapidly fading channel, and the RSS variance can become extremely large, as noted in [68]. The result is unacceptably noisy measurements for tomographically estimating the large-scale shadowing loss due to objects along the LOS. To measure the LOS-only signal strength, we make use of the DPSS metric. Originally defined in [72], the DPSS was empirically determined to provide the best measure of signal strength along the LOS path. The metric is defined by

$$Y = \max_{\forall l} |x[l]w[l-\tau]| \ , \tag{4.1}$$

where $x[l]$ is the sampled signal and $w[l-\tau]$ is a unit amplitude rectangular window of the same duration as the transmitted pulse. The offset τ is the sample index of the detected leading edge of the signal. In practice, to reduce the variance of the DPSS and improve SNR, multiple pulses are accumulated and averaged to obtain a single measurement, which we will still denote simply as Y. This is the measure of signal strength used throughout this work. Note that while the RTI literature generally uses power as the signal strength metric, Y is a measure of amplitude, being an average of many pulse peaks as measured by the analog to digital converter (ADC) in Figure 4.1. Rather than square this value to obtain units of power, we will simply express Y in the decibel scale in the next section.

4.2.3 *Log-distance Path Loss Model*

The UWB multipath propagation channel has been studied in theory and empirically, e.g. [73, 74]. In this work, we express the DPSS as a function of distance and shadowing using a simplified log-distance path loss model. The model is expressed with additive terms in

the log domain as

$$y = b + s - \alpha d + \epsilon \,, \tag{4.2}$$

where DPSS value $y = 20 \log_{10} Y$ is now measured in decibels. $b \in \mathbb{R}$ is a bias or "gain" term aggregating the effects of transmitter power, receiver sensitivity, antenna gains, cable losses, etc. $s \in (-\infty, 0]$ is the shadowing component of primary interest in this work; s models the signal strength loss in the observed variable y due to objects blocking the LOS. $\alpha > 0$ is a path loss exponent controlling the rate of signal decay due to distance, with d equal to the log-distance between transmitter and receiver. The additive error term $\epsilon \in \mathbb{R}$ represents measurement error and any other unmodeled effects.

To characterize b and α in (4.2) for a single transmitter/receiver pair, we have performed a LOS path loss experiment in a multipath rich laboratory environment over the distances of interest. The results are plotted in Figure 4.2. The results show a strong fit to the measured data, indicating that (4.2) is a reasonable model for DPSS path loss in indoor environments. The large decibel values shown in Figure 4.2 are relative to 1 amplitude unit, since proportionality constants for units of energy/voltage are not known. For example, the P410 ADC outputs DPSS values in the typical range of 5000 to 60000 amplitude units.

In order to produce a tomographic image of the shadowing caused by objects in the environment, many DPSS measurements must be taken at spatially diverse locations in that environment. This is facilitated by mobile sensor networks which may contain many links; M mobile nodes grants up to $N = M^2 - M$ unique transmit/receive pairs. We index (4.2) to encompass the full network by using i to index the unique links, and j to index the individual measurements made by a given link:

$$y_{ij} = b_i + s_{ij} - \alpha d_{ij} + \epsilon_{ij} \,. \tag{4.3}$$

Thus, y_{ij} is the jth DPSS measurement made by the ith link in the network. The index set is defined by $i \in \{1...N\}$, where $N = M^2 - M$. The links are formed by the M nodes

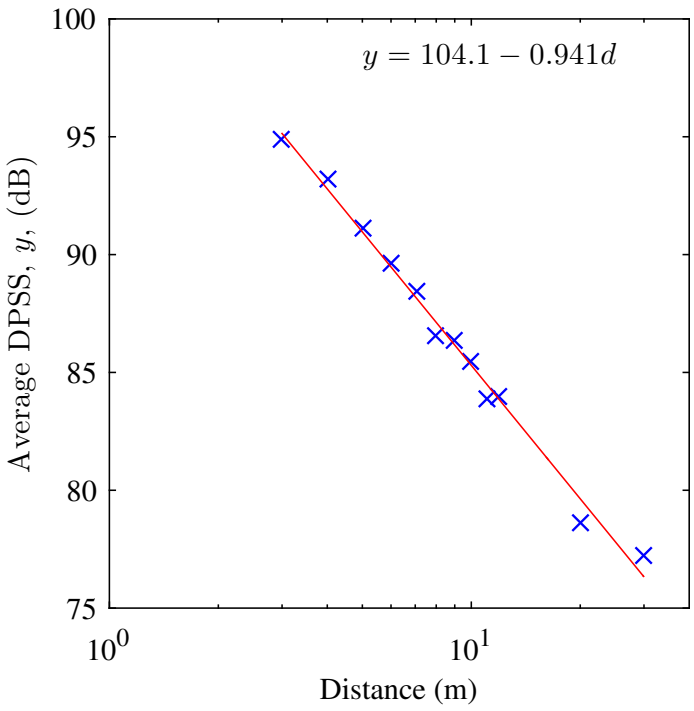

Figure 4.2: Measured DPSS for a single LOS $(s = 0)$ link in an indoor environment. The least squares values for the path loss parameters are $\hat{b} = 104.1$, $\hat{\alpha} = 0.941$, with $r^2 = 0.99$. 1000 DPSS measurements were averaged for each data point.

in the network, and each link makes n_i measurements. The gain term is now also indexed by i, since transmit power, receiver sensitivity, and other systematic effects mentioned above are different for each transmit/receive pair, and may vary substantially. The LOS shadowing s_{ij} and link log-distance d_{ij} may change with each measurement as the nodes move, and are indexed accordingly. The unknown path loss exponent α is assumed to be an environmental variable shared by all links and thus carries no index. Note that for a spherical wave propagating in free space $\alpha = 1$ for signal strength measurements, though in practice will vary due to antenna properties and the environment.

Clearly, the link index i creates a large number of bias parameters $\{b_i, \alpha\}$. Thus, single-link characterizations such as those shown in Figure 4.2 may not generalize well across the entire network, leading to poor or misleading results, even with homogeneous hardware. Our mixed effects estimation procedure, derived in the following sections, seeks to characterize these parameters, along with the unknown spatial shadowing.

4.3 Tomographic Projection Model

From the path loss model in (4.3), the DPSS measurements y_{ij} contain information about the shadowing loss along the LOS for that measurement. This information, when aggregated, should describe the static shadowing losses in the environment as a function of space. This rate of attenuation with respect to spatial extent has been termed the spatial loss field (SLF) [75, 55], and its estimation is our primary goal. Allowing the spatial variable $\mathbf{z}$ to represent position, the total shadowing loss s_{ij} between two points is described as the line integral of the continuous SLF $\theta(\mathbf{z})$ over the straight line connecting the two points,

$$s_{ij}(\theta(\mathbf{z}), L_{ij}) = \int_{L_{ij}} \theta\left(\mathbf{z}\right) d\mathbf{z}\,, \tag{4.4}$$

where L_{ij} is the straight line path connecting the transmitter and receiver of link i when taking measurement j. From (4.4) it can be seen that the SLF has units of dB/m if measuring distance in meters. Also, given the sign conventions used in Section 4.2.3, $\theta(\mathbf{z}) \in (-\infty,\, 0\,]$ will be negative in regions containing attenuating objects, and zero in free space regions.

In seeking a tractable method of estimating the entire SLF from measurements, we approximate the integral with a summation, and replace the continuous SLF $\theta(\mathbf{z})$ with a vector $\boldsymbol{\theta}$ having a discrete set of K pixel values. This yields

$$s_{ij} = \sum_{k=1}^{K} x_{ijk}\theta_k = \mathbf{x}_{ij}^T\boldsymbol{\theta}\,. \tag{4.5}$$

Now, the shadowing loss is the sum over all SLF pixels θ_k in the area to be imaged, multiplied by a corresponding set of pixel weights x_{ijk}. These weights represent each pixel's contribution to the total shadowing loss. Note that though the SLF is interpreted as a two-dimensional map, in (4.5) the SLF is expressed as a $K \times 1$ vector by column stacking, consistent with the image processing literature.

In assigning weights x_{ijk}, we choose the straight line approach, depicted in Figure 4.3.

In this weighting only pixels along the direct LOS between transmitter and receiver receive nonzero weight. This is due to the fact that the DPSS measurement effectively eliminates the multipath signal components, such that only objects within pixels along the LOS should materially affect the shadowing loss. The notation $\theta_k \in L_{ij}$ will indicate that the straight line segment from transmitter to receiver passes through pixel θ_k. The weighting values are then assigned by

$$x_{ijk} = \begin{cases} D_k & : \theta_k \in L_{ij} \\ 0 & : \text{else} \end{cases}, \tag{4.6}$$

where D_k is the length of the line segment passing through pixel θ_k. This weighting scheme is similar to those used in X-ray based computed tomography (CT) scanning, as also noted in [71]. Weighting each pixel by line segment length also preserves the expected units of measurement for the model; x_{ijk} has units of meters, θ_k has units of dB/m, yielding the shadowing loss in pure decibels of attenuation.

The aforementioned straight line weight model makes physical sense for the DPSS metric, since the LOS path is isolated. However different propagation models have also been considered in the RTI literature. In [53, 10], an evenly weighted ellipse with transmitter and receiver as foci was used. The weight factor was inversely proportional to the square root of the link distance, which represents the lower RSS variance for longer links. In [71], several models were studied from experimental data, including both elliptical and straight line weighting areas.

We also expect that shadowing losses will be spatially correlated in practice. Therefore we will define the between-pixel spatial covariance matrix

$$E\left[\boldsymbol{\theta}\boldsymbol{\theta}^T\right] - E[\boldsymbol{\theta}]\, E[\boldsymbol{\theta}]^T = \mathbf{C}_{\boldsymbol{\theta}} \in \mathbb{R}^{K \times K}. \tag{4.7}$$

To determine the elements of $\mathbf{C}_{\boldsymbol{\theta}}$, we assume that the between-pixel covariance decays

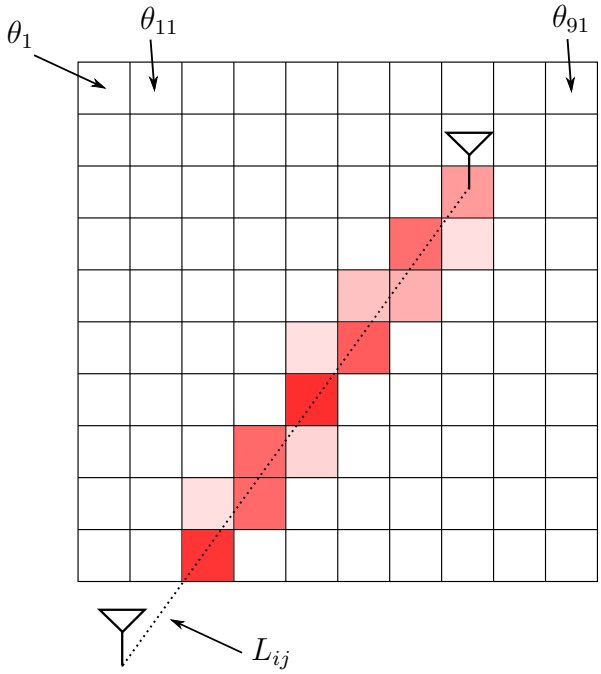

Figure 4.3: Graphical depiction of relative pixel weighting and indexing for an arbitrary link i taking a measurement j in a 10×10 pixel image. Shaded pixels have $x_{ijk} > 0$ according to (4.6); unshaded pixels have $x_{ijk} = 0$. Note the single index k is used to designate the K pixels by column stacking, typical in image processing contexts.

exponentially with distance,

$$E\left[\theta_k \theta_l\right] - E\left[\theta_k\right] E\left[\theta_l\right] = \sigma_\theta^2 e^{-\frac{D_{kl}}{\kappa}}, \tag{4.8}$$

where D_{kl} is the distance between the centers of pixels θ_k and θ_l, and κ is a spread parameter with units of meters. This exponential decay parametrization is similar to that used in the network shadowing model of [55] to model randomly placed objects, and was used in the experimental work of [71] as *a-priori* image information. We use the empirically determined value of $\kappa = 0.21$ m from [55] in our work. We also set the prior pixel variance $\sigma_\theta^2 = 1$, as the overall scaling effect will be managed by selection of regularization parameter λ_2 in Section 4.4.2.

Note that other characterizations of pixel correlation besides that in (4.8) are possible. In our work in [3] for example, we explored using *a-priori* knowledge of image structure

expressed as covariance to enhance image reconstruction. However, we have not done so in this work in order to minimize assumptions.

4.4 Mixed Effects Image Reconstruction

This section describes our full forward model mapping the unknown SLF onto the known DPSS measurements. The inverse problem of retrieving an estimate of the SLF image is ill-conditioned, and thus requires regularization to obtain a useful result. We explain our approach to regularization using a modified form of the EN cost function, and its solution using convex optimization.

4.4.1 Forward Model

By combining (4.3) and (4.5), we obtain an expression for the K unknown SLF parameters as a function of the observed DPSS measurements:

$$y_{ij} = \mathbf{x}_{ij}^T \boldsymbol{\theta} + b_i - \alpha d_{ij} + \epsilon_{ij} \,. \tag{4.9}$$

As given in Section 4.2, each link in the network makes n_i measurements. To simplify the notation we will assume that each link makes the same number of measurements, so that

$n_i = n$.[3] Aggregating the n measurements made by link i yields the expression

$$\begin{aligned}
\mathbf{y}_i &= \begin{bmatrix} \mathbf{x}_{i1}^T \\ \vdots \\ \mathbf{x}_{in}^T \end{bmatrix} \boldsymbol{\theta} + b_i \begin{bmatrix} 1 \\ \vdots \\ 1 \end{bmatrix} + \alpha \begin{bmatrix} -d_{i1} \\ \vdots \\ -d_{in} \end{bmatrix} + \begin{bmatrix} \epsilon_{i1} \\ \vdots \\ \epsilon_{in} \end{bmatrix} \\
&= \mathbf{X}_i \boldsymbol{\theta} + b_i \mathbf{1}_n + \alpha \mathbf{d}_i + \boldsymbol{\epsilon}_i \\
&= \begin{bmatrix} -\mathbf{d}_i & \mathbf{X}_i \end{bmatrix} \begin{bmatrix} \alpha \\ \boldsymbol{\theta} \end{bmatrix} + b_i \mathbf{1}_n + \boldsymbol{\epsilon}_i \\
&= \mathbf{H}_i \boldsymbol{\theta}^{(\alpha)} + b_i \mathbf{1}_n + \boldsymbol{\epsilon}_i \,. \qquad (4.10)
\end{aligned}$$

Here we have defined the design matrix $\mathbf{X}_i \in \mathbb{R}^{n \times K}$ as the stacked, transposed pixel weight vectors defined for each individual measurement in (4.5). Defining $\mathbf{1}_n$ to be an $n \times 1$ vector of ones, the vector $b_i \mathbf{1}_n$ replicates the nuisance parameter representing the bias of link i for each measurement. The vector $\alpha \mathbf{d}_i \in \mathbb{R}^n$ maps the contribution of the unknown path loss exponent onto the DPSS measurements via the known log distances. Finally, the collected errors form the vector $\boldsymbol{\epsilon}_i \in \mathbb{R}^n$. For compactness, we combine the unknowns not dependent on link index i into a single vector $\boldsymbol{\theta}^{(\alpha)} \in \mathbb{R}^{K+1}$ with corresponding known model matrix $\mathbf{H}_i \in \mathbb{R}^{n \times (K+1)}$.

From (4.10), we can see that the measurements for each link $\mathbf{y}_i$ are a function of the common SLF / path loss exponent parameter $\boldsymbol{\theta}^{(\alpha)}$, which is of primary interest and does not vary with each link i. However, DPSS is also a linear function of the link biases $\{b_i\}$, which are unique to each link and unknown. From here on we will model b_i as a Gaussian random variable with unknown mean and variance; so that $b_i \sim \mathcal{N}(\mu_b, \sigma_b^2)$. The $\boldsymbol{\epsilon}_i$ is modeled as a zero-mean independent Gaussian random vector; $\boldsymbol{\epsilon}_i \sim \mathcal{N}(\mathbf{0}, \sigma_\epsilon^2 \mathbf{I}_n)$. Thus within link i, we explicitly separate the link bias b_i from independent noise vector $\boldsymbol{\epsilon}_i$. We also assume that the $\{b_i, \boldsymbol{\epsilon}_i\}$ are mutually independent, and independent across i.

[3] It is straightforward to generalize these results such that each link makes a variable number of measurements.

Under these assumptions, (4.10) has the general form of a linear *mixed effects model*, a special class of linear models used in the statistical literature. Such models are used to express the hierarchical effects of clustered data which might be arranged into "bins". That is, they account for measurement effects at different levels: global effects which are of primary interest, and subject or group specific effects which are not of primary interest but nevertheless must be accounted for [76, 77]. Thus, they are a natural fit for modeling the unknown bias and path loss present in a network making signal strength measurements. The term *mixed effects* is used because we model the global parameters $\boldsymbol{\theta}^{(\alpha)}$ as fixed but unknown "fixed effects", while the link specific effects $\{b_i, \boldsymbol{\epsilon}_i\}$ are modeled as random variables, or "random effects". While we will not specifically use the Gaussian assumption of the $\{b_i\}$ for image reconstruction, doing so facilitates closed form derivation of the Cramér Rao lower bound (CRLB), and is in general agreement with our empirical results.

To obtain a single linear model from the N sets of equations, (4.10) is stacked for each value of i by

$$\begin{aligned}\mathbf{y} = \begin{bmatrix} \mathbf{y}_1 \\ \vdots \\ \mathbf{y}_N \end{bmatrix} &= \begin{bmatrix} \mathbf{H}_1 \\ \vdots \\ \mathbf{H}_N \end{bmatrix} \boldsymbol{\theta}^{(\alpha)} + \begin{bmatrix} \mathbf{1}_n & \mathbf{0} & \cdots & \mathbf{0} \\ \mathbf{0} & \mathbf{1}_n & & \vdots \\ \vdots & & \ddots & \mathbf{0} \\ \mathbf{0} & \cdots & \mathbf{0} & \mathbf{1}_n \end{bmatrix} \begin{bmatrix} b_1 \\ \vdots \\ b_N \end{bmatrix} + \begin{bmatrix} \boldsymbol{\epsilon}_1 \\ \vdots \\ \boldsymbol{\epsilon}_N \end{bmatrix} \\ &= \mathbf{H}\boldsymbol{\theta}^{(\alpha)} + \mathbf{Z}\mathbf{b} + \boldsymbol{\epsilon}\,. \end{aligned} \tag{4.11}$$

Here the full data vector is $\mathbf{y} \in \mathbb{R}^{N_T}$, where $N_T = Nn$ is the full data size. The full model matrices have dimensions $\mathbf{H} \in \mathbb{R}^{N_T \times (K+1)}$ and $\mathbf{Z} \in \mathbb{R}^{N_T \times N}$. The unknown SLF vector $\boldsymbol{\theta}^{(\alpha)} \in \mathbb{R}^{(K+1)}$ is unchanged, and $\mathbf{b} \in \mathbb{R}^N$ is the full unknown mixed effects vector. The modeling errors / measurement noise is captured by vector $\boldsymbol{\epsilon} \in \mathbb{R}^{N_T}$. Thus (4.11) relates all parameters, known and unknown, to the collected data $\mathbf{y}$ across all links in the network, and serves as our full forward measurement model.

4.4.2 EN Regularization

Inverse problems in the literature on mixed effects are generally solved using a maximum likelihood approach in which the data covariance and unknown fixed effects are estimated simultaneously [76]. However, (4.11), like most imaging inverse problems, represents an underdetermined system of equations. That is, the measurement data are insufficient to fully describe the parameter $\boldsymbol{\theta}^{(\alpha)}$, yielding an infinite number of candidate solutions which fit the data $\mathbf{y}$. Model matrix $\mathbf{H}$ has low rank, which is due to a combination of limited measurements, each measurement describing only a small part of $\boldsymbol{\theta}^{(\alpha)}$, and disparities in areas of the image crossed by few or no links. A full rank model matrix $\mathbf{H}$ is normally assumed in the mixed effects literature; thus the usual parametric solution of mixed models, e.g., maximum likelihood, will not yield useful images.

As a result, prior information must be introduced into the model to select a unique solution among the infinite number available, a process known as regularization. This usually involves minimizing some cost function of the data and unknown parameters, selecting the "best" value for $\boldsymbol{\theta}^{(\alpha)}$ which minimizes the cost function. Regularization is thus a non-parametric approach to solving (4.11). Several popular methods exist, such as Tikhonov (2-norm), lasso (1-norm), truncated singular value decomposition, and total variation approaches [78]. Each method has its own tradeoffs; in [10], Tikhonov regularization was preferred for computational speed and having a closed form solution. In [57, 59, 58], total variation minimization was preferred to enforce piecewise constant shadowing regions.

In our approach, we use the EN. Originally proposed in [79], the EN loss function is a linear combination of Tikhonov and lasso type penalties, given by

$$L\left(\lambda_1, \lambda_2, \boldsymbol{\theta}\right) = \left\|\mathbf{y} - \mathbf{X}\boldsymbol{\theta}\right\|_2^2 + \lambda_2 \left\|\boldsymbol{\Gamma}\boldsymbol{\theta}\right\|_2^2 + \lambda_1 \left\|\boldsymbol{\theta}\right\|_1 \tag{4.12}$$

for the basic linear model $\mathbf{y} = \mathbf{X}\boldsymbol{\theta} + \boldsymbol{\epsilon}$. The 2-norm penalty $\left\|\boldsymbol{\Gamma}\boldsymbol{\theta}\right\|_2^2$ is taken from Tikhonov regularization, also known as ridge regression, and penalizes the energy in $\boldsymbol{\Gamma}\boldsymbol{\theta}$, for some

specified linear operator $\mathbf{\Gamma}$. The 1-norm penalty $\|\boldsymbol{\theta}\|_1$ comes from the lasso regression, and enforces a sparse solution. Parameters $\{\lambda_2, \lambda_1\} > 0$ control the penalty term's smoothing effect on the solution.

Several unique properties of the EN are noted in [79] which are appropriate for the assumptions in our problem. First, the 1-norm penalty enforces a sparse solution, with many elements of $\boldsymbol{\theta}$ forced to zero. This is appropriate as we assume that much of the area to be imaged consists of empty space, which has shadowing loss equal to zero. 2-norm-only regularization methods will in general have all $\theta_k \neq 0$. Second, the addition of the 2-norm penalty from Tikhonov regularization overcomes what is known as a grouping effect of the lasso. If a subset of parameters $\boldsymbol{\theta}_c \subset \boldsymbol{\theta}$ are highly correlated, then the lasso will tend to select only one of them at random. This grouping effect is undesirable for our model; in Section 4.3 we assume shadowing losses to be correlated among neighboring pixels in the image.

To model this expected behavior, we define the *a-priori* pixel covariance according to (4.7) and (4.8). Use of a prior covariance matrix is of course probabilistic and suggests a Bayesian interpretation of the data. However, (4.12) is a deterministic cost function of the unknowns. It has been observed, e.g., [80], that the 2-norm Tikhonov penalty can be related to the Bayesian covariance via

$$\|\mathbf{\Gamma}\boldsymbol{\theta}\|_2^2 = \boldsymbol{\theta}^T\mathbf{\Gamma}^T\mathbf{\Gamma}\boldsymbol{\theta} = \boldsymbol{\theta}^T\mathbf{C}_{\boldsymbol{\theta}}^{-1}\boldsymbol{\theta}\,, \tag{4.13}$$

so that $\mathbf{\Gamma}$ can be derived from $\mathbf{C}_{\boldsymbol{\theta}}^{-1}$ via the Cholesky decomposition. In this way the assumed pixel covariance may be incorporated into the 2-norm regularization term in (4.12).

Finally, we extend the EN cost function of (4.12) by incorporating our additional mixed effects model terms:

$$\widetilde{L}\left(\lambda_1, \lambda_2, \boldsymbol{\theta}, \alpha, \mathbf{b}\right) = \left\|\mathbf{y} - \mathbf{H}\boldsymbol{\theta}^{(\alpha)} - \mathbf{Z}\mathbf{b}\right\|_2^2 + \lambda_2\left\|\mathbf{\Gamma}\boldsymbol{\theta}\right\|_2^2 + \lambda_1\left\|\boldsymbol{\theta}\right\|_1\,. \tag{4.14}$$

Here the squared-error term seeks to obtain agreement between the solution and the data, where we now allow the individual link bias terms $\mathbf{b}$ to be model variables to be estimated. The linear operator $\mathbf{\Gamma}$ allows us to enforce the per-pixel spatial correlations desired above. Note that the penalty terms apply to vector $\boldsymbol{\theta}$ only, that is, regularization is not applied to variable α. Given the regularization parameters, the minimization problem with all constraints is

$$\left\{\hat{\boldsymbol{\theta}}, \hat{\alpha}, \hat{\mathbf{b}}\right\} = \underset{\boldsymbol{\theta}\leq 0\,,\alpha>0}{\arg\min}\, \widetilde{L}\left(\boldsymbol{\theta}, \alpha, \mathbf{b} \mid \lambda_1, \lambda_2\right) . \tag{4.15}$$

The constraint $\boldsymbol{\theta} \leq 0$ indicates that all elements of the solution vector are less than or equal to zero, consistent with the definition. While there is no known closed-form solution to the EN, both it and our extension in (4.14) represent convex cost functions. Thus, efficient methods exist for finding numerical solutions, and flexible software packages are available. For our simulation and experimental results, we have employed the CVX package for MATLAB, which allows specifying and solving various convex problems [81].

This leaves the problem of determining the parameters $\{\lambda_2, \lambda_1\}$ which adjust the regularization weighting to apply. Higher values will generally result in smoother images, with fewer pixels selected as nonzero. While multiple methods exist to determine regularization parameters, we use the two step method suggested in [79]. In the first step, the usual Tikhonov regularization is performed, that is, with $\lambda_1 = 0$ for a range of values of λ_2. For each λ_2, we plot the observed "norm error" $\|\mathbf{\Gamma}\hat{\boldsymbol{\theta}}(\lambda_2)\|_2^2$ as a function of the corresponding "data error" $\|\mathbf{y} - \mathbf{H}\hat{\boldsymbol{\theta}}^{(\alpha)}(\lambda_2) - \mathbf{Z}\hat{\mathbf{b}}\,(\lambda_2)\|_2^2$. For a wide range of λ_2 values, this curve will take an "L" shape, and hence this procedure is referred to as the L-curve method. The λ_2 value corresponding to the inflection point at which the sum of the two error terms is minimized is the value used. This heuristic is justified by its general robustness and intuition as a compromise between the two solution norms.

For λ_1, leave-one-out cross validation is used. A single data point is omitted from each link's measurements, forming a "training" data set and associated model matrices $\{\mathbf{y}_t, \mathbf{H}_t, \mathbf{Z}_t\}$. The left out data forms a smaller "verification" data and model matrix set,

$\{\mathbf{y}_v, \mathbf{H}_v, \mathbf{Z}_v\}$. A suitable range of values for λ_1 are chosen to test, denoted $\{\lambda_{1,q}\},\ q = 1...Q$. Then a solution pair $\hat{\boldsymbol{\theta}}_q^{(\alpha)}, \hat{\mathbf{b}}_q$ is computed for each $\lambda_{1,q}$ using the training set. For each candidate solution, we calculate the prediction error $\|\mathbf{y}_v - \mathbf{H}_v\hat{\boldsymbol{\theta}}_q^{(\alpha)} - \mathbf{Z}_v\hat{\mathbf{b}}_q\|_2^2$ using the verification set. Finally, we choose the $\lambda_{1,q}$ corresponding to the $\hat{\boldsymbol{\theta}}_q, \hat{\mathbf{b}}_q$ that gave the lowest prediction error. With both $\{\lambda_1, \lambda_2\}$ now selected, a full solution can be computed using the entire data set via (4.15).

4.5 Bayesian CRLB Derivation

It is very useful to obtain performance bounds for a given model and solution method to benchmark performance in the general case. The CRLB is very well known in statistics as a lower bound on the variance of unbiased estimators. The CRLB proves that the variance of individual parameter estimates are lower bounded by corresponding elements of the inverse Fisher information matrix. However, our estimator in (4.15) is clearly biased by the introduction of the regularization terms. In such cases the CRLB has been extended to include biased estimators in what is known as the Bayesian CRLB, or Van Trees inequality [82]. The covariance of biased estimators is bounded by the inclusion of a prior distribution on the unknowns, just as in Bayesian estimation. This leads to the derivation of a Fisher information matrix for both the data likelihood and the prior. The Bayesian CRLB states that the estimation error covariance matrix $\mathbf{E} = E[(\hat{\boldsymbol{\theta}}^{(\alpha)} - \boldsymbol{\theta}^{(\alpha)})(\hat{\boldsymbol{\theta}}^{(\alpha)} - \boldsymbol{\theta}^{(\alpha)})^T]$ is lower bounded by

$$\mathbf{E} \succcurlyeq (\mathbf{F}_L + \mathbf{F}_P)^{-1} = \mathbf{F}^{-1}\,, \tag{4.16}$$

where $\mathbf{F}_L$, $\mathbf{F}_P$ are the Fisher information matrices for the data log likelihood and prior distributions, respectively. The "$\succcurlyeq$" relation indicates that the difference matrix $\mathbf{E} - \mathbf{F}^{-1}$ is positive semidefinite. An important consequence of this fact is that the diagonal elements of $\mathbf{E}$ represent lower bounds on the variance of estimating individual pixel values; that is,

$$\mathbf{E}_{qq} = E[(\hat{\boldsymbol{\theta}}^{(\alpha)} - \boldsymbol{\theta}^{(\alpha)})_q^2] \succcurlyeq \mathbf{F}_{qq}^{-1}\,. \tag{4.17}$$

Though other formulae exist, the Fisher information expressions for general data log likelihood and prior distributions can be expressed as

$$\mathbf{F}_L = E_{\mathbf{y}|\boldsymbol{\theta}}\left[\left(\nabla_{\boldsymbol{\theta}}\mathscr{L}\left(\mathbf{y}|\boldsymbol{\theta}\right)\right)\left(\nabla_{\boldsymbol{\theta}}\mathscr{L}\left(\mathbf{y}|\boldsymbol{\theta}\right)\right)^T\right] \tag{4.18}$$

$$\mathbf{F}_P = E_{\boldsymbol{\theta}}\left[\left(\nabla_{\boldsymbol{\theta}}\mathscr{L}\left(\boldsymbol{\theta}\right)\right)\left(\nabla_{\boldsymbol{\theta}}\mathscr{L}\left(\boldsymbol{\theta}\right)\right)^T\right], \tag{4.19}$$

where $\mathscr{L}(\cdot)$ indicates the log-likelihood of the enclosed random vector. ∇ represents the gradient operator taken with respect to the unknown parameter as shown. We will now derive the necessary expressions to compute a Bayesian CRLB for our mixed effects model in (4.10), and use it to benchmark simulated performance. From (4.10), the data have Gaussian distribution $\mathbf{y}_i \sim \mathcal{N}(\boldsymbol{\mu}_{\mathbf{y}_i}, \mathbf{C}_{\mathbf{y}_i})$, where

$$\boldsymbol{\mu}_{\mathbf{y}_i} = \mathbf{H}_i\boldsymbol{\theta}^{(\alpha)} + \mu_b\mathbf{1}_n \tag{4.20}$$

$$\mathbf{C}_{\mathbf{y}_i} = \sigma_b^2\mathbf{1}_n\mathbf{1}_n^T + \sigma_\epsilon^2\mathbf{I}_n\,. \tag{4.21}$$

The data log likelihood is then given by (up to constant terms not dependent on $\boldsymbol{\theta}^{(\alpha)}$):

$$\mathscr{L}\left(\mathbf{y}_i|\boldsymbol{\theta}^{(\alpha)}\right) = -\frac{1}{2}\left(\mathbf{y}_i - \boldsymbol{\mu}_{\mathbf{y}_i}\right)^T\mathbf{C}_{\mathbf{y}_i}^{-1}\left(\mathbf{y}_i - \boldsymbol{\mu}_{\mathbf{y}_i}\right). \tag{4.22}$$

Using straightforward rules for the gradient operator over vectors, it can be easily shown that

$$\nabla_{\boldsymbol{\theta}^{(\alpha)}}\mathscr{L}\left(\mathbf{y}_i|\boldsymbol{\theta}^{(\alpha)}\right) = \mathbf{H}_i^T\mathbf{C}_{\mathbf{y}_i}^{-1}\left(\mathbf{y}_i - \boldsymbol{\mu}_{\mathbf{y}_i}\right) = \mathbf{K}_i\,, \tag{4.23}$$

which when inserted into the definition of Fisher information gives

$$\mathbf{F}_{L_i} = E_{\mathbf{y}_i|\boldsymbol{\theta}^{(\alpha)}}\left[\mathbf{K}_i\mathbf{K}_i^T\right] = \mathbf{H}_i^T\mathbf{C}_{\mathbf{y}_i}^{-1}\mathbf{H}_i \tag{4.24}$$

as the Fisher information for a single link in the network. Since we have assumed that the random variables $\{b_i,\, \boldsymbol{\epsilon}_i\}$ are independent across links, the data $\{\mathbf{y}_i\}$ represent indepen-

dent observations of $\boldsymbol{\theta}^{(\alpha)}$. The additivity property of Fisher information for independent observations gives

$$\begin{aligned}\mathbf{F}_L &= \sum_{i=1}^{N} \mathbf{F}_{L_i} = \sum_{i=1}^{N} \mathbf{H}_i^T \mathbf{C}_{\mathbf{y}_i}^{-1} \mathbf{H}_i \\ &= \sum_{i=1}^{N} \mathbf{H}_i^T \left(\sigma_b^2 \mathbf{1}_n \mathbf{1}_n^T + \sigma_\epsilon^2 \mathbf{I}_n\right)^{-1} \mathbf{H}_i \end{aligned} \tag{4.25}$$

as the expression for the Fisher information matrix of data collected from our uncalibrated network across all links. If the network were "perfectly calibrated" such that all bias parameters were known and removed, (4.25) reduces to

$$\mathbf{F}_{L_C} = \frac{1}{\sigma_\epsilon^2} \mathbf{X}^T \mathbf{X} \,, \tag{4.26}$$

where $\mathbf{X}$ indicates the stacked matrices $\mathbf{X}_i$, and the subscript C indicates a calibrated or bias free network. This is the same matrix derived in [10] for their imaging problem, in which the stationary system took baseline readings in empty space before adding the objects under test.

For the prior distribution on the image and path loss parameters, we will assume that $\boldsymbol{\theta}^{(\alpha)}$ is also Gaussian distributed with mean $\boldsymbol{\mu}_{\boldsymbol{\theta}^{(\alpha)}}$ and covariance $\mathbf{C}_{\boldsymbol{\theta}^{(\alpha)}}$. The covariance structure is defined by (4.8), with α assumed uncorrelated with the image pixels. By very similar derivation it can be shown that

$$\mathbf{F}_P = \mathbf{C}_{\boldsymbol{\theta}^{(\alpha)}}^{-1} \,, \tag{4.27}$$

which defines all necessary parameters to compute the bound in (4.17). Note that while (4.17) gives a variance bound for *each* pixel, we will generally average over all pixels to compute an average bound for the entire image.

4.6 Performance Simulations

In this section we analyze the performance of our proposed convex EN solution approach with respect to the theoretical bounds derived in Section 4.5. We attempt to choose parameter values which are realistic and also representative of the conditions seen in our experimental results of Section 4.7. In our simulations, we assume a 32×32 pixel image representing a 4.8 m $\times$ 4.8 m area. The network of UWB nodes is mobile and each node moves independently through a larger 16×16 m area encompassing the image in a random-trajectory fashion. Our network is assumed to have a bias standard deviation $\sigma_b = 3$ dB and measurement noise standard deviation $\sigma_\epsilon = 3$ dB. Test images are generated according to a Gaussian distribution with a mean SLF value of 3 dB/m and pixel covariance defined by (4.8). We choose this prior image distribution for a fair comparison with standard Tikhonov regularization, which would be optimal for the Gaussian case *if* the network were perfectly calibrated. The simulated path loss exponent α is also Gaussian with mean 1 and standard deviation 0.1.

We measure the root mean squared error (RMSE) performance of both our proposed solution in (4.15), and our proposed solution ignoring the random effects and path loss, $\{b_i, \alpha\}$, and instead using only their mean values. These are assumed to be known from a measurement experiment such as that given in Figure 4.2. For comparison, we also simulate the performance of the standard Tikhonov regularization used in e.g. [10], also ignoring random effects. The Bayesian CRLBs are also computed, where we use both our mixed effects Fisher information from (4.25) and the "calibrated" Fisher information in (4.26) as separate cases. Results are displayed in Figure 4.4. In the first simulation we examine the average RMSE as a function of node count, assuming each node takes $n = 30$ measurements as it moves through the area. The results are shown in the top plot of Figure 4.4. We note the superior performance of our method when random effects are considered and estimated across all values of M with respect to the Bayesian CRLBs. In

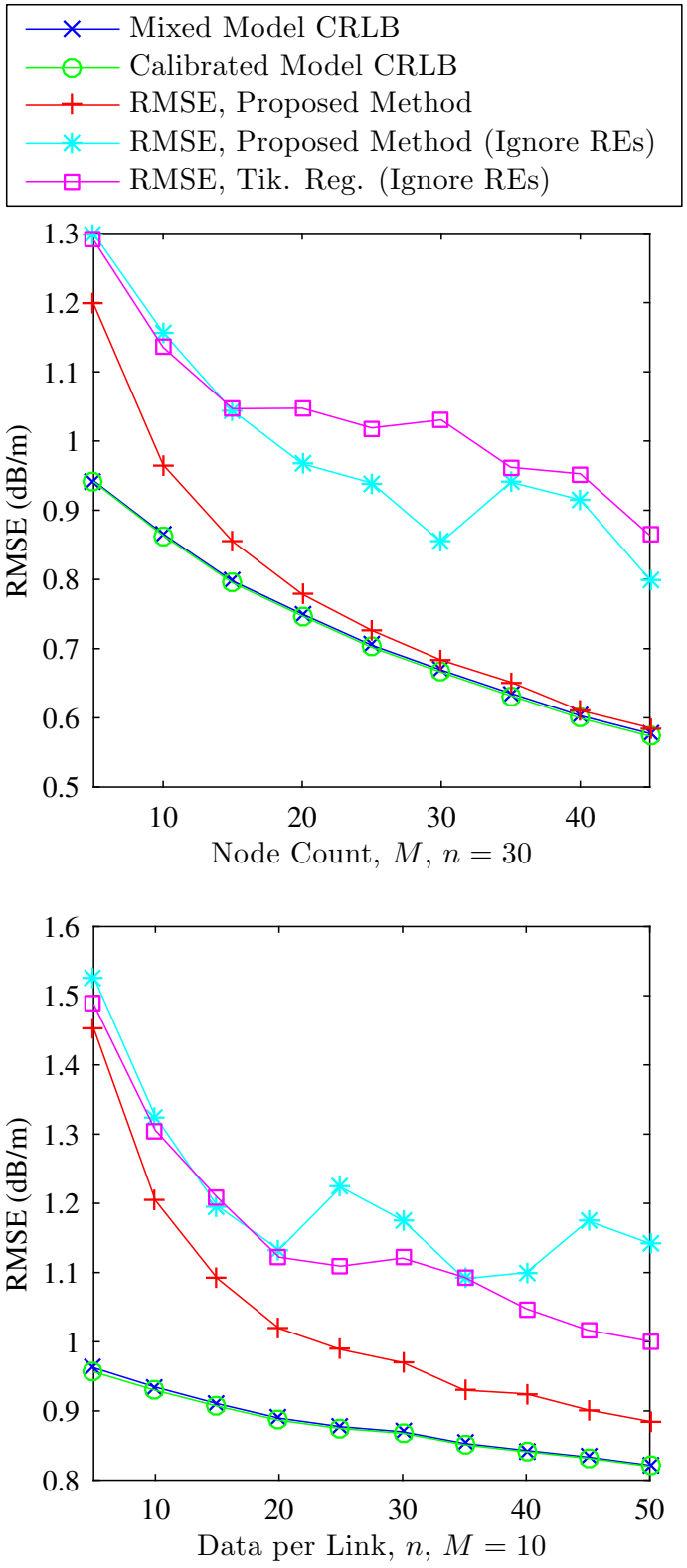

Figure 4.4: Comprehensive performance simulation results, varying node count M (top) and data per link n (bottom). 25 images were simulated and estimated per data point.

fact our method virtually achieves the lower bound for large M. Also of interest is that the mixed model lower bound is only trivially larger than the calibrated model lower bound. These results suggest that the influence of the random effects and path loss $\{b_i, \alpha\}$ can be mitigated, since the bound is taken with respect to estimating fixed unknown parameter $\boldsymbol{\theta}^{(\alpha)}$. The difference between the two bounds would increase, however, if the bias variance σ_b^2 increased with respect to the noise variance σ_ϵ^2.

For our second simulation we assume a network of $M = 10$ nodes and instead vary the data collected for each link i. The results are shown in the bottom plot of Figure 4.4. We again observe improving performance as more data becomes available to each link in the network. The lower bound on performance does not decrease as rapidly, though the total data size N_T is growing only linearly with n in this case. In both simulations, we see a clear performance degradation when the random effects are ignored. In fact, since Tikhonov Regularization can be shown to be a minimum mean-squared error (MMSE) estimator for Gaussian distributed data with Gaussian prior, other methods of reconstruction are not likely to improve upon the indicated results without considering the random effects.

4.7 Experimental Results

In this section we validate our forward model and image reconstruction techniques using real experimental data from a variety of test setups containing attenuating objects. The experiments were performed using our Cognitive Spectrum Operations Testbed (CSOT). A primary difficulty in RTI research has been collection of quality real data. These tomographic experiments have resulted in collection of high fidelity data sets to address this issue.

The installed hardware of interest in this work is the aforementioned P410 UWB radio from Time Domain. The radio transmits and samples UWB pulses as described in Section 4.2.1 for each pairwise link in the network. Note that each CSOT node has two duplex UWB antenna ports, and both are used. This results in a system with 224 useful

links from only 8 mobile nodes. The transmitted power and bandwidth are compliant with FCC regulations for a UWB system for general use. Received signal scans are converted to DPSS measurements as in Section 4.2.2, and the esimated SLF is computed via the methods of Section 4.4. Common and individual experimental parameters are summarized in Table 4.1.

To establish the correct pixel weighting described in Section 4.3, accurate position information must be available to the nodes at each time step. All position data for our experiments are also provided by the UWB radios by our cooperative localization algorithms described in Chapter 3 and [4, 5]. As shown in Chapter 3, the localization error is < 2 cm in LOS conditions. Thus, the same measured waveforms and hardware are used for both localization and tomographic mapping. We emphasize this natural SLAM characterization; a mobile network already utilizing UWB hardware for localization purposes could also perform our tomographic mapping in parallel. The UWB's low power and wide bandwidth make harmful interference very unlikely, enabling compatibility with other RF communications hardware.

We also note that it is difficult to accurately establish the true SLF in an experimental setting, and thus to compute the RMSE of the estimated images. Still, it is beneficial to quantify the estimated SLF image quality in some sense. We compute two different metrics for this purpose. First is the well known structural similarity (SSIM) metric [83], which compares a processed or degraded image to a reference. The SSIM attempts to measure how well structure is preserved, an important property of subjectively high quality images. Higher values of SSIM are better, with the maximum value of 1 occurring only when both images are identical. The reference images we use here are binary, equal to one where a pixel is occupied by an attenuating object, and zero elsewhere. To compare with the reference, the estimated SLF images are scaled to the range $[0, 1]$, ignoring the negative sign.

For the second metric, we use the same reference image and scaled SLF to compute a

Table 4.1: Tomographic mapping campaign summary.

	Exp. I	Exp. II	Exp. III
Number of discrete nodes	8		
Number of radio links, N	224		
Localization error RMSE	< 2.0 cm		
UWB pulse bandwidth	$3.3 - 5.5$ GHz		
UWB pulse duration	~ 4 ns		
UWB pulses per measurement	128		
Approx. avg. pulse power	-14.78 dBm		
Pixel size	0.1 m	0.15 m	0.15 m
Image dimensions	30×60	47×60	37×37
Data size, N_T	8512	10304	9856
Data per link, n	38	46	44
Reg. parameter λ_1	0.1350	0.1068	0.0936
Reg. parameter λ_2	1.000	0.9770	0.6000
Est. object(s) attenuation	8.1 dB	4.15, 7.64 dB	3.72 dB
Measured object(s) attenuation	14.5 dB	14.5, 14.5 dB	6.3 dB
Est. α	1.063	0.992	1.284
SSIM index	0.891	0.802	0.448
Pixel occupancy index	0.978	0.977	0.876

simple pixel occupancy index. This is intended to measure how spatially accurate the image reconstruction is at detecting the objects in the experiments. The scaled SLF is thresholded to create a binary estimate; pixels less than 0.25 are treated as zero, and pixels greater than 0.25 are set to one. The pixel occupancy index is then defined to be the percentage of total pixels where the reference image and binary SLF estimate are equal. Thus, the index falls in the range $[0, 1]$; higher values being better. Both the SSIM and pixel occupancy indices are provided in Table 4.1. The following subsections detail the particulars of the three experiments performed.

4.7.1 Experiment I: Hallway, Single Object

Our first experiment was performed in a laboratory building hallway, with the image encompassing an area approximately 3×6 m in size. The confined space, with large metal doors and close walls is intended to create a multipath rich environment for the system to overcome. A single 1.22 m wall section in the center is the target to be imaged; broad-

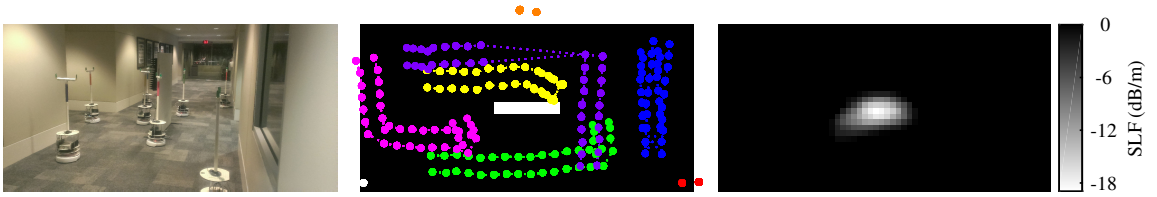

Figure 4.5: Experiment I setup and results. Left: Hallway test setup, showing the attenuating object and CSOT nodes. Middle: overhead schematic view / binary reference image of the test area. Data sampling locations for each node are indicated by colored dots. Right: SLF image reconstruction from DPSS measurements.

band RF absorbing foam was used to create opacity to the UWB signals. The test utilized 3 stationary and 5 mobile nodes. The experiment setup, binary reference image, and reconstructed images are displayed in Figure 4.5. We note that the position of the wall is well-contrasted with the free space background, which is correctly estimated to have an attenuation of 0 dB. As a result, the SSIM and pixel occupancy index given in Table 4.1 are the highest of the campaign.

To estimate the attenuation of the wall from the SLF image, we take a straight line, perpendicular path through the wall at its brightest point. Doing so gives an estimated total attenuation of 8.1 dB, an approximation of the laboratory measured attenuation of 14.5 dB. Note that in general, shadowing loss values obtained from the tomographic image will tend to underestimate the true value, since the regularization applied tends to bias the solution toward zero.

4.7.2 Experiment II: Large Room, Two Objects

Our second experiment seeks to differentiate and estimate the attenuation of two 1.22 m objects separated by a gap of 1.58 m. The experiment was performed in a large conference room with a larger test area of 7×9 m. The same type of attenuating foam was used for the walls, and the test again used 3 stationary and 5 mobile nodes. The results are shown in Figure 4.6. The objects are well differentiated, though we do note some over-smoothing with our systematic regularization parameter search. This lowers the SSIM vs. Experiment

I, though the occupancy index is still quite high. In this case, the wall sections have an estimated attenuation of 4.15 dB (left) and 7.64 dB (right) using the same perpendicular paths as Experiment I.

4.7.3 Experiment III: Through-wall Imaging

The final experiment seeks to demonstrate our proposed techniques for a through-wall image, an application of RTI which has been frequently proposed in the literature. That is, we wish to estimate not only the location and attenuation of visible features, but also those which might be obstructed behind walls. To do this, a 2.44×2.44 m artificial building was constructed from standard drywall material, shown in Figure 4.7. Since the drywall is highly transparent to the UWB signal, very thin RF absorbing foam was added to the inside surface to simulate a much thicker material. Another wall section was placed in the center, and data was collected as shown by surveying around the perimeter using 4 mobile and 4 stationary nodes. As shown, the image reconstruction is able to resolve the empty space inside the structure and partially separate the interior object. Estimates of the outer wall attenuation average 3.72 dB, measured diagonally through each corner. Laboratory measurements of the outer wall attenuation yielded 6.3 dB. The greater difficulty in reconstructing this image is also evident in the lower SSIM and occupancy indices, which is consistent with the subjectively lower image quality.

The through-wall imaging performance could be improved in several ways. One could depart from our systematic approach to finding $\{\lambda_1, \lambda_2\}$ and manually tune these parameters, as well as place additional constraints on bias vector $\mathbf{b}$ and path loss α. As suggested in Section 4.4.2 and [3], the wall sections could be better estimated by altering the spatial shape of the prior image covariance. We leave this increased scope as a topic for future research.

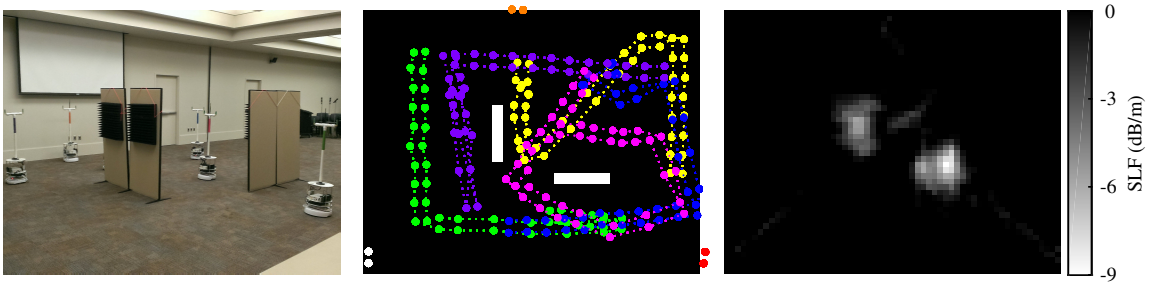

Figure 4.6: Experiment II setup and results. Left: Conference room test setup, showing the attenuating objects and CSOT nodes. Middle: overhead schematic view / binary reference image of the test area, with colored dots showing data sampling locations. Right: SLF image reconstruction from DPSS measurements.

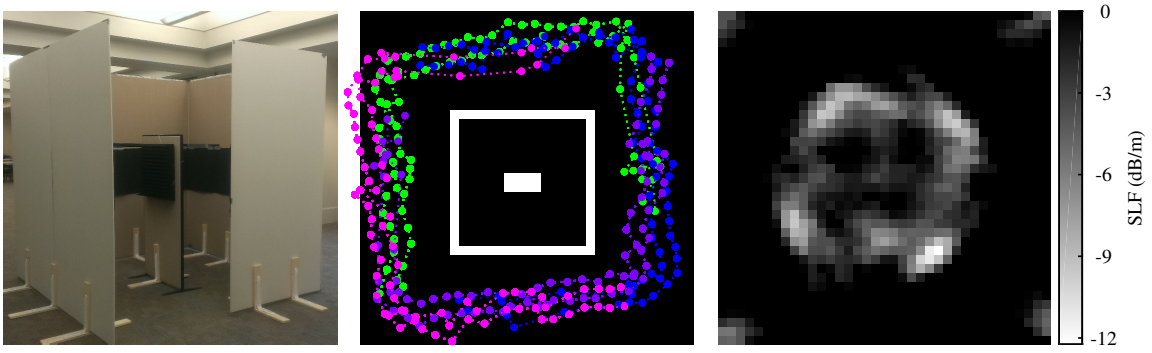

Figure 4.7: Experiment III setup and results. Left: Artificial building test setup, with cutaway showing the interior object. Middle: overhead schematic view / binary reference image of the test area, with colored dots showing data sampling locations. Right: SLF image reconstruction from DPSS measurements.

4.7.4 Penalty for Ignoring Random Effects

The simulation results from Section 4.6 suggest that ignoring link bias and path loss parameters (i.e., using assumed or empirical values) carries a performance penalty regardless of the method used to estimate the image. To get a sense of the influence these parameters may have in practice, we plot the histogram of the estimated $\{\hat{b}_i\}$ in Figure 4.8. The empirical distribution of values gives confidence to our original assumption that this parameter carries a Gaussian distribution; in this case the sample mean is $\hat{\mu}_b = 99.60$ dB and sample standard deviation is $\hat{\sigma}_b = 2.59$ dB.

To visualize the effect of ignoring these parameters, we estimate the standard Tikhonov regularization solution on the data for Experiment II, assuming that all links carry the same bias $\hat{b}_i = \hat{b} = 104.1$ dB and path loss exponent $\alpha = 0.941$ obtained empirically from Figure 4.2. The result is shown in Figure 4.9. The degradation in performance is evident in comparison with our method, particularly the streaking between positions of the stationary nodes. This example illustrates the important observation made in Section 4.2.3 that results for a single pair of nodes may not generalize well to an entire network, despite the estimated parameters strongly fitting the data. This is true even if all nodes share the same hardware, antennas, and power levels, as in our experiments.

4.8 Conclusion

In this chapter we have presented a novel mixed-effects modeling technique for aggregating UWB signal strength measurements in an uncalibrated, mobile network, for the purposes of performing static radio tomographic imaging. We have proposed to use the DPSS metric from a UWB signal as a practical means of managing multipath propagation, in contrast with other approaches. UWB has gained popularity for use in GPS-denied indoor environments, and our imaging may be performed in parallel with cooperative localization of the network. This is very attractive for distributed sensor networks already using UWB for

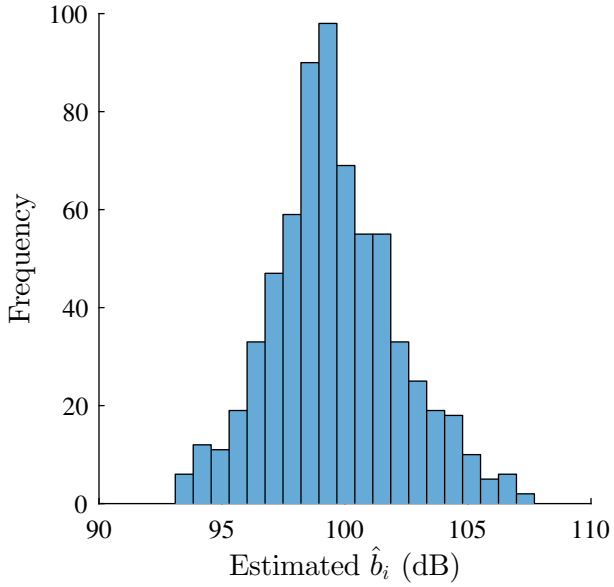

Figure 4.8: Histogram plot showing distribution of values of the estimated $\{\hat{b}_i\}$ across all experiments. The sample mean $\hat{\mu}_b = 99.60$ dB and sample standard deviation $\hat{\sigma}_b = 2.59$ dB.

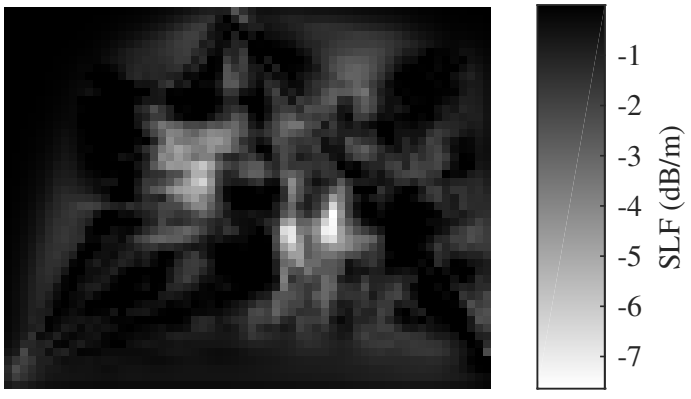

Figure 4.9: Tikhonov regularization solution for Experiment II when ignoring the random effects. $\hat{b}_i = \hat{b} = 104.1$ dB, $\hat{\alpha} = 0.941$ from Figure 4.2. The L-curve method was used to determine $\lambda_2 = 1.003$, and constraint $\hat{\boldsymbol{\theta}} \leq 0$ is applied.

localization or communication, since the network may immediately expand to performing SLAM during localization.

To estimate the unknown SLF image, we have proposed to use a modified convex form of EN regularization. Our simulation results show very attractive performance relative to the derived Bayesian CRLB in the presence of the random effects. In our experimental results we have shown the performance of our methods to estimate both the positions as well as the spatial loss field present in the environment using a mobile, cooperative network.[4]

Future research could focus on a key observation that the UWB pulse signal also captures significant channel information. While the DPSS rejects all energy not propagating along the line of sight, this energy still carries information about the reflective environment. This channel information could be used to also characterize the reflective environment, as in a multistatic radar. The tomographic image (transmitted signals) and radar image (reflected signals) could be highly complementary in characterizing the RF environment.

Our mixed model framework for characterizing biased network parameters could also be applied to other signal processing problems where data is collected from multiple low-cost, uncalibrated sensors. As wireless sensor networks continue to proliferate in greater numbers, directly estimating such parameters from the data becomes more attractive. Results could be applied wherever absolute signal levels are crucial, or when measurements must be compared among uncalibrated sensors.

[4]Datasets are available to other researchers for testing new algorithms via GitHub: `https://github.com/bbeck6/CSOT-UWB-Tomography-Data.git`

CHAPTER 5
UNCOOPERATIVE RSS EMITTER LOCALIZATION IN UNCALIBRATED NETWORKS

5.1 Background and Contributions

As discussed in Chapter 3, accurate positioning of devices (nodes) operating in an area remains an important goal. As before, using the Global Positioning System (GPS) for localization is not always a viable option [24, 84]. This is the case in indoor environments, or when locating uncooperative nodes. In Chapter 3, the sensing modality was two-way time-of-flight (TOF) measurements for cooperative localization. However, many other localization techniques are possible, and localization problems are often classified by the type of sensing mode used to collect data. Other sensing modes include measuring a radio frequency (RF) signal's time-of-arrival (TOA), angle-of-arrival (AOA), or received signal strength (RSS) at the various nodes to estimate the signal source's position [85]. Generally, TOA and AOA techniques provide more accurate localization results, at the cost of requiring synchronization between nodes and specialized antenna hardware, respectively [24]. Other considerations in the localization problem include whether or not the node(s) to be localized will cooperate with the network, and which, if any, of the nodes are mobile.[1]

This chapter considers the localization of a static, uncooperative emitter using a mobile network of sensors taking RSS measurements. There are several potential applications of this scenario. For example, a military unmanned aerial vehicle (UAV) swarm may attempt to locate an enemy radar site or communications tower. Alternatively, ground-based mobile nodes in a mobile ad-hoc network (MANET) may circle a building in an attempt to locate an interior signal source, such as a distress signal. In such scenarios, friendly nodes might

[1] Technical content of this chapter has been submitted for publication in the IEEE Transactions on Wireless Communications.

use GPS to determine their own positions, but another localization method is still needed to determine the position of the uncooperative emitter.

We confine our analysis in this chapter to the case of RSS-based localization, as the ability to make some measurement of received signal power is available to almost any receiver. Further, no synchronization or particular antenna types need be used, which is important if the network contains heterogeneous hardware or is formed on an ad-hoc basis. Within the RSS-based paradigm, approaches generally fall into three broad, overlapping categories in the literature. First are the so-called "fingerprint" routines, in which an indoor area is initially surveyed, and RSS values from the available access points are mapped at many locations. A mobile node's position is estimated by matching its measured RSS to the radio map in some sense [86, 87]. These methods mitigate poor modeling by mapping real observed RSS data, but naturally suffer from the need to pre-survey an area and maintain such a map. An alternative approach is to define a signal strength model which maps RSS data directly onto distances, estimating the location from these derived distances [88, 89, 90, 91]. Doing so enables geometric approaches to position estimation; even sub-optimal linear estimators are possible [86]. While it simplifies the estimator, some information is inevitably lost in the distance mapping process. The third approach, and the one we will consider in this chapter, is to directly estimate the emitter location from the RSS values from the resulting nonlinear model. Some possible estimators include nonlinear least squares [92, 93], maximum likelihood, and convex relaxation techniques [94]. The direct approach avoids loss of accuracy from transforming the data, and is not subject to cumbersome fingerprint survey routines.

When estimating the emitter's position from an RSS model, the presence of additional model parameters must also be considered. These are usually the environmental path loss exponent and the emitter power offset components. The path loss exponent measures the rate of RSS decay with distance, and is a function of the shadowing and multipath environment. The emitter power offset is related to the transmitted signal power, measured at unit

distance. Treatment of these parameters varies widely in the literature. Often assumed values are used, e.g. [95, 96]. Others treat these as nuisance parameters [97], or estimate them via separate, cooperative measurements [98]. Still others attempt to remove unknowns via transformation of the data, usually by differencing [99, 100, 101]. Some nonparametric methods of estimating nuisance parameters in the nonlinear model have been described in [102, 103, 104].

As the title states, we wish to focus on an important practical problem associated with localizing an uncooperative emitter using an *uncalibrated* network of mobile sensors. In such a system, each receiver node produces biased measurements of the "true" RSS, due to natural hardware variations, antennas, method of computing RSS, etc. In the radar target tracking literature, this issue of bias is known as the sensor registration problem [105, 106]. For general localization, some bias models and estimators were considered in [107, 108] when dealing directly with range measurements. In RSS-based localization, the sensor bias/registration problem has been studied for fingerprint methods, e.g. [109, 110, 111, 101], at least with respect to different emitters. At the receiver, [112] showed experimentally that antenna orientation alone can account for over 10 dB of RSS variation between otherwise identical sensors. We note, however, that this particular problem appears to be inadequately addressed when dealing with localization directly from RSS measurements.

In this chapter, we show that this biasing effect can have a substantial impact on localization performance. A common approach when dealing with sensor biases is to model them as unknown nuisance parameters, and estimate them directly along with parameters of interest [113, 114]. However, nonlinear, non-convex estimation algorithms do not scale well with the dimension of the parameter space, which in our case grows with every node in the network. Thus, to avoid an intractable number of nuisance parameters, we choose to treat the network's sensor biases in a statistical manner. We model the bias of each sensor as an additive random variable of unknown variance. It is shown that least-squares estimates of the bias and noise variances can be obtained in closed form, thus giving an

estimate of the data covariance. Knowledge of these statistics are then used to augment the performance of two different estimation algorithms. We consider both a nonlinear least squares (NLS) algorithm and a Gaussian particle filter (GPF) implementation. We show through simulation that our methods substantially mitigate sensor bias with respect to the Cramér Rao lower bound (CRLB), even when the sensor bias is quite large. We then validate these simulations experimentally using real RSS data from a network of mobile sensors. This work is presented as an extension of our uncalibrated localization work in [7]; relevant passages are reproduced where applicable[2].

The chapter is organized as follows. Section 5.2 develops the nonlinear log-distance path loss model for RSS, extended for an uncalibrated network. Closed form estimation of bias and noise statistics (variance parameters) is covered in Section 5.3. Use of these estimates to augment both NLS and GPF algorithms for improved performance is detailed in Section 5.4. Particulars of the CRLB for the model are given in Section 5.5, and performance simulations are covered in Section 5.6. Section 5.7 details the results of our RSS measurement and localization campaign, and finally we give concluding remarks in Section 5.8.

5.2 RSS Measurement Model

5.2.1 Path Loss Model

We consider the problem of estimating the unknown position $\boldsymbol{\beta} = [\beta_x \ \beta_y]^T$ of an emitter in the environment. The extension to three dimensions is straightforward but not considered here. The known position of a given receiver node will be defined by $\mathbf{s} = [s_x \ s_y]^T$. We will use the well known log-distance path loss model to express the drop in RSS as the distance between transmitter and receiver increases. This model has been verified experimentally as a good approximation of the physical effects governing path loss in various environments

[2] © 2016 IEEE. Reproduced with permission.

[24], and is given by

$$P_T - P_R = P_{d_0} + 10\alpha \log_{10} \frac{d}{d_0} + \epsilon \,, \tag{5.1}$$

where P_T, P_R are the transmitted and received power levels expressed in dBm. The reference level P_{d_0} is the path loss at the reference distance d_0, which is often assumed to be 1 meter for indoor localization. $\alpha > 0$ is a unit-less path loss exponent governing the rate of signal decay due to distance, equal to 2 in free space. d is the distance between transmitter and receiver in meters, and ϵ is a "noise" term representing shadowing variations. Often log-normal shadowing is assumed, so that in the dB scale ϵ has a zero-mean Gaussian distribution with some unknown variance σ_ϵ^2. A measured RSS value $z = P_R$ in the frequency band of interest is expressed as

$$z = -10\alpha \log_{10} \|\mathbf{s} - \boldsymbol{\beta}\|_2 + p_0 + \epsilon \,, \tag{5.2}$$

by substituting $p_0 = P_T - P_{d_0}$, $d_0 = 1$ m, and distance $d = \|\mathbf{s} - \boldsymbol{\beta}\|_2$. The 2-norm $\|\cdot\|_2$ represents the Euclidian distance. As discussed in Section 5.1, treatment of the path loss exponent α and power offset p_0 varies in the literature; generally one or both are assumed known a-priori or estimated separately, such as with anchor-to-anchor measurements [95, 96, 98]. However, since an uncooperative emitter may generally operate in an unfamiliar environment at an unknown power level, we assume both p_0 and α to be unknown nuisance parameters.

5.2.2 Bias Effects Extension

Most of the literature on RSS-based localization techniques assumes a stationary sensor network, and that each node produces unbiased measurements z. However, differences in receiver hardware, antenna type/orientation, cable lengths, etc. will introduce an unknown bias for each node. Note that prior calibration of the system is often impractical, particularly as the node count increases. In this section we extend the basic path loss model (5.2)

to incorporate these effects statistically as random variables.

Again, we assume that the network is mobile and consists of N receivers. Let each node i collect a set of M_i RSS values, where $i \in \{1...N\}$. The known position of a receiver node is then given by $\mathbf{s}_{ij} = [s_{ij,x}\ s_{ij,y}]^T$ for node i and RSS data point j. While in general each M_i can be different, in this work we simplify the notation by assuming $M_i = M$, so that each node has the same data size, and $j \in \{1...M\}$. It is assumed that if multiple RSS values are taken at a given node position, they are averaged to obtain a single value.

We incorporate the bias effect of each uncalibrated receiver by assuming an additional additive zero-mean Gaussian random variable $b_i \sim \mathcal{N}(0, \sigma_b^2)$ for each node, so that a single RSS value z_{ij} is given by

$$\begin{aligned} z_{ij} &= -10\alpha \log_{10} \|\mathbf{s}_{ij} - \boldsymbol{\beta}\|_2 + p_0 + b_i + \epsilon_{ij} \\ &= f(\mathbf{s}_{ij}, \boldsymbol{\theta}) + b_i + \epsilon_{ij}\,, \end{aligned} \tag{5.3}$$

where $\boldsymbol{\theta} = [\boldsymbol{\beta}^T, \alpha, p_0]^T$ and we use the nonlinear function $f(\cdot)$ to compact notation and collect nonrandom terms. The bias variance σ_b^2 is considered unknown. Aggregating the data from sensor node i into a vector gives

$$\mathbf{z}_i = \mathbf{f}(\mathbf{s}_i, \boldsymbol{\theta}) + b_i \mathbf{1}_M + \boldsymbol{\epsilon}_i\,, \tag{5.4}$$

where the position vector $\mathbf{s}_i = [\mathbf{s}_{i1}^T ... \mathbf{s}_{iM}^T]^T$. Thus, the data for node i are a function of both fixed parameters common to all nodes in the network $\{\boldsymbol{\beta}, \alpha, p_0\}$, as well as random terms b_i and $\boldsymbol{\epsilon}_i$ which are specific to node i. Viewed in this context, (5.4) has the form of a nonlinear mixed effects model from the field of statistics [77]. Such models are called mixed because the data are defined by random and nonrandom unknowns, and the data may be organized into "bins" (mobile receiver nodes in our case). Our formulation has been called a nonlinear marginal model, because the random terms enter the model in a linear fashion [76].

We assume that the bias and noise terms $\{b_i, \boldsymbol{\epsilon}_i\}$ are independent across nodes $\{i\}$. The within-node noise vector $\boldsymbol{\epsilon}_i$ is assumed to have iid Gaussian components $\boldsymbol{\epsilon}_i \sim \mathcal{N}(\mathbf{0}, \sigma_\epsilon^2 \mathbf{I}_M)$ unless otherwise indicated. Within node i, random variables b_i and $\boldsymbol{\epsilon}_i$ will be considered mutually independent. In subsequent sections, if any of the aforementioned distributional assumptions are not necessary, they will be indicated in context. In any case, it is still assumed that σ_b^2, σ_ϵ^2 are unknown to the system, and are referred to as variance parameters.

5.3 Variance Parameters Estimation

5.3.1 A Note on MLE

A maximum likelihood estimator (MLE) is at least asymptotically efficient, and thus commonly used for well determined problems in which the data samples significantly outnumber the unknown parameters. From (5.4), it is clear that the RSS data for each node have Gaussian distribution $\mathbf{z}_i \sim \mathcal{N}(\mathbf{f}(\mathbf{s}_i, \boldsymbol{\theta}), \mathbf{C}_\mathbf{z})$ with data covariance matrix easily shown to be

$$\mathbf{C}_\mathbf{z} = \sigma_b^2 \mathbf{1}_M \mathbf{1}_M^T + \sigma_\epsilon^2 \mathbf{I}_M \,, \tag{5.5}$$

for the data collected by node i. The corresponding log likelihood function is then given by

$$\mathscr{L}\left(\mathbf{z}_i | \, \boldsymbol{\theta}, \sigma_b^2, \sigma_\epsilon^2\right) = -\frac{M}{2} \ln |\mathbf{C}_\mathbf{z}| - \frac{1}{2} \left(\mathbf{z}_i - \mathbf{f}(\mathbf{s}_i, \boldsymbol{\theta})\right)^T \mathbf{C}_\mathbf{z}^{-1} \left(\mathbf{z}_i - \mathbf{f}(\mathbf{s}_i, \boldsymbol{\theta})\right) \,, \tag{5.6}$$

after dropping the constant term $-M/2 \ln 2\pi$. The likelihood function has closed form because the random terms in our model are additive and linear, thus preserving the Gaussian distribution of the data. However, $\mathscr{L}(\cdot)$ is clearly a nonlinear and non-convex function of parameters $\boldsymbol{\theta}$, σ_b^2, and σ_ϵ^2. Since each node in the network is assumed independent, the MLE can be expressed as the estimator

$$\left\{\hat{\boldsymbol{\theta}}, \hat{\sigma}_b^2, \hat{\sigma}_\epsilon^2\right\} = \underset{\boldsymbol{\theta}, \sigma_b^2, \sigma_\epsilon^2}{\arg\max} \sum_{i=1}^{N} \mathscr{L}\left(\mathbf{z}_i | \, \boldsymbol{\theta}, \sigma_b^2, \sigma_\epsilon^2\right) . \tag{5.7}$$

Solving (5.7) is challenging due to its nonlinearity in $\boldsymbol{\theta}$ and unknown variance parameters σ_b^2, σ_ϵ^2. Various iterative approaches exist in the statistical literature, e.g., [115]. Due to space constraints we refer the reader to the given reference for details of the complex algorithms for nonlinear mixed model MLE. In our work in [7], the MLE was shown to have virtually identical performance to our method of augmenting NLS, and our method is much simpler to implement. Thus we omit the MLE from our results in this work.

5.3.2 Variance Least Squares Estimator

In this section we explain the method used to obtain estimates of variance parameters σ_b^2 and σ_ϵ^2. The complexity of maximizing (5.7) motivated the search for a simpler approach with good performance. In this section we propose to derive and apply a closed-form variance least squares (VLS)-type estimator to estimate vector $\boldsymbol{\theta}$ in the nonlinear model of (5.4). The technique traces back to the work of [116], and general expressions for unbiased and biased versions for a linear mixed model can be found in [76]. The VLS approach has several desirable properties. First, VLS requires us to estimate only the mean and covariance of the data, and thus the Gaussian assumptions of Section 5.2 are not required. Second, VLS generalizes easily to nonlinear models, facilitating derivation and implementation. Finally, our proposed algorithms in Section 5.4 demonstrate very good finite sample performance with respect to the CRLB. Simulation and experimental results are covered in Sections 5.6 and 5.7, respectively.

The basic concept of VLS is intuitively appealing. Assuming an estimate of parameter vector $\boldsymbol{\theta}$ is available, use it to minimize the squared error between the empirical covariance matrix and estimated covariance matrix parametrized by σ_b^2, σ_ϵ^2, doing so across all nodes in the network. In this work, we first obtain an initial estimate via nonlinear least squares. We denote this initial estimate as

$$\hat{\boldsymbol{\theta}}_0 = \arg\min_{\boldsymbol{\theta}} \sum_{i=1}^{N} \|\mathbf{z}_i - \mathbf{f}(\mathbf{s}_i, \boldsymbol{\theta})\|_2^2 = LM(\{\mathbf{z}_i, \mathbf{f}(\cdot)\}) \ , \tag{5.8}$$

where the notation indicates our use of the Levenberg-Marquardt (LM) algorithm [117]. We choose the LM as a compromise between the Gauss-Newton and gradient descent approaches, balancing convergence speed with stability. As with any nonlinear iterative technique, it is advisable to try multiple random initial conditions for $\boldsymbol{\theta}$ in order to avoid local minima. Once the initial NLS estimate $\hat{\boldsymbol{\theta}}_0$ is obtained, it can be used to estimate the true mean of the data for node i, $E[\mathbf{z}_i] = \mathbf{f}(\mathbf{s}_i, \boldsymbol{\theta})$ by making the substitution $\mathbf{f}(\mathbf{s}_i, \hat{\boldsymbol{\theta}}_0)$. In subsequent sections, we will use the index k to indicate that $\hat{\boldsymbol{\theta}}_k$ is the estimate of true parameter $\boldsymbol{\theta}$ at the k-th iteration.

Define the residual vector for node i as $\mathbf{r}_i = \mathbf{z}_i - \mathbf{f}(\mathbf{s}_i, \hat{\boldsymbol{\theta}}_k)$. Thus a scaled empirical covariance matrix for node i can be computed as $\mathbf{r}_i \mathbf{r}_i^T$. VLS seeks the best fit in the least squares sense between this empirical covariance and the theoretical data covariance of (5.5), computed across all nodes in the network. Thus the objective function for VLS is defined to be

$$\begin{aligned} \mathcal{S}\big(\sigma_b^2, \sigma_\epsilon^2\big) &= \sum_{i=1}^{N} \left\| \mathbf{r}_i \mathbf{r}_i^T - \mathbf{C}_{\mathbf{z}}(\sigma_b^2, \sigma_\epsilon^2) \right\|_F^2 \\ &= \sum_{i=1}^{N} \left\| \mathbf{r}_i \mathbf{r}_i^T - \sigma_b^2 \mathbf{1}_M \mathbf{1}_M^T - \sigma_\epsilon^2 \mathbf{I}_M \right\|_F^2, \end{aligned} \tag{5.9}$$

where $\| \cdot \|_F$ indicates the Frobenius matrix norm. It can be shown that the VLS estimates are given in closed form by

$$\hat{\sigma}_b^2 = \frac{1}{N_T(M-1)} \sum_{i=1}^{N} \left(\mathbf{1}_M^T \mathbf{r}_i \mathbf{r}_i^T \mathbf{1}_M - \mathbf{r}_i^T \mathbf{r}_i \right) \tag{5.10}$$

$$\hat{\sigma}_\epsilon^2 = \frac{M}{N_T(M-1)} \sum_{i=1}^{N} \left(\mathbf{r}_i^T \mathbf{r}_i - \frac{1}{M} \mathbf{1}_M^T \mathbf{r}_i \mathbf{r}_i^T \mathbf{1}_M \right), \tag{5.11}$$

where $N_T = N \cdot M$ is the total data size. The detailed proof is provided in Section 5.9.

5.4 Localization Algorithms

In this section we propose two novel localization algorithms for the uncalibrated network model (5.4). Both are informed by the VLS parameter estimates of Section 5.3.2, implicitly accounting for node bias. This statistical approach avoids adding additional nuisance parameters for every receiver node, which would quickly become intractable as N grows. The first algorithm is an extension of NLS via iterative reweighting, and was also covered in our work in [7]. For the second algorithm, we propose a new approach with improved performance, based on Gaussian particle filtering.

5.4.1 NLS-VLS Algorithm

With variance parameter estimates $\hat{\sigma}_b^2$, $\hat{\sigma}_\epsilon^2$, it is possible to transform the basic NLS algorithm by incorporating the estimated data covariance [76]. First the estimated covariance $\hat{\mathbf{C}}_\mathbf{z} = \hat{\sigma}_b^2 \mathbf{1}_M \mathbf{1}_M^T + \hat{\sigma}_\epsilon^2 \mathbf{I}_M$ is used to compute weights via the upper Cholesky decomposition, $\mathbf{W}^T\mathbf{W} = \hat{\mathbf{C}}_\mathbf{z}^{-1}$. Then the data and model are linearly transformed for each node via

$$\{\mathbf{z}_i'\} = \{\mathbf{W}\mathbf{z}_i\} \tag{5.12}$$

$$\{\mathbf{f}'(\mathbf{s}_i, \boldsymbol{\theta})\} = \{\mathbf{W}\mathbf{f}(\mathbf{s}_i, \boldsymbol{\theta})\}\,. \tag{5.13}$$

This transformation is mathematically equivalent to performing nonlinear least squares using the weighted norm $\|\cdot\|^2_{\hat{\mathbf{C}}_\mathbf{z}^{-1}}$ in (5.8). The NLS-VLS algorithm can then proceed to produce a new estimate $\hat{\boldsymbol{\theta}}_1$ by performing a single iteration of the LM least squares algorithm, which we will denote as $LM_+(\{\mathbf{z}_i', \mathbf{f}'(\cdot)\})$. The algorithm alternates between estimating the fixed parameters $\hat{\boldsymbol{\theta}}$ and variance parameters $\hat{\sigma}_b^2$, $\hat{\sigma}_\epsilon^2$ until convergence is reached. We formalize our NLS-VLS estimator in Algorithm 2.

Algorithm 2: NLS-VLS Uncalibrated Localization

Data: RSS data $\{\mathbf{z}_i\}$, positions $\{\mathbf{s}_i\}$ for nodes $i \in \{1...N\}$, convergence tolerance δ
Result: Fixed parameter estimate $\hat{\boldsymbol{\theta}} = [\hat{\boldsymbol{\beta}}^T, \hat{\alpha}, \hat{p}_0]^T$, variance parameter estimates $\hat{\sigma}_b^2$, $\hat{\sigma}_\epsilon^2$

begin
  Initialize iteration $k = 0$;
  Initialize estimate $\hat{\boldsymbol{\theta}}_0 \leftarrow LM(\{\mathbf{z}_i, \mathbf{f}(\cdot)\})$ from (5.8);
  while $\mathrm{STOP} = \mathrm{FALSE}$ **do**
    Residuals $\{\mathbf{r}_i\} \leftarrow \{\mathbf{z}_i - \mathbf{f}(\mathbf{s}_i, \hat{\boldsymbol{\theta}}_k)\}$;
    Variance parameters $\hat{\sigma}_b^2$, $\hat{\sigma}_\epsilon^2$ from (5.10), (5.11);
    Est. covariance matrix $\hat{\mathbf{C}}_\mathbf{z} \leftarrow \hat{\sigma}_b^2 \mathbf{1}_M \mathbf{1}_M^T + \hat{\sigma}_\epsilon^2 \mathbf{I}_M$;
    Weights $\mathbf{W} \leftarrow \mathrm{chol}\left(\hat{\mathbf{C}}_\mathbf{z}^{-1}\right)$;
    Transforms $\{\mathbf{z}_i', \mathbf{f}'(\cdot)\}$ from (5.12),(5.13);
    $\hat{\boldsymbol{\theta}}_{k+1} \leftarrow LM_+(\{\mathbf{z}_i', \mathbf{f}'(\cdot)\})$;
    if $\|\hat{\boldsymbol{\beta}}_{k+1} - \hat{\boldsymbol{\beta}}_k\| < \delta$ **then**
      $\mathrm{STOP} \leftarrow TRUE$
    else
      $k \leftarrow k + 1$;
    end
  end
end

5.4.2 GPF-VLS Algorithm

Particle filtering methods can be extremely powerful; nonlinear dynamic systems can often be modeled very accurately with a sufficient number of particles [114]. In general, a set of candidate "particles" representing the system state $\boldsymbol{\theta}$ are drawn randomly from a sampling distribution. The particles are then weighted according to the likelihood of each particle from the observed data. A resampling or propagation step is then performed to select particles for the next iteration. In this section we introduce a new localization algorithm based on the principles of the Gaussian particle filter (GPF) [118]. We select the GPF specifically because of its natural ability to handle static parameters ($\boldsymbol{\theta}$ in our case). The GPF also does not require a resampling step for the particles. Instead, new particles are drawn from an estimated Gaussian distribution at each iteration.

The key point to consider is that particle filtering algorithms are inherently proba-

Algorithm 3: GPF-VLS Uncalibrated Localization

Data: RSS data $\{\mathbf{z}_i\}$, positions $\{\mathbf{s}_i\}$ for nodes $i \in \{1...N\}$, convergence tolerance δ
Result: Fixed parameter estimate $\hat{\boldsymbol{\theta}} = [\hat{\boldsymbol{\beta}}^T, \hat{\alpha}, \hat{p}_0]^T$, Variance parameter estimates $\hat{\sigma}_b^2$, $\hat{\sigma}_\epsilon^2$

begin
  Initialize iteration $k = 0$;
  Initialize estimate $\hat{\boldsymbol{\theta}}_0 \leftarrow LM(\{\mathbf{z}_i, \mathbf{f}(\cdot)\})$ from (5.8);
  Initialize particles $\mathbf{x}^{(q)} \sim \mathcal{N}(\boldsymbol{\mu}_0, \boldsymbol{\Sigma}_0)$, $q \in \{1...N_p\}$;
  while STOP = FALSE **do**
    Residuals $\{\mathbf{r}_i\} \leftarrow \{\mathbf{z}_i - \mathbf{f}(\mathbf{s}_i, \hat{\boldsymbol{\theta}}_k)\}$;
    Variance parameters $\hat{\sigma}_b^2$, $\hat{\sigma}_\epsilon^2$ from (5.10), (5.11);
    Est. covariance matrix $\hat{\mathbf{C}}_\mathbf{z} \leftarrow \hat{\sigma}_b^2 \mathbf{1}_M \mathbf{1}_M^T + \hat{\sigma}_\epsilon^2 \mathbf{I}_M$;
    Particle weights $w^{(q)} \leftarrow \sum_i \mathscr{L}(\mathbf{z}_i | \mathbf{x}^{(q)})$ from (5.6);
    Normalize weights $w^{(q)} \leftarrow \frac{w^{(q)}}{\sum_q w^{(q)}}$;
    Mean and covariance of filtering density:
    $\boldsymbol{\mu} \leftarrow \sum_q w^{(q)} \mathbf{x}^{(q)}$;
    $\boldsymbol{\Sigma} \leftarrow \sum_q w^{(q)} (\mathbf{x}^{(q)} - \boldsymbol{\mu})(\mathbf{x}^{(q)} - \boldsymbol{\mu})^T$;
    New particles $\mathbf{x}^{(q)} \sim \mathcal{N}(\boldsymbol{\mu}, \boldsymbol{\Sigma}), q \in \{1...N_p\}$;
    Parameter estimate $\hat{\boldsymbol{\theta}}_k \leftarrow \boldsymbol{\mu}$;
    if $\|\hat{\boldsymbol{\beta}}_{k+1} - \hat{\boldsymbol{\beta}}_k\| < \delta$ **then**
      STOP $\leftarrow TRUE$
    else
      $k \leftarrow k + 1$;
    end
  end
end

bilistic. That is, the weight of particle p is optimally determined via the log-likelihood $\sum_i \mathscr{L}(\mathbf{z}_i | \boldsymbol{\theta}^{(p)})$. Clearly from (5.5) and (5.6), the likelihood is dependent on the variance parameters σ_b^2, σ_ϵ^2. Typically these values are either assumed or determined offline through a "tuning" process. While certain particle filtering algorithms could choose to treat these as additional model parameters, it should be noted that increasing the dimension of the parameter space can greatly increase the required particles to maintain performance. Instead we use the VLS closed-form estimates of σ_b^2, σ_ϵ^2 to inform the likelihood function in much the same way that the weights $\mathbf{W}$ inform the NLS-VLS. The detailed procedure is shown in Algorithm 3, including the sampling steps required for a GPF.

5.5 Cramér Rao Lower Bound

The CRLB is a well known lower bound on the variance of an unbiased estimator of a fixed parameter. As such it is useful as a benchmark for the performance of our proposed methods as well as those which fail to account for node bias. Expressions for the general form of the CRLB for the vector Gaussian case are readily available, see e.g., [119]. An unbiased estimator of vector parameter $\boldsymbol{\eta}$ has variances bounded by the Fisher information $E\Big[(\boldsymbol{\eta}-\hat{\boldsymbol{\eta}})_p^2\Big] \geq [\mathbf{F}^{-1}]_{pp}$, and for our problem $\boldsymbol{\eta} = [\boldsymbol{\theta}^T, \sigma_b^2, \sigma_\epsilon^2]^T$. In this special case it can be shown that the Fisher information for node i will have block diagonal form: $\mathbf{F}_i = \mathrm{diag}[\boldsymbol{\mathcal{I}}_i(\boldsymbol{\theta}),\ \boldsymbol{\Psi}_i(\sigma_b^2, \sigma_\epsilon^2)]$ [119]. Since we are primarily interested in $\boldsymbol{\theta}$, we can focus on the expression for the Fisher submatrices $\boldsymbol{\mathcal{I}}_i$, which reduces the Fisher information to the standard Gaussian case

$$[\boldsymbol{\mathcal{I}}_i]_{pq} = \frac{\partial \mathbf{f}(\mathbf{s}_i,\boldsymbol{\theta})}{\partial\,[\boldsymbol{\theta}]_p}^T \mathbf{C}_\mathbf{z}^{-1} \frac{\partial \mathbf{f}(\mathbf{s}_i,\boldsymbol{\theta})}{\partial\,[\boldsymbol{\theta}]_q}\,. \tag{5.14}$$

Since data gathered by each node in the network is assumed independent, we use the additivity property of Fisher information to determine the CRLB for the whole network,

$$\boldsymbol{\mathcal{I}} = \sum_{i=1}^{N} \boldsymbol{\mathcal{I}}_i\,. \tag{5.15}$$

Clearly we are interested in how accurately the emitter's position $\boldsymbol{\beta} = [\beta_x\, \beta_y]^T$ can be estimated. Rather than look at the elements of $\boldsymbol{\beta}$ individually, it is more natural to consider the distance $\|\boldsymbol{\beta}-\hat{\boldsymbol{\beta}}\|_2 = \sqrt{(\beta_x-\hat{\beta}_x)+(\beta_y-\hat{\beta}_y)} = g(\boldsymbol{\beta})$. To do so requires that the CRLB be transformed by the gradient of $g(\boldsymbol{\beta})$,

$$E\Big[\|\boldsymbol{\beta}-\hat{\boldsymbol{\beta}}\|_2^2\Big] \geq \frac{\partial g(\boldsymbol{\beta})}{\partial \boldsymbol{\beta}} \boldsymbol{\mathcal{I}}^{-1} \frac{\partial g(\boldsymbol{\beta})^T}{\partial \boldsymbol{\beta}}\,. \tag{5.16}$$

Note that the gradient of $g(\cdot)$ with respect to the other parameters is zero, ensuring that the dimensions agree. We use the expression in (5.16) to bound the (root) mean-squared error (MSE) in simulation. In this case the CRLB depends on the unknown parameters as well as the geometry of the problem, requiring that many random configurations be simulated to obtain an average lower bound.

5.6 Performance Simulations

We have performed simulations of our uncalibrated network RSS measurement model of Section 5.2 to demonstrate the performance of our VLS-augmented algorithms in Section 5.4. The CRLB of Section 5.5 for the uncalibrated network is also simulated to provide a lower bound on root mean squared error (RMSE) for localization of the emitter. To demonstrate the effect of ignoring the sensor bias, we also include the performance of the standard NLS [117] and GPF [118] algorithms. These naive estimators omit the VLS steps and assume unbiased data from all nodes, as is normally the case in the localization literature.

We choose simulation parameters to be relatively consistent with the scale of our experimental results, covered in Section 5.7. Each iteration simulates N mobile nodes each collecting M RSS values according to model (5.4), while taking a random walk through a 50×50 m area. The step length for each node is normally distributed with zero mean and standard deviation $\sigma = 0.5$ m. The target emitter is randomly placed in the 20×20 m area in the center. Parameters α and p_0 are selected at each run from uniform distributions $\mathcal{U}[2, 4]$ and $\mathcal{U}[-50, -10]$ dBm, respectively. The variance parameters are also selected to be similar to the experimentally estimated values. We fix the noise variance parameter at $\sigma_\epsilon = 4$ dB, and bias at $\sigma_b = 6$ dB. Additionally, $N_p = 500$ particles are used for the particle filters, and exact knowledge of σ_ϵ^2 is granted to the naive GPF algorithm.

The simulation results are shown in Figure 5.1. The RMSE of each algorithm is plotted vs. node count N, with each successive plot showing the effect of increasing the data per

node M. In the top plot of Figure 5.1, each node gathers only $M = 25$ RSS values. The small data set for each node is still sufficient for a performance improvement when using VLS over the naive methods. The GPF-VLS, for example, improves upon the GPF by an average of 1.04 m, or 14%. Increasing each node's data to $M = 50$ makes the performance improvements much more evident. In this case, the GPF-VLS reduces the RMSE over the GPF by an average of 3.17 m, or 41%. Finally, we highlight the bottom plot of Figure 5.1, where M is increased further to 100 RSS values per node. Here the GPF-VLS is virtually efficient for $N > 10$. This corresponds to improving RMSE over the GPF by an average 5.46 m, or 67%, a very significant improvement.

We also note the performance improvement of the particle filter based GPF-VLS over the nonlinear least squares based NLS-VLS. Particle filters in general handle nonlinear models very naturally without the linearizing approximations made in NLS type algorithms. The result is a significant jump in efficiency provided the sensor bias is accounted for. The drawback is computational cost, especially for large numbers of particles. We do not provide a quantitative analysis of computational cost here, as this will depend upon the implementation of each algorithm, however we note that it exists. If convergence time over accuracy is a priority, the NLS-VLS may be preferable.

It is clear from (5.15) and the positive semidefinite property of the Fisher information that the CRLB will decrease with increasing node count N. However, also observe in the three plots of Figure 5.1 that the CRLB also drops with increasing data per node M. This property would be difficult to show analytically for our model, however the behavior is clear from the simulations. Also as shown in Figure 5.1, both the GPF-VLS and NLS-VLS become more efficient as the data per node M increases. These observations are interesting in that performance can be improved by increasing either the number of uncalibrated sensors N, or the quantity of data each collects, M.

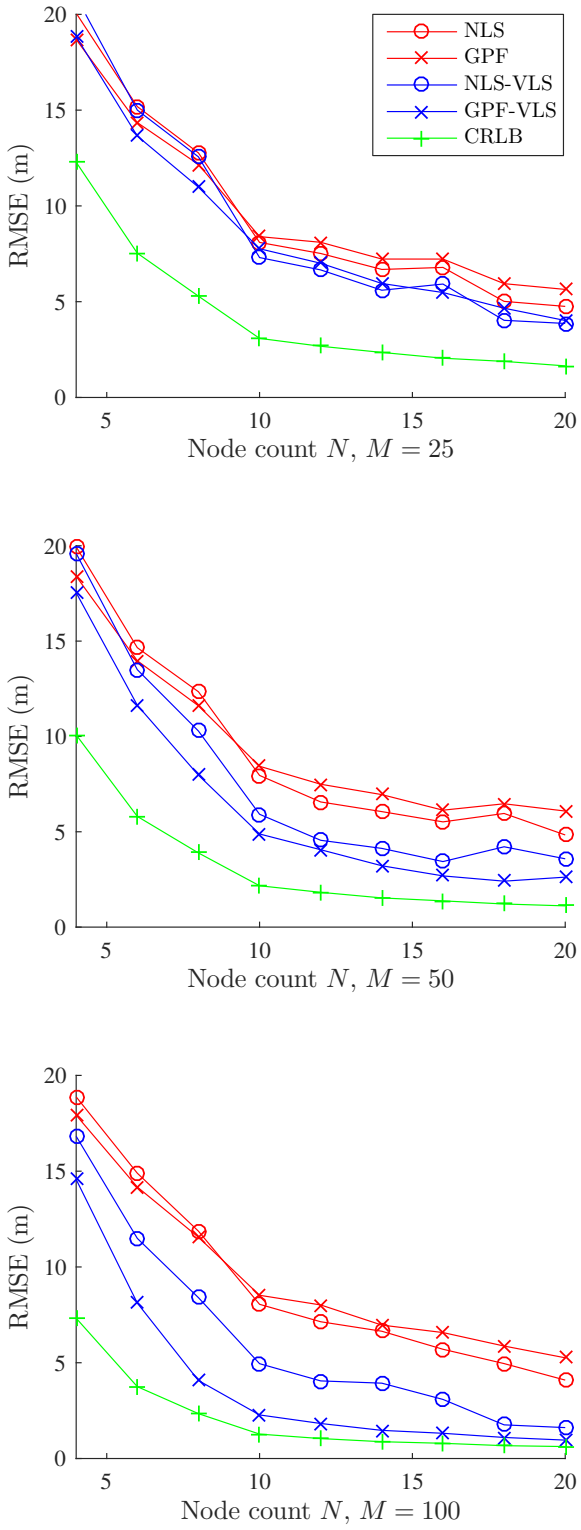

Figure 5.1: Simulation results of the proposed methods, naive estimators, and CRLB. 960 random simulations were averaged for each data point.

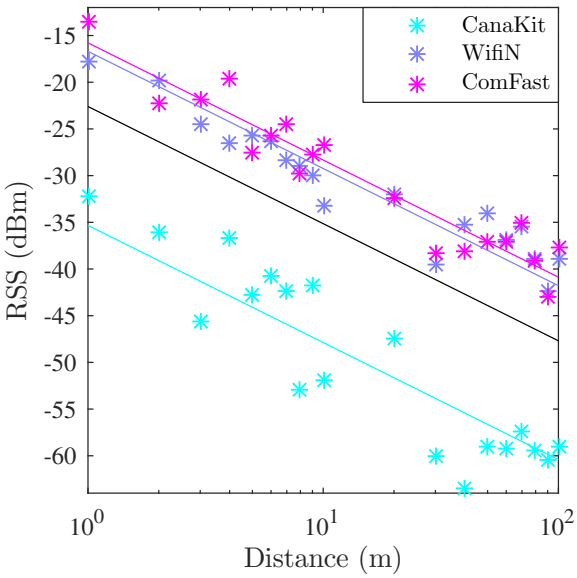

Figure 5.2: Outdoor RSS data collection. The global mean fit is indicated by the black line; colored lines are best fit for each receiver type. Path loss exponent $\hat{\alpha} = 1.25$.

5.7 Experimental Results

5.7.1 Hardware and Measured Bias Effects

For the experimental campaign, the 2.4 GHz band was chosen for its ubiquity and ease of data collection. Likewise, localization of such signals is a common theme in the literature. The mobile receiver nodes consist of three distinct, commercially available WiFi adapter models with different stock antenna configurations. These adapters are shown in Figure 5.3. The uncooperative emitter is an 802.11n WiFi router, nominally transmitting at 20 dBm.

To examine the effect of the heterogeneous hardware on measuring RSS, an outdoor experiment was first performed. RSS data was gathered from each receiver node over a wide range of distances up to 100 m. The results are plotted in Figure 5.2, showing the best fit lines for the global mean data as well as the individual units. These results illustrate the clear variation between the individuals and the mean; estimated bias levels are -12.7, 5.91, and 6.82 dBm for CanaKit, WifiN, and Comfast adapters, respectively. The effects of this variation between units on localization performance are examined in the following section.

5.7.2 Indoor Localization

We have performed indoor localization experiments to test the real performance of our proposed algorithms in Section 5.4. The experiments are based on one of the proposed use cases in Section 5.1, that is, a set of mobile receivers encircling a building searching for an interior emitter. A view of the laboratory setting of the experiments is shown in Figure 5.4. Two of each of the aforementioned receiver units were used so that $N = 6$ for the experiments. $M = 50$ RSS values were gathered by each node, which allowed the nodes to move approximately 0.5 m at each time step without significant overlap.

Graphical results for Experiment I are plotted in Figure 5.5. The overhead schematic view illustrates the relative performance of each algorithm in locating the emitter, as well as RSS data collection points. The detailed numerical results are provided in Table 5.1. Examining the results for Experiment I shows the NLS-VLS and GPF-VLS algorithms reducing RMSE by 1.72 m (18.2%) and 3.15 m (35.4%) when compared to the naive NLS and GPF, respectively. Note also that both VLS augmented algorithms estimate a significant bias variance parameter; the values are $\sigma_b = 5.89$ dB and $\sigma_b = 6.62$ dB.

For Experiment II, virtually the same sensor geometry is replicated from Experiment I. The difference lies in choice of sensor type used for each path. This can be seen in the colored dots used for each receiver type, plotted in Figure 5.6. This result demonstrates the spatial impact of the individual sensor bias on the localization solutions. The naive NLS and GPF algorithms both deteriorate significantly in performance, with the NLS giving particularly poor results off of the lower map edge. This is not a problem for the VLS augmented algorithms; in fact their performance in this experiment actually improves. The numerical results can also be found in Table 5.1. NLS-VLS and GPF-VLS each improve over the naive methods by 30.6 m (92.1%) and 9.98 m (80.7%).

Figure 5.3: Heterogeneous receiver hardware used in the experiments. Left to right, WiFi adapters from CanaKit, WifiN, and Comfast shown with Raspberry Pi controllers. Nodes were supported by movable tripods during testing.

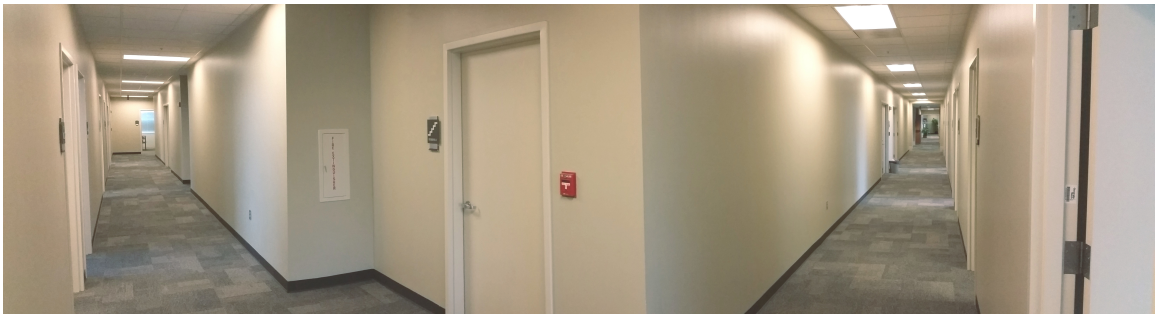

Figure 5.4: Panoramic view of test area, as seen from the origin.

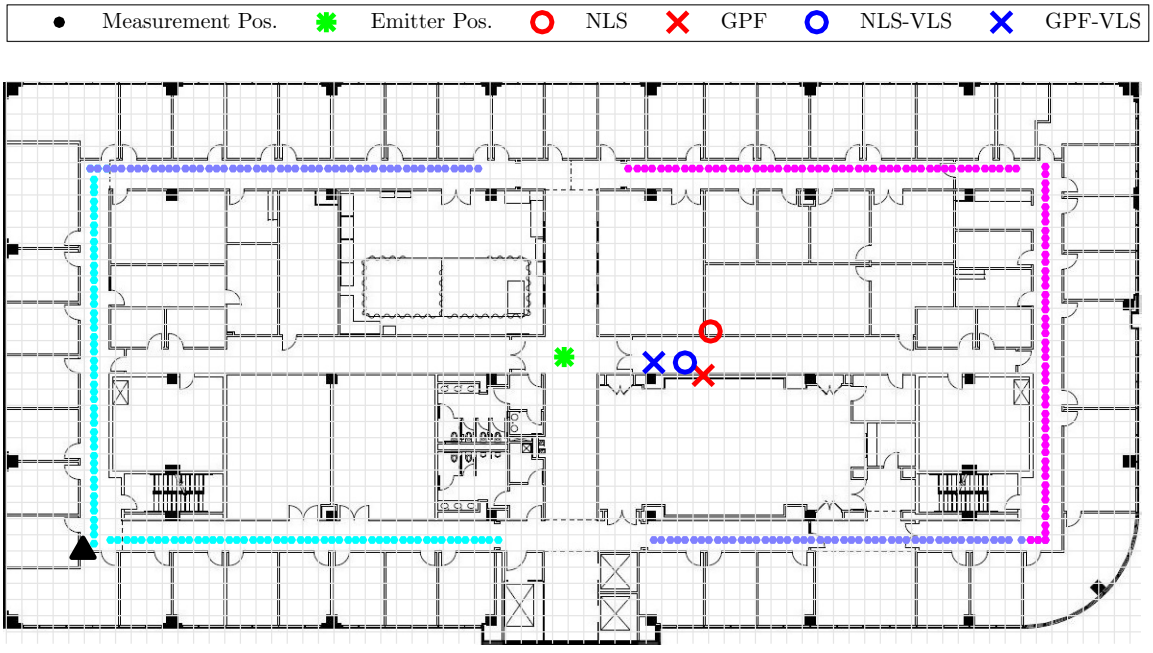

Figure 5.5: Experiment I results in indoor environment. Dot colors indicate the type of mobile sensor used to record RSS: CanaKit, WifiN, and Comfast adapters are indicated by cyan, light purple, and magenta, respectively. Each grid space equals one square meter. The origin is indicated by the black triangle in the lower left.

Table 5.1: Uncalibrated Localization Campaign Summary.

	Exp. I	**Exp. II**
Number of mobile nodes, N	6	
Number of unique RX hardware	3 (2 ea. type)	
Data per node, M	50	
Test area size (m)	25×63	
Approx. emitter TX power (dBm)	20	
NLS:		
Position RMSE (m)	9.43	33.2
Est. α	5.33	5.82
GPF:		
Position RMSE (m)	8.90	12.37
Est. α	5.65	3.83
NLS-VLS:		
Position RMSE (m)	7.71	2.63
Est. α	4.28	3.92
Est. σ_ϵ (dB)	4.06	4.76
Est. σ_b (dB)	5.89	8.23
GPF-VLS:		
Position RMSE (m)	5.75	2.39
Est. α	3.99	3.91
Est. σ_ϵ (dB)	4.06	4.76
Est. σ_b (dB)	6.62	8.16

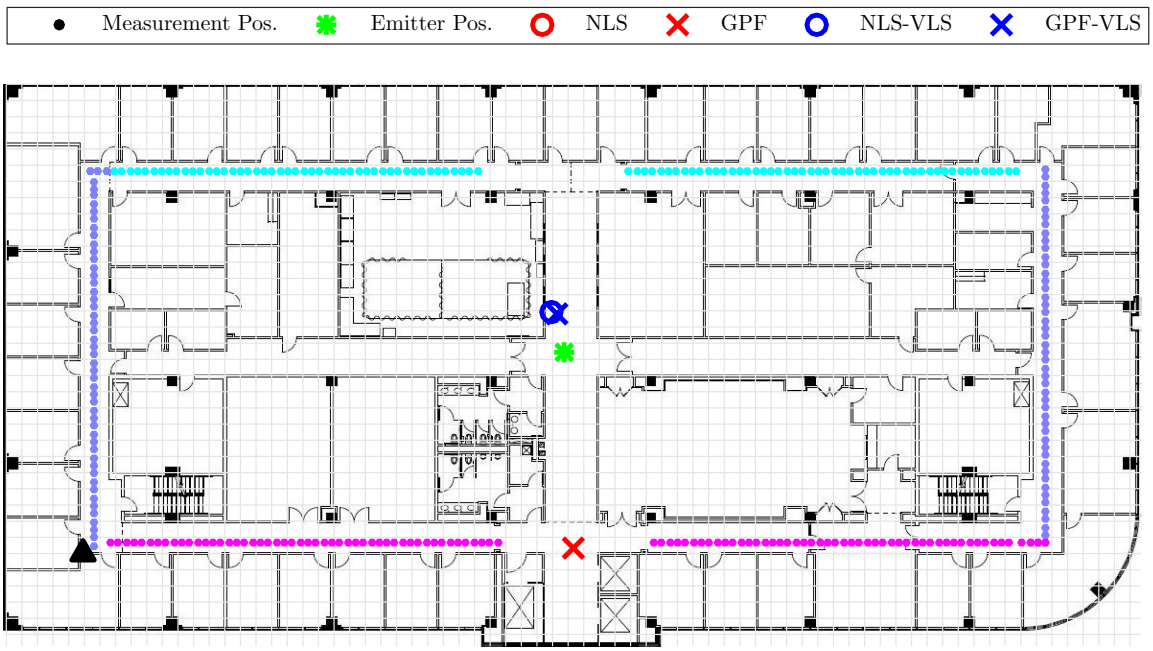

Figure 5.6: Experiment II results with a different arrangement of sensors. Coloration to indicate sensor type is identical to Experiment I, Figure 5.5. The NLS solution $(27.5, -20.4)$ m is outside the visible area of the map.

5.8 Conclusion

In this chapter we have explored the effects of individual receiver bias on the localization of an uncooperative emitter. Both simulation and experimental results show that this effect can be significant and degrade the efficiency of localization algorithms. Even powerful nonlinear techniques such as the GPF do not handle these effects well. Additionally, prior calibration of sensors is cumbersome, and may not be possible in an ad-hoc scenario. Furthermore, the simple approach of augmenting parameter vector $\boldsymbol{\theta}$ with additional unknowns quickly becomes intractable for nonlinear models.

Instead we have chosen to take a statistical approach, estimating the effects of the bias on the data vector through the covariance. This method improves in performance not only as more data is collected for a given node, but also as the network size grows. We have shown the substantial performance improvement over naive methods in the general case through simulations. Experimental results have indicated an improvement in accuracy even

in real localization scenarios.

Future research could focus on expanding these results to new use cases. Generalizing these methods to the case of a mobile uncooperative emitter could prove very beneficial. Other localization paradigms, such as AOA, could also be investigated. Finally, expanding to other frequency bands, such as joint estimation utilizing 5 GHz WiFi signals, may improve accuracy even further.

5.9 Chapter Appendix: VLS Derivation

He we prove the results in (5.10) and (5.11). The starting point is very similar to the methods used in [76] for a general linear model, though here we show that for our model (5.4) the estimates simplify substantially into fully separable form. Returning to the cost function (5.9):

$$\begin{aligned}\mathcal{S}\big(\sigma_b^2,\sigma_\epsilon^2\big) &= \sum_{i=1}^{N}\left\|\mathbf{r}_i\mathbf{r}_i^T-\mathbf{C}_{\mathbf{z}}(\sigma_b^2,\sigma_\epsilon^2)\right\|_F^2 \\ &= \sum_{i=1}^{N}\left\|\mathbf{r}_i\mathbf{r}_i^T-\sigma_b^2\mathbf{1}_M\mathbf{1}_M^T-\sigma_\epsilon^2\mathbf{I}_M\right\|_F^2, \end{aligned} \tag{5.17}$$

where $\mathbf{r}_i = \mathbf{z}_i - \mathbf{f}(\mathbf{s}_i,\hat{\boldsymbol{\theta}}_k) \in \mathbb{R}^M$ is the residual computed at the current estimate of the parameters $\hat{\boldsymbol{\theta}}_k$, for node $i \in \{1...N\}$, and iteration k. Now note that for a symmetric matrix $\mathbf{A}$, the property $\|\mathbf{A}\|_F^2 = \mathrm{Tr}(\mathbf{A}^T\mathbf{A}) = \mathrm{Tr}(\mathbf{A}^2)$ holds. Substituting into (5.17) yields

$$\mathcal{S}\big(\sigma_b^2,\sigma_\epsilon^2\big) = \sum_{i=1}^{N}\mathrm{Tr}\Big(\big(\mathbf{r}_i\mathbf{r}_i^T-\sigma_b^2\mathbf{1}_M\mathbf{1}_M^T-\sigma_\epsilon^2\mathbf{I}_M\big)^2\Big). \tag{5.18}$$

Differentiating (5.18) with respect to σ_b^2 and expanding gives

$$\begin{aligned}\frac{\partial \mathcal{S}}{\partial \sigma_b^2} &= \sum_{i=1}^{N} \operatorname{Tr}\left(2\left(\mathbf{r}_i\mathbf{r}_i^T - \sigma_b^2\mathbf{1}_M\mathbf{1}_M^T - \sigma_\epsilon^2\mathbf{I}_M\right)\left(-\mathbf{1}_M\mathbf{1}_M^T\right)\right) \\ &= 2\left(\sigma_b^2 N_T M + \sigma_\epsilon^2 N_T - \sum_{i=1}^{N} \operatorname{Tr}\left(\mathbf{r}_i\mathbf{r}_i^T\mathbf{1}_M\mathbf{1}_M^T\right)\right) \\ &= 2\left(\sigma_b^2 N_T M + \sigma_\epsilon^2 N_T - \sum_{i=1}^{N} \mathbf{1}_M^T\mathbf{r}_i\mathbf{r}_i^T\mathbf{1}_M\right).\end{aligned}$$

Note that as before, $N_T = N \cdot M$ is the total data size. The final step holds via the cyclic property of trace and trace of a scalar: $\operatorname{Tr}(\mathbf{a}\mathbf{a}^T\mathbf{b}\mathbf{b}^T) = \operatorname{Tr}(\mathbf{b}^T\mathbf{a}\mathbf{a}^T\mathbf{b}) = \mathbf{b}^T\mathbf{a}\mathbf{a}^T\mathbf{b}$. Setting equal to zero and solving for σ_b^2 yields

$$\sigma_b^2 = \frac{1}{N_T \cdot M}\sum_{i=1}^{N} \mathbf{1}_M^T\mathbf{r}_i\mathbf{r}_i^T\mathbf{1}_M - \sigma_\epsilon^2\frac{1}{M}. \tag{5.19}$$

Differentiating (5.18) with respect to σ_ϵ^2 and performing a very similar sequence of steps gives

$$\sigma_\epsilon^2 = \frac{1}{N_T}\sum_{i=1}^{N} \mathbf{r}_i^T\mathbf{r}_i - \sigma_b^2. \tag{5.20}$$

The results (5.19) and (5.20) are then easily solved via substitution to obtain the final separable results

$$\begin{aligned}\hat{\sigma}_b^2 &= \frac{1}{N_T(M-1)}\sum_{i=1}^{N}\left(\mathbf{1}_M^T\mathbf{r}_i\mathbf{r}_i^T\mathbf{1}_M - \mathbf{r}_i^T\mathbf{r}_i\right) \\ \hat{\sigma}_\epsilon^2 &= \frac{M}{N_T(M-1)}\sum_{i=1}^{N}\left(\mathbf{r}_i^T\mathbf{r}_i - \frac{1}{M}\mathbf{1}_M^T\mathbf{r}_i\mathbf{r}_i^T\mathbf{1}_M\right).\end{aligned}$$

REFERENCES

[1] B. Beck, R. Baxley, and X. Ma, "Improving radio tomographic images using multipath signals," in *Proc. IEEE Int. Conf. on Wireless Inform. Technol. and Syst. (ICWITS)*, Nov. 2012, pp. 1–4.

[2] B. Beck, J. Kim, R. Baxley, *et al.*, "RadioBOT: A spatial cognitive radio testbed," in *Proc. IEEE Aerospace Conf.*, Mar. 2013, pp. 1–9.

[3] B. Beck, R. Baxley, and X. Ma, "Regularization techniques for floor plan estimation in radio tomographic imaging," in *Proc. IEEE Global Conf. on Signal and Inform. Process. (GlobalSIP)*, Dec. 2013, pp. 177–180.

[4] B. Beck and R. Baxley, "Anchor free node tracking using ranges, odometry, and multidimensional scaling," in *Proc. IEEE Int. Conf. on Acoustics, Speech and Signal Process. (ICASSP)*, May 2014, pp. 2209–2213.

[5] B. Beck, R. Baxley, and J. Kim, "Real-time, anchor-free node tracking using ultra-wideband range and odometry data," in *Proc. IEEE Int. Conf. on Ultra-Wideband (ICUWB)*, Aug. 2014, pp. 286–291.

[6] B. Beck, X. Ma, and R. Baxley, "Ultra-wideband tomographic imaging in uncalibrated networks," *IEEE Trans. Wireless Commun.*, vol. 15, no. 9, pp. 6474–6486, Sep. 2016.

[7] B. Beck, R. Baxley, and X. Ma, "Uncooperative RSS-based emitter localization in uncalibrated mobile networks," in *Proc. 17th IEEE Int. Workshop on Signal Proc. Advances in Wireless Commun. (SPAWC)*, Jul. 2016, pp. 1–6.

[8] B. Beck, S. Lanh, R. Baxley, *et al.*, "Uncooperative emitter localization using signal strength in uncalibrated mobile networks," *IEEE Trans. Wireless Commun.*, 2016.

[9] P. Rawat, K. Singh, H. Chaouchi, *et al.*, "Wireless sensor networks: A survey on recent developments and potential synergies," *J. of Supercomputing*, vol. 68, no. 1, pp. 1–48, Apr. 2014.

[10] J. Wilson and N. Patwari, "Radio tomographic imaging with wireless networks," *IEEE Trans. Mobile Comput.*, vol. 9, pp. 621–632, May 2010.

[11] B. Fette, *Cognitive radio technology*, 2nd ed., B. Fette, Ed., ser. Electronics & Electrical. Academic Press, 2009.

[12] I. F. Akyildiz, W.-Y. Lee, M. C. Vuran, *et al.*, "Next generation/dynamic spectrum access/cognitive radio wireless networks: A survey," *Comput. Networks*, vol. 50, no. 13, pp. 2127–2159, Sep. 2006.

[13] K. Kim, I. Akbar, K. Bae, *et al.*, "Cyclostationary approaches to signal detection and classification in cognitive radio," in *Proc. 2nd IEEE Int. Symp. on New Frontiers in Dynamic Spectrum Access Networks*, Apr. 2007, pp. 212–215.

[14] R. Chen, J.-M. Park, and J. Reed, "Defense against primary user emulation attacks in cognitive radio networks," *IEEE J. Sel. Areas Commun.*, vol. 26, no. 1, pp. 25–37, Jan. 2008.

[15] R. Chen, J.-M. Park, Y. Hou, *et al.*, "Toward secure distributed spectrum sensing in cognitive radio networks," *IEEE Commun. Mag.*, vol. 46, no. 4, pp. 50–55, Apr. 2008.

[16] Y. Zhao, J. H. Reed, S. Mao, *et al.*, "Overhead analysis for radio environment map enabled cognitive radio networks," in *Proc. 1st IEEE Workshop on Networking Technol. for Software Defined Radio Networks*, Sep. 2006, pp. 18–25.

[17] B. R. Hamilton, X. Ma, R. Baxley, *et al.*, "Radio frequency tomography in mobile networks," in *Proc. IEEE Statist. Signal Process. Workshop (SSP)*, Aug. 2012, pp. 508–511.

[18] M. Dillinger, K. Madani, and N. Alonistioti, *Software defined radio: Architectures, systems and functions*, ser. Wiley Series in Software Radio. John Wiley & Sons, 2004.

[19] S.-J. Kim, E. Dall'Anese, and G. Giannakis, "Cooperative spectrum sensing for cognitive radios using kriged Kalman filtering," *IEEE J. Sel. Topics Signal Process.*, vol. 5, no. 1, pp. 24–36, Feb. 2011.

[20] G. Mateos, J.-A. Bazerque, and G. Giannakis, "Spline-based spectrum cartography for cognitive radios," in *Proc. 43rd Asilomar Conf. on Signals, Sys. and Comput.*, Nov. 2009, pp. 1025–1029.

[21] J. Bazerque, G. Mateos, and G. Giannakis, "Basis pursuit for spectrum cartography," in *Proc. IEEE Int. Conf. on Acoustics, Speech and Signal Process. (ICASSP)*, May 2011, pp. 2992–2995.

[22] ——, "Group-lasso on splines for spectrum cartography," *IEEE Trans. Signal Process.*, vol. 59, no. 10, pp. 4648–4663, Oct. 2011.

[23] D. T. Sandwell, "Biharmonic spline interpolation of GEOS-3 and SEASAT altimeter data," *Geophysical Res. Lett.*, vol. 14, no. 2, pp. 139–142, Feb. 1987.

[24] N. Patwari, J. Ash, S. Kyperountas, *et al.*, "Locating the nodes: Cooperative localization in wireless sensor networks," *IEEE Signal Process. Mag.*, vol. 22, no. 4, pp. 54–69, Jul. 2005.

[25] H. Wymeersch, J. Lien, and M. Win, "Cooperative localization in wireless networks," *Proc. IEEE*, vol. 97, no. 2, pp. 427–450, Feb. 2009.

[26] D. Schneider, "New indoor navigation technologies work where GPS can't," *IEEE Spectrum*, vol. 50, no. 12, pp. 34–39, Dec. 2013.

[27] S. Gezici, Z. Tian, G. Giannakis, *et al.*, "Localization via ultra-wideband radios: A look at positioning aspects for future sensor networks," *IEEE Signal Process. Mag.*, vol. 22, no. 4, pp. 70–84, Jul. 2005.

[28] I. Borg and P. Groenen, *Modern multidimensional scaling*, ser. Springer Series in Statistics. Springer-Verlag New York, 1997.

[29] K. Cheung and H. So, "A multidimensional scaling framework for mobile location using time-of-arrival measurements," *IEEE Trans. Signal Process.*, vol. 53, no. 2, pp. 460–470, Feb. 2005.

[30] D. Macagnano and G. De Abreu, "Tracking multiple dynamic targets with multidimensional scaling," in *Proc. IEEE 18th Int. Symp. on Personal, Indoor and Mobile Radio Commun. (PIMRC)*, Sep. 2007, pp. 1–5.

[31] F. Chan and H. So, "Efficient weighted multidimensional scaling for wireless sensor network localization," *IEEE Trans. Signal Process.*, vol. 57, no. 11, pp. 4548–4553, Nov. 2009.

[32] J. Costa, N. Patwari, and A. Hero, "Distributed weighted-multidimensional scaling for node localization in sensor networks," *ACM Trans. on Sensor Networks*, vol. 2, no. 1, pp. 39–64, Feb. 2006.

[33] O. Kwon and H. Song, "Localization through map stitching in wireless sensor networks," *IEEE Trans. Parallel Distrib. Syst.*, vol. 19, no. 1, pp. 93–105, Jan. 2008.

[34] O. Kwon, H. Song, and S. Park, "Anchor-free localization through flip-error resistant map stitching in wireless sensor network," *IEEE Trans. Parallel Distrib. Syst.*, vol. 21, no. 11, pp. 1644–1657, Nov. 2010.

[35] A. Amar, Y. Wang, and G. Leus, "Extending the classical multidimensional scaling algorithm given partial pairwise distance measurements," *IEEE Signal Process. Lett.*, vol. 17, no. 5, pp. 473–476, May 2010.

[36] P. Drineas, A. Javed, M. Magdon-Ismail, *et al.*, "Distance matrix reconstruction from incomplete distance information for sensor network localization," in *Proc. 3rd Annu. IEEE Commun. Soc. on Sensor and Ad Hoc Commun. and Networks (SECON)*, vol. 2, Sep. 2006, pp. 536–544.

[37] Y. Shang and W. Ruml, "Improved MDS-based localization," in *Proc. IEEE Joint Conf. of Comput. and Commun. Soc. (INFOCOM)*, vol. 4, Mar. 2004, pp. 2640–2651.

[38] H. Jamali-Rad and G. Leus, "Dynamic multidimensional scaling for low-complexity mobile network tracking," *IEEE Trans. Signal Process.*, vol. 60, no. 8, pp. 4485–4491, Aug. 2012.

[39] A. Al-Fuqaha, M. Elbes, and A. Rayes, "An intelligent data fusion technique based on the particle filter to perform precise outdoor localization," *Int. J. of Pervasive Comput. and Commun.*, vol. 9, no. 2, pp. 163–183, 2013.

[40] J. Corrales, F. Candelas, and F. Torres, "Hybrid tracking of human operators using IMU/UWB data fusion by a Kalman filter," in *Proc. 3rd ACM/IEEE Int. Conf. on Human-Robot Interaction (HRI)*, Mar. 2008, pp. 193–200.

[41] E. North, J. Georgy, M. Tarbouchi, *et al.*, "Enhanced mobile robot outdoor localization using INS/GPS integration," in *Proc. Int. Conf. on Comput. Eng. Syst. (ICCES)*, Dec. 2009, pp. 127–132.

[42] H. Wang, H. Lenz, A. Szabo, *et al.*, "WLAN-based pedestrian tracking using particle filters and low-cost MEMS sensors," in *Proc. 4th Workshop on Positioning, Navigation and Commun. (WPNC)*, Mar. 2007, pp. 1–7.

[43] H. Durrant-Whyte and T. Bailey, "Simultaneous localization and mapping (SLAM): Part I," *IEEE Robot. Autom. Mag.*, vol. 13, no. 2, pp. 99–110, Sep. 2006.

[44] T. Bailey and H. Durrant-Whyte, "Simultaneous localization and mapping (SLAM): Part II," *IEEE Robot. Autom. Mag.*, vol. 13, no. 3, pp. 108–117, Sep. 2006.

[45] R. C. Luo and C. C. Lai, "Multisensor fusion-based concurrent environment mapping and moving object detection for intelligent service robotics," *IEEE Trans. Ind. Electron.*, vol. 61, no. 8, pp. 4043–4051, Aug. 2014.

[46] E. Dall'Anese, S. J. Kim, and G. Giannakis, "Channel gain map tracking via distributed kriging," *IEEE Trans. Veh. Technol.*, vol. 60, no. 3, pp. 1205–1211, Mar. 2011.

[47] E. J. Baranoski, "Through-wall imaging: Historical perspective and future directions," *J. of the Franklin Inst.*, vol. 345, no. 6, pp. 556–569, Sep. 2008.

[48] D. Hill, "Radio propagation in a coal seam and the inverse problem," *J. of Research of the Nat. Bureau of Standards*, vol. 89, no. 5, p. 36, Sep. 1984.

[49] L. Stolarczyk, G. Rogers, and P. Hatherly, "Comparison of radio imaging method (RIM) electromagnetic wave tomography with in-mine geological mapping in the Liddell, Bulli and Wongawilli coal seams," *Exploration Geophysics*, vol. 19, no. 2, pp. 169–170, Jan. 1988.

[50] N. Pendock, "Radio-wave tomography for geological mapping," in *Proc. of SPIE*, vol. 1942, Nov. 1993, pp. 96–104.

[51] L. Lo Monte, D. Erricolo, F. Soldovieri, *et al.*, "Radio frequency tomography for tunnel detection," *IEEE Trans. Geosci. Remote Sens.*, vol. 48, no. 3, pp. 1128–1137, Mar. 2010.

[52] N. Patwari and J. Wilson, "RF sensor networks for device-free localization: Measurements, models, and algorithms," *Proc. IEEE*, vol. 98, no. 11, pp. 1961–1973, Nov. 2010.

[53] J. Wilson and N. Patwari, "See-through walls: Motion tracking using variance-based radio tomography networks," *IEEE Trans. Mobile Comput.*, vol. 10, no. 5, pp. 612–621, May 2011.

[54] J. Wilson, N. Patwari, and F. Vasquez, "Regularization methods for radio tomographic imaging," in *Proc. Virginia Tech Symp. on Wireless Personal Commun.*, Jun. 2009.

[55] N. Patwari and P. Agrawal, "NESH: A joint shadowing model for links in a multi-hop network," in *Proc. IEEE Int. Conf. on Acoustics, Speech, and Signal Processing (ICASSP)*, Apr. 2008, pp. 2873–2876.

[56] B. Hamilton, X. Ma, and R. Baxley, "SAL: Shadowing assisted localization," in *Proc. IEEE Statist. Signal Process. Workshop (SSP)*, Jun. 2011, pp. 229–232.

[57] Y. Mostofi, "Cooperative wireless-based obstacle/object mapping and see-through capabilities in robotic networks," *IEEE Trans. Mobile Comput.*, vol. 12, no. 5, pp. 817–829, May 2013.

[58] A. Gonzalez-Ruiz and Y. Mostofi, "Cooperative robotic structure mapping using wireless measurements - a comparison of random and coordinated sampling patterns," *IEEE Sensors J.*, vol. 13, no. 7, pp. 2571–2580, Apr. 2013.

[59] A. Gonzalez-Ruiz, A. Ghaffarkhah, and Y. Mostofi, "An integrated framework for obstacle mapping with see-through capabilities using laser and wireless channel measurements," *IEEE Sensors J.*, vol. 14, no. 1, pp. 25–38, Jan. 2014.

[60] R. Fontana, "Recent system applications of short-pulse ultra-wideband (UWB) technology," *IEEE Trans. Microw. Theory Techn.*, vol. 52, no. 9, pp. 2087–2104, Sep. 2004.

[61] F. Yanovsky, V. Ivashchuk, and V. Prokhorenko, "Through-the-wall surveillance technologies," in *Proc. 6th Int. Conf. on Ultrawideband and Ultrashort Impulse Signals (UWBUSIS)*, Sep. 2012, pp. 30–33.

[62] C. R. P. Dionisio, S. Tavares, M. Perotoni, *et al.*, "Experiments on through-wall imaging using ultra wideband radar," *Microwave and Optical Technol. Lett.*, vol. 54, no. 2, pp. 339–344, Feb. 2012.

[63] S. Nag, M. A. Barnes, T. Payment, *et al.*, "Ultrawideband through-wall radar for detecting the motion of people in real time," in *Proc. SPIE Radar Sensor Technol. and Data Visualization*, vol. 4744, Jul. 2002, pp. 48–57.

[64] Q. Huang, L. Qu, B. Wu, *et al.*, "UWB through-wall imaging based on compressive sensing," *IEEE Trans. Geosci. Remote Sens.*, vol. 48, no. 3, pp. 1408–1415, Mar. 2010.

[65] S. Bartoletti, A. Conti, A. Giorgetti, *et al.*, "Sensor radar networks for indoor tracking," *IEEE Wireless Commun. Lett.*, vol. 3, no. 2, pp. 157–160, Apr. 2014.

[66] S. Bartoletti, A. Giorgetti, M. Z. Win, *et al.*, "Blind selection of representative observations for sensor radar networks," *IEEE Trans. Veh. Technol.*, vol. 64, no. 4, pp. 1388–1400, Apr. 2015.

[67] V. Casadei, N. Nanna, and D. Dardari, "Experimental study in breath detection and human target ranging in the presence of obstacles using ultra-wideband signals," *Int. J. Ultra Wideband Commun. and Syst.*, vol. 2, no. 2, pp. 116–123, 2011.

[68] A. Gonzalez-Ruiz, A. Ghaffarkhah, and Y. Mostofi, "A comprehensive overview and characterization of wireless channels for networked robotic and control systems," *J. of Robotics*, vol. 2011, Oct. 2011.

[69] A. Edelstein and M. Rabbat, "Background subtraction for online calibration of baseline RSS in RF sensing networks," *IEEE Trans. Mobile Comput.*, vol. 12, no. 12, pp. 2386–2398, Dec. 2013.

[70] D. Maas, J. Wilson, and N. Patwari, "Toward a rapidly deployable radio tomographic imaging system for tactical operations," in *Proc. 38th IEEE Conf. on Local Comput. Networks (LCN)*, Oct. 2013, pp. 203–210.

[71] B. Hamilton, X. Ma, R. Baxley, *et al.*, "Propagation modeling for radio frequency tomography in wireless networks," *IEEE J. Sel. Topics Signal Process.*, vol. 8, no. 1, pp. 55–65, Feb. 2014.

[72] B. Dewberry and W. Beeler, "Increased ranging capacity using ultrawideband direct-path pulse signal strength with dynamic recalibration," in *Proc. IEEE/ION Position Location and Navigation Symp. (PLANS)*, Apr. 2012, pp. 1013–1017.

[73] A. Molisch, "Ultrawideband propagation channels-theory, measurement, and modeling," *IEEE Trans. Veh. Technol.*, vol. 54, no. 5, pp. 1528–1545, Sep. 2005.

[74] D. Cassioli, M. Win, and A. Molisch, "The ultra-wide bandwidth indoor channel: From statistical model to simulations," *IEEE J. Sel. Areas Commun.*, vol. 20, no. 6, pp. 1247–1257, Aug. 2002.

[75] P. Agrawal and N. Patwari, "Correlated link shadow fading in multi-hop wireless networks," *IEEE Trans. Wireless Commun.*, vol. 8, no. 8, pp. 4024–4036, Aug. 2009.

[76] E. Demidenko, *Mixed models: Theory and applications with R*, 2nd ed., D. J. Balding, Ed., ser. Wiley Series in Probability and Statistics. John Wiley & Sons, 2013.

[77] N. M. Laird and J. H. Ware, "Random-effects models for longitudinal data," *Biometrics*, pp. 963–974, Dec. 1982.

[78] R. Aster, B. Borchers, and C. Thurber, *Parameter estimation and inverse problems*, 2nd ed. Academic Press, 2012.

[79] H. Zou and T. Hastie, "Regularization and variable selection via the elastic net," *J. of the Royal Stat. Soc.*, vol. 67, no. 2, pp. 301–320, Apr. 2005.

[80] A. M. Stuart, "Inverse problems: A Bayesian perspective," *Acta Numerica*, vol. 19, pp. 451–559, Apr. 2010.

[81] M. Grant and S. Boyd, "Graph implementations for nonsmooth convex programs," in *Recent Advances in Learning and Control*, ser. Lecture Notes in Control and Information Sciences, V. Blondel, Ed., Springer-Verlag Limited, 2008, pp. 95–110.

[82] R. D. Gill and B. Y. Levit, "Applications of the Van Trees inequality: A Bayesian Cramér Rao bound," *Bernoulli*, vol. 1, no. 1/2, pp. 59–79, Jun. 1995.

[83] Z. Wang, A. Bovik, H. Sheikh, *et al.*, "Image quality assessment: From error visibility to structural similarity," *IEEE Trans. Image Process.*, vol. 13, no. 4, pp. 600–612, Apr. 2004.

[84] Y. Gu, A. Lo, and I. Niemegeers, "A survey of indoor positioning systems for wireless personal networks," *IEEE Commun. Surveys Tuts.*, vol. 11, no. 1, pp. 13–32, Jan. 2009.

[85] G. Mao, B. Fidan, and B. D. Anderson, "Wireless sensor network localization techniques," *Comput. Networks*, vol. 51, no. 10, pp. 2529 –2553, Jul. 2007.

[86] F. Seco, A. Jimenez, C. Prieto, *et al.*, "A survey of mathematical methods for indoor localization," in *Proc. IEEE Int. Symp. on Intell. Signal Process. (WISP)*, Aug. 2009, pp. 9–14.

[87] H. Jamali-Rad, H. Ramezani, and G. Leus, "Sparsity-aware multi-source RSS localization," *Signal Process.*, vol. 101, pp. 174 –191, Aug. 2014.

[88] A. Coluccia and F. Ricciato, "RSS-based localization via Bayesian ranging and iterative least squares positioning," *IEEE Commun. Lett.*, vol. 18, no. 5, pp. 873–876, May 2014.

[89] H. Lim, L. C. Kung, J. C. Hou, *et al.*, "Zero-configuration, robust indoor localization: Theory and experimentation," University of Illinois, Tech. Rep., Aug. 2005.

[90] Y. Gwon and R. Jain, "Error characteristics and calibration-free techniques for wireless LAN-based location estimation," in *Proc. 2nd Int. Workshop on Mobility Management & Wireless Access Protocols*, Oct. 2004, pp. 2–9.

[91] Z. Li and P. J. Chung, "Weighted least squares solution for RSS based localization in correlated shadowing," in *Proc. IEEE Workshop on Signal Process. Sys. (SiPS)*, Oct. 2014, pp. 1–5.

[92] G. Wang and K. Yang, "A new approach to sensor node localization using RSS measurements in wireless sensor networks," *IEEE Trans. Wireless Commun.*, vol. 10, no. 5, pp. 1389–1395, May 2011.

[93] G. Wang, H. Chen, Y. Li, *et al.*, "On received-signal-strength based localization with unknown transmit power and path loss exponent," *IEEE Wireless Commun. Lett.*, vol. 1, no. 5, pp. 536–539, Oct. 2012.

[94] S. Tomic, M. Beko, and R. Dinis, "RSS-based localization in wireless sensor networks using convex relaxation: Noncooperative and cooperative schemes," *IEEE Trans. Veh. Technol.*, vol. 64, no. 5, pp. 2037–2050, May 2015.

[95] N. Patwari, A. O. Hero, M. Perkins, *et al.*, "Relative location estimation in wireless sensor networks," *IEEE Trans. Signal Process.*, vol. 51, no. 8, pp. 2137–2148, Aug. 2003.

[96] S. Gezici, "A survey on wireless position estimation," *Wireless Personal Commun.*, vol. 44, no. 3, pp. 263–282, Oct. 2008.

[97] M. R. Gholami, R. M. Vaghefi, and E. G. Ström, "RSS-based sensor localization in the presence of unknown channel parameters," *IEEE Trans. Signal Process.*, vol. 61, no. 15, pp. 3752–3759, Aug. 2013.

[98] M. B. Jamâa, A. Koubâa, N. Baccour, *et al.*, "EasyLoc: Plug-and-play RSS-based localization in wireless sensor networks," in *Cooperative Robots and Sensor Networks*, A. Koubâa and A. Khelil, Eds., ser. Studies in Computational Intelligence. Springer Berlin - Heidelberg, 2014, vol. 507, ch. 5, pp. 77–98.

[99] H. Lohrasbipeydeh, T. A. Gulliver, and H. Amindavar, "A minimax SDP method for energy based source localization with unknown transmit power," *IEEE Wireless Commun. Lett.*, vol. 3, no. 4, pp. 433–436, Aug. 2014.

[100] ——, "Blind received signal strength difference based source localization with system parameter errors," *IEEE Trans. Signal Process.*, vol. 62, no. 17, pp. 4516–4531, Sep. 2014.

[101] F. Dong, Y. Chen, J. Liu, *et al.*, "A calibration-free localization solution for handling signal strength variance," in *Mobile Entity Localization and Tracking in GPS-less Environnments*, Springer, 2009, pp. 79–90.

[102] F. Gustafsson and F. Gunnarsson, "Localization in sensor networks based on log range observations," in *Proc. 10th Int. Conf. on Inform. Fusion*, Jul. 2007, pp. 1–8.

[103] L. Lin, H. So, and Y. Chan, "Received signal strength based positioning for multiple nodes in wireless sensor networks," *Digital Signal Process.*, vol. 25, pp. 41–50, Feb. 2014.

[104] R. Vaghefi, M. Gholami, R. Buehrer, *et al.*, "Cooperative received signal strength-based sensor localization with unknown transmit powers," *IEEE Trans. Signal Process.*, vol. 61, no. 6, pp. 1389–1403, Mar. 2013.

[105] S. Fortunati, A. Farina, F. Gini, *et al.*, "Least squares estimation and Cramér-Rao type lower bounds for relative sensor registration process," *IEEE Trans. Signal Process.*, vol. 59, no. 3, pp. 1075–1087, Mar. 2011.

[106] X. Lin and Y. Bar-Shalom, "Multisensor target tracking performance with bias compensation," *IEEE Trans. Aerosp. Electron. Syst.*, vol. 42, no. 3, pp. 1139–1149, Jul. 2006.

[107] A. J. Weiss and J. S. Picard, "Network localization with biased range measurements," *IEEE Trans. Wireless Commun.*, vol. 7, no. 1, pp. 298–304, Jan. 2008.

[108] J. S. Picard and A. J. Weiss, "Localization of networks using various ranging bias models," *Wireless Commun. and Mobile Comput.*, vol. 8, no. 5, pp. 553–562, Jun. 2008.

[109] C. Laoudias, R. Piché, and C. G. Panayiotou, "Device self-calibration in location systems using signal strength histograms," *J. of Location Based Services*, vol. 7, no. 3, pp. 165–181, Aug. 2013.

[110] A. W. Tsui, Y. H. Chuang, and H. H. Chu, "Unsupervised learning for solving RSS hardware variance problem in WiFi localization," *Mobile Networks and Appl.*, vol. 14, no. 5, pp. 677–691, Oct. 2009.

[111] G. Lui, T. Gallagher, B. Li, *et al.*, "Differences in RSSI readings made by different Wi-Fi chipsets: A limitation of WLAN localization," in *Proc. Int. Conf. on Localization and GNSS (ICL-GNSS)*, Jun. 2011, pp. 53–57.

[112] B. J. Dil and P. J. M. Havinga, "RSS-based localization with different antenna orientations," in *Proc. Australasian Telecommun. Networks and Appl. Conf. (ATNAC)*, Oct. 2010, pp. 13–18.

[113] Y. Bar-Shalom, X. Li, and T. Kirubarajan, *Estimation with applications to tracking and navigation: Theory, algorithms, and software*. John Wiley & Sons, 2001.

[114] T. Adali and S. Haykin, *Adaptive signal processing: Next generation solutions*, T. Adali and S. Haykin, Eds., ser. Adaptive and Learning Systems for Signal Processing, Communication, and Control. John Wiley & Sons, 2010, vol. 55.

[115] J. C. Pinheiro and D. M. Bates, "Approximations to the log-likelihood function in the nonlinear mixed-effects model," *J. of Computational and Graphical Statist.*, vol. 4, no. 1, pp. 12–35, Mar. 1995.

[116] T. Amemiya, "A note on a heteroscedastic model," *J. of Econometrics*, vol. 6, no. 3, pp. 365–370, Nov. 1977.

[117] D. W. Marquardt, "An algorithm for least-squares estimation of nonlinear parameters," *J. of the Soc. for Ind. and Appl. Math.*, vol. 11, no. 2, pp. 431–441, Jun. 1963.

[118] J. H. Kotecha and P. M. Djuric, "Gaussian particle filtering," *IEEE Trans. Signal Process.*, vol. 51, no. 10, pp. 2592–2601, Oct. 2003.

[119] S. M. Kay, *Fundamentals of statistical signal processing: Estimation theory*, A. V. Oppenheim, Ed., ser. Signal Processing. Prentice Hall, 1993, vol. 1.